

**A Study of High Q Spiral Inductor Fabrication Methods
Using a Production Silicon Process with Application
to a Current Tuned Microwave Oscillator**

by

Daniel N. Badiere B.Sc.E.

A thesis submitted to the
School of Graduate Studies and Research
in partial fulfillment of the requirements for the degree of

Master of Engineering
in Electronics

Ottawa-Carleton Institute for Electrical and Computer Engineering
Department of Electronics
Faculty of Engineering
Carleton University

© Copyright D.N. Badiere 2001



**National Library
of Canada**

**Acquisitions and
Bibliographic Services**

**395 Wellington Street
Ottawa ON K1A 0N4
Canada**

**Bibliothèque nationale
du Canada**

**Acquisitions et
services bibliographiques**

**395, rue Wellington
Ottawa ON K1A 0N4
Canada**

Your file Votre référence

Our file Notre référence

The author has granted a non-exclusive licence allowing the National Library of Canada to reproduce, loan, distribute or sell copies of this thesis in microform, paper or electronic formats.

The author retains ownership of the copyright in this thesis. Neither the thesis nor substantial extracts from it may be printed or otherwise reproduced without the author's permission.

L'auteur a accordé une licence non exclusive permettant à la Bibliothèque nationale du Canada de reproduire, prêter, distribuer ou vendre des copies de cette thèse sous la forme de microfiche/film, de reproduction sur papier ou sur format électronique.

L'auteur conserve la propriété du droit d'auteur qui protège cette thèse. Ni la thèse ni des extraits substantiels de celle-ci ne doivent être imprimés ou autrement reproduits sans son autorisation.

0-612-61016-0

Canada

ABSTRACT

This document describes the design and measurement of a series of spiral inductors fabricated on low resistivity ($10\Omega\text{cm}$) silicon, and a bias current tuned oscillator that incorporated one of the previously mentioned spiral inductors.

The inductors were designed and fabricated in three distinct ways: top metal only (basic inductors), top metal with an inter-winding trench (trench inductors), and top and second from top metal layers connected by vias along the length of the inductor (2-metal inductors). None of these fabrication methods required any post processing steps. Approximately ten of each inductor were measured. Results indicated that compared to the basic inductors the 2-metal spirals had inductances that were between 4% and 7% lower, and peak Q values that were between 7% to 18% lower. Measured results indicated the trench inductors had up to 5% higher Qs compared to the basic inductors. One octagonal trench inductor with a measured inductance of 0.45nH demonstrated a peak Q of 20 at 15GHz, which to the author's knowledge is the highest reported Q of a spiral inductor fabricated in a production silicon process.

The integrated oscillator designed and characterized in this work used bias currents to vary the transistor parasitic capacitances presented to the resonator to tune the oscillation frequency. The oscillator demonstrated a tuning range of 9.4 - 12.3GHz, a phase noise of -86dB/Hz at 1MHz offset, a maximum output power of -3.3dBm, and second harmonic suppression of approximately 30dB.

ACKNOWLEDGEMENTS

I would first like to thank Professor Jim Wight of Carleton University. You continued to bet on a horse that did not always look like it was going to finish the race. Thanks for not giving up!

Next I would like to thank Charles Nicholls - my advisor at Nortel Networks. You supervised this work with a level of commitment and effort that far surpassed all expectations. Your organized approach to the project made it manageable and rewarding. I am grateful not only for your support in this work, but also for your contribution to my professional development. I hope you enjoyed your role as mentor.

I would also like to thank Bill Kung, A.J. Bergsma, Doug Beards, Simon Damphousse, John Ilowski, Bob Leroux and everyone from department RE10 at Nortel Networks Wireless not already mentioned. I can not imagine where I would be without your help. Thanks for your patience in dealing with my seemingly infinite questions.

I would also like to express my appreciation to Nortel Networks for giving me the opportunity to work with some of the brightest people I have ever met, and for the generous donation of resources.

Thanks is also due to Philippe Lafleur for his generosity during that first time around.

Last, but not least, I would like to thank Cindy Wolfe for her encouragement during those early days in Toronto, and her unwavering support ever since.

TABLE OF CONTENTS

ABSTRACT	iii
ACKNOWLEDGEMENTS	iv
TABLE OF CONTENTS	v
LIST OF TABLES	viii
LIST OF FIGURES	ix
CHAPTER 1: Introduction	1
1.1 Goal of Research	1
1.2 Thesis Outline	3
1.3 Contribution	4
CHAPTER 2: On-chip Inductor Theory and Design	5
2.1 On-chip Inductor Characteristics	5
2.1.1 Definition of Inductor Q	8
2.2 Inductor Design	10
2.2.1 Area	10
2.2.2 Trace Thickness	11
2.2.3 Trace Width	12
2.2.4 Line Spacing	12
2.2.5 Center Gap	13
2.2.6 Distance to Surrounding Metal	14
2.2.7 Inductor Geometry	14
2.2.8 Substrate Trenches and Ground Shields	15
2.3 Description of Inductor Study	16
2.3.1 Dimensions of Fabricated Inductors	18
2.3.2 Layout of Inductors Studied	22
2.4 Measurement and De-embedding	23
2.4.1 The Modified Cho Method of De-embedding	23
2.4.2 The Modified Koolen Method of De-embedding	26
2.4.3 One Port Inductor De-embedding	27
2.5 Summary	29

CHAPTER 3: Inductor Measurement and Results 30

3.1 Inductor Measurement Results 32
3.1.1 Inductor Measurement Error 41
3.2 Discussion of Inductor Results 43
3.2.1 Comparison of Modified Koolen and Modified Cho
De-embedding Methods. 44
3.2.2 Effect of Using Two Metal Layers to Fabricate Inductor
Windings 46
3.2.3 Effect of Trench on Inductor Performance 47
3.2.4 Effect of Inductor Size on Performance. 49
3.2.5 Effect of Inductor Shape on Performance 49
3.3 Spiral Inductor Simulation. 50
3.3.1 Octagonal Inductor Simulation 51
3.3.2 Comparison of Square Inductor Simulations and Measurements . 52
3.4 Summary 57

CHAPTER 4: Oscillator Theory and Design 58

4.1 Parallel LCR Resonators 58
4.1.1 Resonator Quality Factor 59
4.1.2 Parallel Resonator with Series Inductor Losses. 61
4.1.3 Sustained Oscillation 64
4.2 Phase Noise 65
4.3 Generation of Negative Resistance 72
4.3.1 The Cross-coupled Differential Pair 74
4.3.2 The Cross-coupled Differential Pair with Emitter-Follower
Buffers 76
4.4 Frequency Tuning 79
4.4.1 Emitter-Follower Current Controlled Frequency Tuning 80
4.4.2 Differential Pair Bias Current Controlled Frequency Tuning 82
4.5 Design of Bias Current Tuned Oscillator. 83
4.5.1 Selection of Inductor 84
4.5.2 Selection of Transistor Size 85
4.5.3 Oscillator Simulation Results 86
4.5.4 Output Buffer. 87
4.5.5 Phase Noise Calculation 91
4.6 Summary 96

CHAPTER 5: Oscillator Measurement and Results 97

5.1 Phase Noise Measurement. 97
5.1.1 Direct Spectrum Measurement 97

5.1.2	Phase Locked Reference Source Method	98
5.1.3	The Frequency Discriminator Method	100
5.1.4	Theory of the Frequency Discriminator Method	101
5.1.5	Selection of the Delay Line	106
5.2	Oscillator Measurements and Analysis	108
5.2.1	Phase Noise Measurements	108
5.2.2	Comparison of Estimated Phase Noise to Measured Phase Noise	115
5.2.3	Reducing Oscillator Phase Noise	116
5.2.4	Tuning Range and Output Power Measurements	118
5.2.5	Frequency Pushing	124
5.2.6	Second Harmonic Power	126
5.2.7	Frequency Pulling	126
5.3	Summary	128
CHAPTER 6: Conclusion		129
6.1	Summary	129
6.2	Thesis Contribution	130
6.3	Future Work	131
REFERENCES		133
APPENDIX A: Emitter Follower Analysis		135
A.1	Input Impedance	135
A.2	Output Impedance	136
A.3	Voltage Gain	137
APPENDIX B: Proof of (EQ 2.27)		138
APPENDIX C: MATLAB De-embedding Code		145
C.1	The Modified Cho De-embedding Code	145
C.2	Modified Koolen De-embedding Code	155
C.3	The 1-Port De-embedding Code	159
APPENDIX D: Full Circuit Schematic		163

LIST OF TABLES

Table	Description	Page
1.1	Performance goals for oscillator.	3
2.1	Dimensions of the square inductors. Each inductor had a line width of 10mm, a line spacing of 3mm, and 80mm clearance to surrounding metal.	19
2.2	Dimensions of octagonal inductors. Each inductor had a line width of 10mm, a line spacing of 3mm, and a clearance of 80mm to surrounding metal.	21
3.1	Inductor sizes and number measured.	32
3.2	Average measured results of the two port square inductors.	32
3.3	Average measured results of the octagonal inductors (all two port).	33
3.4	Average measured results for one port square inductors.	33
3.5	Four measurements of the same 0.5nH octagonal inductor.	43
3.6	Measured average self resonant frequencies of inductors with $L > 0.5\text{nH}$	48
3.7	Material values used in HP EEs of Momentum for each inductor.	52
3.8	Simulated and measured parameters for the basic square inductors.	52
4.1	Target specifications for bias tuned oscillator.	83
4.2	Targeted and estimated phase noise values for the bias current tuned oscillator.	95
5.1	Spectral density of phase noise fluctuations (dBc/Hz) for five different oscillator signal frequencies.	110
5.2	Frequency tuning range of oscillator. All frequencies are in GHz.	120
5.3	Oscillator output power over tuning range.	123
5.4	Pushing figure of oscillator.	124
5.5	Second harmonic power of oscillator signal.	126

LIST OF FIGURES

Figure	Description	Page
2.1	Cross-section view of on-chip inductor.	5
2.2	Spiral inductor substrate current flow. I _{cir} represents eddy currents, induced by currents in the windings, circulating in the substrate. Other substrate currents flow between windings, and to ground. The resistors represent ohmic losses in the substrate.	6
2.3	Equivalent circuit model for an on-chip spiral inductor.	7
2.4	Lossy inductor.	8
2.5	Square inductor with key layout parameters labeled: (a) top view, (b) cross section view of trace.	10
2.6	Cross section of an on-chip inductor near some form of metallization. (a) cancellation of flux (dashed lines) by windings on opposite sides of the inductor. (b) eddy currents generated in surrounding metal by inductor's magnetic field. Note substrate currents are not shown for simplicity.	14
2.7	Cross section close-up (top row) and entire top (bottom row) views of inductors fabricated in: a) top metal only, b) top metal with an inter-winding substrate trench, and c) two metal layers joined by vias along the entire length of the inductor with a maximum spacing of 5mm.	17
2.8	Skin depth from 100MHz to 100GHz in the aluminum winding metallization.	18
2.9	Underpasses for the Square Inductors.	20
2.10	A single turn of an octagonal inductor.	21
2.11	Modifications to the 1.0nH and 0.4nH octagonal inductors. Note the 0.4nH inductor has a shorter and wider underpass than the 1.0nH inductor. It should also be noted that these diagrams are not to scale. The distance between the outer edge of the spiral and the enclosing metal was 80mm.	22
2.12	Typical layout of inductors for two port measurements.	22
2.13	Inductor surrounded by pad and feed line parasitics - modified from Cho's circuit [6].	23
2.14	Modified Cho model for open pad parasitics.	24

2.15	Shorted pad circuit model for the modified Cho method of de-embedding.....	25
2.16	Modified Koolen model of an inductor embedded in pad and feed line parasitics.....	26
2.17	Modified versions of Koolen's open and short pad parasitics models...	27
2.18	One port inductor test structure and open pad layout.....	28
2.19	One port inductor with surrounding parasitics.....	28
3.1	Inductor measurement setup configuration.....	30
3.2	Flow chart describing the steps the de-embedding code performs to obtain L and Q for the spiral inductor from measured S-parameter data.	31
3.3	Inductor with loss for calculation of Q.....	35
3.4	Series resistance (R_s) and series reactance (X_s) over frequency for inductor.....	36
3.5	Segment of an inductor winding.....	37
3.6	Plot of each type of 1.5nH square inductor - average of 10 samples...	37
3.7	Plots of each type of 1.0nH square inductor - average of 11 samples...	38
3.8	Plot of each type of 0.5nH square inductor - average of 10 samples...	38
3.9	Plots of each type of 0.4nH square inductor - average of 10 samples...	39
3.10	Plot of each type of 1.5nH octagonal inductor - average of 9 samples..	39
3.11	Plots of each type of 1.0nH octagonal inductor - average of 11 samples.	40
3.12	Plot of each type of 0.5nH octagonal inductor - average of 10 samples.	40
3.13	Plot of each type of 0.4nH octagonal inductor - average of 9 samples..	41
3.14	A cluster of test structures for a square inductor.....	42
3.15	Q and L curves of the basic 0.5nH octagonal inductor using the two de-embedding methods.....	46
3.17	Measured and simulated data for the 1.5nH square inductor.....	55
3.16	Cross section views of simulator metallization layering and actual physical metallization layering, for underpass portion of inductor.....	55
3.18	Measured and simulated data for the 1.0nH square inductor.....	56
3.19	Measured and simulated data for the 0.5nH square inductor.....	56
3.20	Measured and simulated data for the 0.4nH square inductor.....	57
4.1	Parallel LC resonator structures: a) lossless and b) with loss.....	58
4.2	Parallel resonator with series inductor losses.....	61
4.3	Parallel resonator with parallel losses and parallel resonator with series losses: a) for $Q=2$, b) for $Q=10$, and c) for $Q=20$. Note the magnitude curves for the two types of resonator appear coincident in plots b and c.....	63
4.4	LC resonator with losses cancelled by $-R$	65

4.5	Oscillator feedback loop for phase noise model derivation.....	66
4.6	Magnitude and phase response of an LCR resonator with a Q of 30. . .	68
4.7	Small-signal circuit of LCR resonator with unstable amplifier.	73
4.8	Cross-coupled differential pair circuit (biasing not shown).....	74
4.9	Small signal model of cross-coupled pair.	74
4.10	Cross-coupled Differential Pair with Emitter-Follower Buffers (biasing not shown).	76
4.11	Small Signal equivalent circuit of cross coupled pair with emitter-followers.	77
4.12	Emitter-follower small signal model with parasitic capacitances.	80
4.13	Small signal model of emitter-follower with differential pair transistor as load.	82
4.14	Simple model of spiral inductor	85
4.15	Bias current controlled oscillator.....	86
4.16	Simulated results for (a) the oscillator resonator signal buildup during startup, and (b) the steady state resonator signal spectrum.	88
4.17	Cascode output buffer stage.....	89
4.18	Oscillator connected to output buffer.....	90
4.19	Oscillator with initial and output buffers.....	91
4.20	-R cell circuit used to determine CCL.....	92
4.21	Active part of oscillator with feedback loop opened and extra components added to maintain correct loading.	93
4.22	Resonator circuit for the determination of loaded Q.	93
5.1	Basic phase detector setup for phase noise measurement.	99
5.2	The frequency discriminator method of phase noise measurement [11].	100
5.3	The generic response of a frequency discriminator.	107
5.4	Phase noise measurement equipment and connections.	109
5.5	Oscillator phase noise at 10.5GHz oscillation frequency.	112
5.6	Oscillator phase noise at 11GHz oscillation frequency.	113
5.7	Oscillator phase noise at 11.5GHz oscillation frequency.	113
5.8	Oscillator phase noise at 12GHz oscillation frequency.....	114
5.9	Oscillator phase noise at 12.3GHz oscillation frequency.	114
5.10	Oscillator phase noise at 12.3GHz compared to estimated and targeted phase noise.....	116
5.11	Bias current controlled oscillator.....	117
5.12	Setup for oscillator measurements using a spectrum analyzer.....	119
5.13	Frequency tuning range of oscillator.	122
5.14	Output power of oscillator over tuning range.	123

5.15	Oscillator circuit with non-ideal current sources.....	125
5.16	Frequency pulling measurement setup.....	127
A.1	Small signal model of emitter follower.	135
A.2	Emitter follower small signal circuit connected for output impedance analysis.	136
B.1	Modified Koolen model of an inductor with pad and feed line parasitics.	138
B.2	Modified versions of Koolen's open and shorted pad parasitics models.	138
B.3	Parasitic impedances Z_1 and Z_2 lumped with the inductor to form the network inside the dashed lines.	139
B.4	Inductor Z parameter equivalent circuit (inside the dashed lines) with feed line series parasitics.	143
D.1	Schematic of oscillator circuit.	164
D.2	Schematic of the pre-driver circuit.....	165
D.3	Schematic of output buffer circuit.	166

CHAPTER 1: Introduction

In recent years the use of wireless services has grown. One of the limiting factors of this wireless expansion is equipment costs. Substantial cost savings could be achieved in wireless systems by integrating the entire transceiver onto a single chip. Oscillators, which are essential components of most transceivers, have typically shown poor phase noise performance when integrated on low resistivity ($10\Omega\text{cm}$) production quality silicon. While some on-silicon integrated oscillators have been demonstrated that meet the specified maximum phase noise levels for standards such as DECT [22], on-silicon oscillators have failed to meet the requirements for high QAM (Quadrature Amplitude Modulation) point-to-point and point-to-multipoint microwave radios. The high phase noise levels of production silicon integrated oscillators are due to the poor quality factors (<15) of on-chip inductors and varactors (~ 7 for the bipolar process used at the frequencies of interest in this work) that form part of the resonator.

This work addresses these issues: by examining two on-chip inductor fabrication methods that have the potential of increasing the quality factor of on-chip spiral inductors: and by designing, fabricating, and testing an integrated oscillator that uses transistor parasitic capacitance (instead of a varactor) to perform frequency tuning.

1.1 Goal of Research

The goals of this research work are:

- To evaluate two different layout techniques for on-chip spiral inductors that have the potential to improve the quality factor of the inductor compared to the general top metal layout that is often used.
- To investigate a varactorless oscillator design that uses emitter followers to buffer the resonator, and uses transistor bias current rather than the voltage across a varactor to control the frequency of oscillation.

The oscillator performance targets are listed in Table 1.1. The phase noise budget for a millimeter wave LO (Local Oscillator) is dependent on various factors such as modulation scheme, data rate, and radio architecture. Consequently, the targeted phase noise values are based on the requirements of a 64 QAM radio developed at Nortel Networks.

Designing a 30GHz oscillator in the available bipolar technology would have been impractical. Instead the target frequency range reflects that of an oscillator operating at half the frequency required by LMDS (Local Multipoint Distribution Service) with a view to the LO driving a sub harmonic mixer. Thus the targeted phase noise shown in Table 1.1 is that required by the oscillator signal to meet the requirements of the LMDS radio after frequency doubling through a doubler that adds $20\log(2)$ or 6dB of phase noise - the contribution of an ideal frequency doubler.

Parameter	Phase Noise for LMDS Radio	Target Value
Frequency	28 - 30 GHz	14 - 15 GHz
Phase Noise	-113 dBc/Hz @ 1MHz offset*	-119 dBc/Hz @ 1MHz offset
	-93 dBc/Hz @ 100kHz offset*	-99 dBc/Hz @ 100kHz offset
	-73 dBc/Hz @ 10kHz offset*	-79 dBc/Hz @ 10kHz offset
	-53 dBc/Hz @ 1kHz offset*	-59 dBc/Hz @ 1kHz offset

*for customer premise equipment

Table 1.1: Performance goals for oscillator.

1.2 Thesis Outline

Chapters 2 and 3 discuss the on-chip spiral inductor work, with Chapter 2 presenting on-chip spiral inductor theory and design as well as the inductors fabricated for this research. Methods of de-embedding inductor characteristics from on-wafer measurements are also discussed.

Chapter 3 discusses inductor measurement and presents the measured results for the inductors described in Chapter 2. Inductor performance is related to each fabrication method as well as to characteristics such as inductor size and shape. Comparisons of measured results to simulated results are presented.

Chapter 4 discusses oscillator theory and design, and the varactorless oscillator designed and fabricated for this research. Expected performance of the oscillator, based on simulations, is also presented.

Chapter 5 discusses the frequency discriminator method of phase noise measurement and presents the oscillator phase noise measurements. Measurements of tuning range, output power, frequency pulling and pushing figures, and second harmonic power are also presented and discussed.

Chapter 6 summarizes the thesis work and results.

1.3 Contribution

One of the purposes of this thesis is to investigate possible means of improving on-silicon spiral inductor quality factor in a production type process. That is, no special post processing steps are to be used. Though each production technique has been attempted before, little has been published: this work therefore attempts to provide valuable insight into these techniques.

The other purpose of this thesis is to examine an oscillator topology that controls oscillation frequency by varying the circuit's bias current - no varactors are used. This topology has been attempted at least once [18] with current tuning accomplished by varying only one bias current level. The oscillator examined in this work uses higher quality factor inductors in its resonator, and tunes frequency by varying one or both of two different bias currents.

CHAPTER 2: On-chip Inductor Theory and Design

In silicon RFIC's (radio frequency integrated circuits) the metallization for planar spiral inductors is deposited on an oxide layer that separates the inductor from the semiconducting substrate as shown in Fig. 2.1. The oxide layer electrically insulates the current flowing in the inductor from the low impedance, lightly doped silicon substrate connected to ground. The metal windings are microstrip transmission lines with the silicon substrate serving as a ground plane. In a silicon bipolar process the winding metallization is typically aluminum.

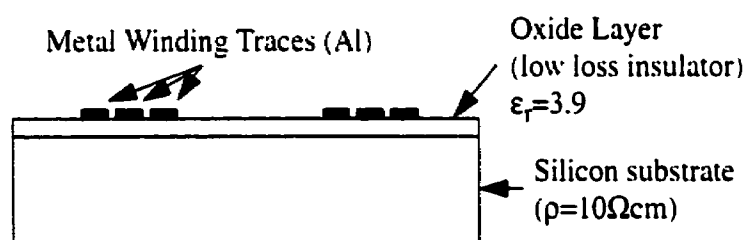


Fig. 2.1: Cross-section view of on-chip inductor.

The radio frequency properties of on-chip inductors are significantly influenced by the parasitic impedance between the inductor windings and the substrate.

2.1 On-chip Inductor Characteristics

On-chip spiral inductors exhibit two main sources of loss: resistive winding losses, and substrate losses. Resistive winding loss refers to ohmic loss due to the small inherent resistivity of the metal winding material ($2.825 \times 10^{-8} \Omega$ for aluminum at DC [1]). As the

frequency of the signal passing through the inductor increases, the skin effect reduces the cross sectional conduction area of the inductor windings. Consequently, the resistance of the windings increases with frequency, and hence their losses increase.

Substrate loss is the result of currents flowing in the substrate that are induced by fields from the inductor windings. Substrate currents can be: circulating (I_{cir} in Fig. 2.2) eddy currents induced by the magnetic fields generated in the windings; currents to ground that flow through the oxide capacitance and the substrate capacitance to ground; or inter-winding currents that flow from a particular winding through the oxide capacitance across the substrate and back through the oxide capacitance to other windings [2]. The resistors in Fig. 2.2 model the ohmic loss of currents flowing in the substrate.

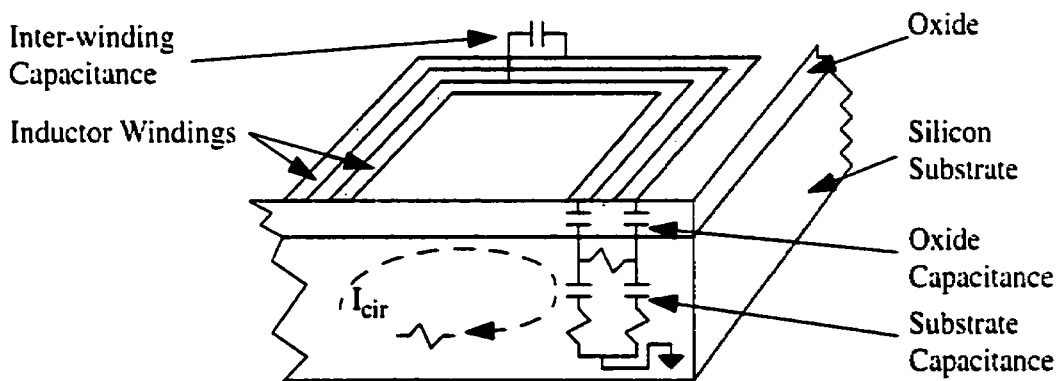


Fig. 2.2: Spiral inductor substrate current flow. I_{cir} represents eddy currents, induced by currents in the windings, circulating in the substrate. Other substrate currents flow between windings, and to ground. The resistors represent ohmic losses in the substrate.

As shown in Fig. 2.2 silicon on-chip inductors have three types of parasitic capacitance: inter-winding, oxide, and substrate. Inter-winding capacitance is the parallel plate

and fringe capacitance between windings. Oxide capacitance is the capacitance between the inductor metal and the substrate, and is shown in Fig. 2.2. Substrate capacitance is the capacitance between the top of the substrate and ground. Usually the substrate is tied to ground through vias to metallization that is grounded externally (off-chip). At RF and microwave frequencies however, the resistance and finite response time of the substrate to the applied fields causes the potential throughout the substrate to exhibit a nonuniform distribution relative to the external ground applied to the circuit. The result is capacitance within the substrate itself.

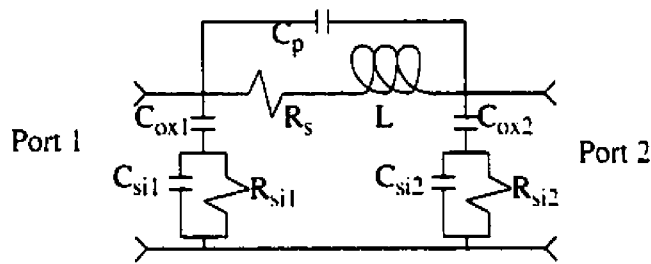


Fig. 2.3: Equivalent circuit model for an on-chip spiral inductor.

Fig. 2.3 shows a commonly used on-chip spiral inductor equivalent circuit model. The model is not scalable and its component values are usually derived by curve fitting to measured or simulated data. C_p represents the inter-winding capacitance; C_{ox} represents the oxide layer capacitance; and C_{si} represents the substrate capacitance. R_s models the series winding losses, and R_{si} represents the substrate losses. The model shows two possible modes of resonance: between L and C_p , and between L and capacitances $C_{ox1,2}$ and $C_{si1,2}$. When an inductor resonates in either of these two modes it is referred to as self resonance. Which of the two modes resonates first is dependent on the component values which result

from the physical dimensions of the inductor. The first frequency at which resonance occurs is usually called the first self resonant frequency, or just the self resonant frequency (SRF). The model in Fig. 2.3 is usually only accurate up to the first self resonant frequency.

2.1.1 Definition of Inductor Q

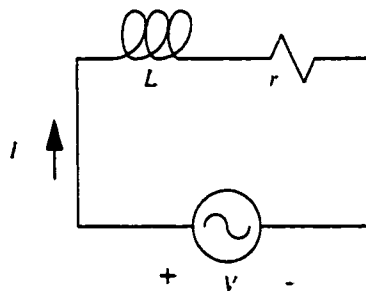


Fig. 2.4: Lossy inductor

Fig. 2.4 shows a lossy inductor with the losses modeled by a series resistance r . A commonly used term to evaluate inductors is the quality factor or Q . Q is defined as

$$Q = \frac{2\pi(E_{pk})}{(P_{loss}/cycle)} \quad (\text{EQ 2.1})$$

where E_{pk} is the peak stored energy in the inductor and $P_{loss}/cycle$ is the power lost in the inductor over one cycle (AC operation is assumed see Fig. 2.4). For an inductor

$$E_{pk} = \frac{1}{2} I_{pk}^2 L \quad (\text{EQ 2.2})$$

where L is the inductance value of the inductor, and I_{pk} is the peak value of the current through the inductor.

$$P_{loss}/cycle = (I_{rms}^2 r)T \quad (\text{EQ 2.3})$$

where I_{rms} is the root mean square value of the current through the inductor, and T is the period of one cycle. T can be expressed as

$$T = \frac{2\pi}{\omega} \quad (\text{EQ 2.4})$$

and I_{rms} can be expressed as

$$I_{rms} = \frac{I_{pk}}{\sqrt{2}} \quad (\text{EQ 2.5})$$

Using (EQ 2.3), (EQ 2.4), and (EQ 2.5) the power loss per cycle can be rewritten as

$$P_{loss}/cycle = \left(\frac{I_{pk}^2}{2} r\right) \left(\frac{2\pi}{\omega}\right) \quad (\text{EQ 2.6})$$

Substituting (EQ 2.2) and (EQ 2.6) into (EQ 2.1) gives the Q of the inductor in terms of ω , r , and L :

$$Q = \frac{\omega L}{r} \quad (\text{EQ 2.7})$$

From this definition a perfect or lossless inductor ($r = 0$) would have an infinite Q, and as losses increase ($r \rightarrow \infty$) Q would approach zero.

To find the Q of the spiral inductor model in Fig. 2.3, the series impedance looking into the spiral is first determined. Assuming the inductor is operating below its SRF, the impedance will look like a series inductance, L_{eff} , and a series resistance r_{eff} . Using L_{eff}

in place of L , and r_{eff} in place of r (in (EQ 2.7)) will yield the inductor's Q at a given frequency.

2.2 Inductor Design

Inductor design involves optimizing layout parameters such as trace width, line length, and area to achieve desired inductance and Q at a certain frequency. The following subsections give important inductor layout parameters and their effects on inductor performance.

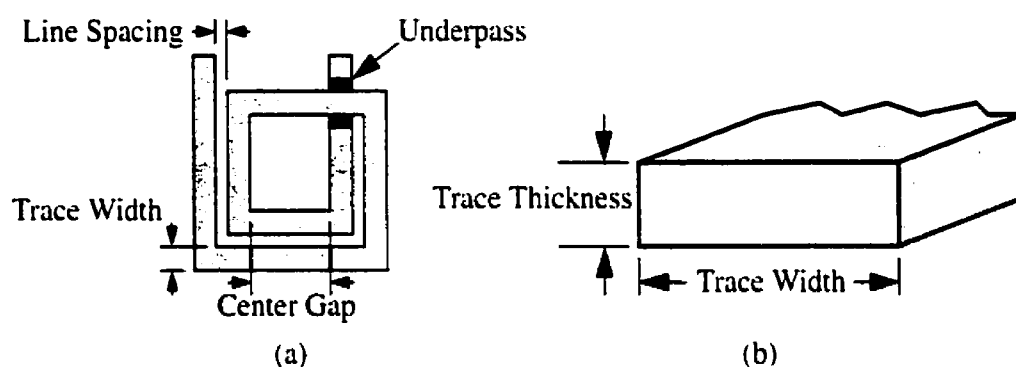


Fig. 2.5: Square inductor with key layout parameters labeled: (a) top view, (b) cross section view of trace.

2.2.1 Area

The area occupied by the inductor affects the cost of the inductor. Typically the more chip area a circuit occupies, the more expensive it is. The area an inductor occupies also affects its performance. The larger the inductor area, the more capacitive coupling to the substrate there will be, consequently lowering the SRF and increasing the substrate loss. An increase in substrate loss will decrease the quality factor of the inductor.

2.2.2 Trace Thickness

Trace thickness is typically fixed by the fabrication process, and is therefore not usually a parameter that a circuit designer can change. Changes in trace thickness affect the SRF of the spiral inductor. Increasing the thickness of the windings increases the interwinding capacitance of the spiral thereby reducing the frequency at which Q reaches its peak, and the SRF. Published measured results [14] indicate this effect is small over trace thicknesses of 0.7–3.5 μm .

Trace thickness also has an impact on the winding losses. Increasing the trace thickness increases the cross sectional area of the trace thereby reducing the overall winding resistance. The benefits of increased trace thickness can be reduced by the skin effect.

The skin depth of a conductor is found from

$$\delta_s = \sqrt{\frac{2}{\omega\mu\sigma}} \quad (\text{EQ 2.8})$$

where ω is the angular frequency of the signal in the conductor in rad/s, σ is the conductivity of the conductor material in S/m, and μ is the permeability of the conductor material in H/m. The skin depth is the depth into the conductor material at which the current density has dropped by a factor of $\frac{1}{e}$. For the particular fabrication process used in this study

$\sigma = 3.54 \times 10^7 \frac{\text{S}}{\text{m}}$ and $\mu = \mu_0$. For an angular frequency of $\omega = 2\pi \times 10^9$ (1GHz), the skin

depth is $\delta_s = 2.7\mu\text{m}$, which is close to the $3\mu\text{m}$ trace metal thickness used in this study.

This suggests that increasing the trace thickness would result in a small reduction in winding resistance.

2.2.3 Trace Width

Trace width is a parameter that a designer can readily control. Increasing the width leads to a greater cross sectional conductor area which, subject to skin effect, may yield lower resistive winding losses. Increasing the trace width also increases the overall area of the inductor which leads to greater capacitive coupling to the substrate resulting in a lower SRF and peak Q frequency. Higher substrate coupling results in higher substrate losses which reduces the quality factor of the inductor.

Because trace width affects multiple inductor parameters, its selection often requires a series of simulations to find the optimal value in conjunction with fabrication and measurement of proposed designs to verify the performance parameters. This continues to be an area that requires further work in order to find a more rigorous method of trace width optimization.

2.2.4 Line Spacing

The closer the line spacing (see Fig. 2.5), the greater the mutual coupling between adjacent lines. This mutual coupling is desirable as it serves to increase the overall inductance of the spiral which, through (EQ 2.7), directly increases the Q of the device. Reduced winding spacing increases the inter-winding capacitance (C_p in Fig. 2.3) of the inductor. According to work presented in [3], the increase in inter-winding capacitance is

not significant and therefore the minimum allowable spacing offered by the fabrication process is recommended in order to maximize inductance and Q.

2.2.5 Center Gap

Spiral inductors store energy as magnetic flux that passes through the center and around the exterior of the inductor. Eddy currents opposing the magnetic flux of the inductor will flow in metallization placed in the center gap of the spiral, which will reduce the amount of energy stored in the inductor's field (decreasing L and Q), and increase the power losses in the inductor (further reducing Q).

A gap of insufficient size permits flux generated in the opposite sides of the inductor to partially cancel each other as shown in Fig. 2.6. once again reducing L and Q. The center space (center gap in Fig. 2.5) should be free of metal, and, because magnetic coupling is inversely proportional to distance, large enough to avoid cancellation of magnetic flux between lines on opposite sides of the inductor. Work by Long [3] suggests a minimum distance of five line widths between opposite sides of the inductor to reduce this magnetic field cancelling effect.

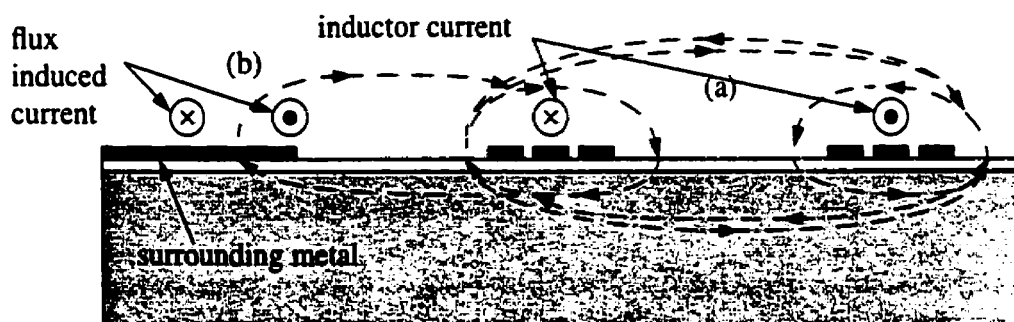


Fig. 2.6: Cross section of an on-chip inductor near some form of metallization. (a) cancellation of flux (dashed lines) by windings on opposite sides of the inductor. (b) eddy currents generated in surrounding metal by inductor's magnetic field. Note substrate currents are not shown for simplicity.

2.2.6 Distance to Surrounding Metal

Just as magnetic flux should be permitted to pass through the center of the inductor, it must also be permitted to pass around the exterior of the inductor. As shown in Fig. 2.6, flux from the inductor can establish eddy currents in any metallization around the inductor. These eddy currents drain energy from the inductor (decreasing Q) and reduce the overall inductance of the spiral (decreasing L and further decreasing Q). Reference [3] suggests surrounding metallization should be placed no closer than five line widths from the outside edge of the outer inductor winding.

2.2.7 Inductor Geometry

Most on-chip inductors have a rectangular geometry. The 90° bends of a rectangular geometry form sharp discontinuities in the windings which produce capacitive parasitics to ground and resistive losses due to current crowding at the corners. Circular spirals,

which do not have bends in the winding traces, have shown improvements in Q of up to 10% over square spirals [3]. However, because circular spirals occupy more space, and because circular shapes can be very difficult to generate in photomasks, square spirals are more popular than circular. Octagonal spirals have 45° bends, which are a relatively softer discontinuity compared to 90° bends, and can offer a nearly 10% increase in Q , while producing little to no difficulty in photomask generation.

2.2.8 Substrate Trenches and Ground Shields

Additional elements have been added to the layout of on-chip inductors in an attempt to reduce substrate losses. Two such elements that are readily available in some production processes are patterned ground shields [4] and substrate trenches.

Patterned ground shields are conductive sheets, connected to ground metallization, placed between the inductor and the substrate. The ground shields stop the electric field from the inductor from establishing currents in the lossy silicon substrate. A solid conductive shield, located on the order of a few microns beneath the inductor, would allow eddy currents to flow dropping the L and Q of the inductor. To avoid eddy currents the shield is not solid. Instead, a pattern of slots is etched in the shield to interrupt eddy current flow. Bringing a grounded conductor so close to the inductor significantly increases the capacitance between the inductor windings and ground thereby reducing the SRF of the inductor.

Substrate trenches are thin insulating slots, $1\mu\text{m}$ wide, etched to a depth of $7\mu\text{m}$ (these values are specific to the process used in this work [25]) into the surface of the silicon substrate. These trenches present an insulating barrier to substrate currents flowing near the substrate - oxide layer boundary. Substrate currents are forced underneath or around the trenches increasing the impedance they experience. In particular, when the trenches are placed between the inductor windings, the inter-winding current discussed in Section 2.1, (the current that flows from one winding, through the oxide, across the substrate, and up through the oxide to other windings) experiences a greater impedance. Thus the trenches reduce substrate currents resulting in an increase in inductor quality factor.

2.3 Description of Inductor Study

The purpose of this study was to construct inductors with trenches between the windings (to impede inter-winding current flow); and to construct inductors with windings composed of two metal layers as opposed to one (to reduce series winding resistance). The performance metrics of Q, L and SRF were used to compare each structure to a basic top metal only inductor (see Fig. 2.7). The comparison enabled the merits of each design approach to be determined.

Two sets of four inductors were designed for this study. One set of inductors were square shaped, while the inductors in the other set were octagonal. Target inductance values in each set were 0.4nH , 0.5nH , 1.0nH , and 1.5nH as these were values required for a planned VCO design. Each set of inductors were fabricated three ways (Fig. 2.7): in top

metal only, in top metal with an inter-winding substrate trench, and in a parallel two metal layer fashion (2-metal). The top metal only inductors, also referred to as basic inductors, reflected the way on-chip inductors are typically fabricated, and were therefore used as control structures with which to compare the trench and 2-metal inductors.

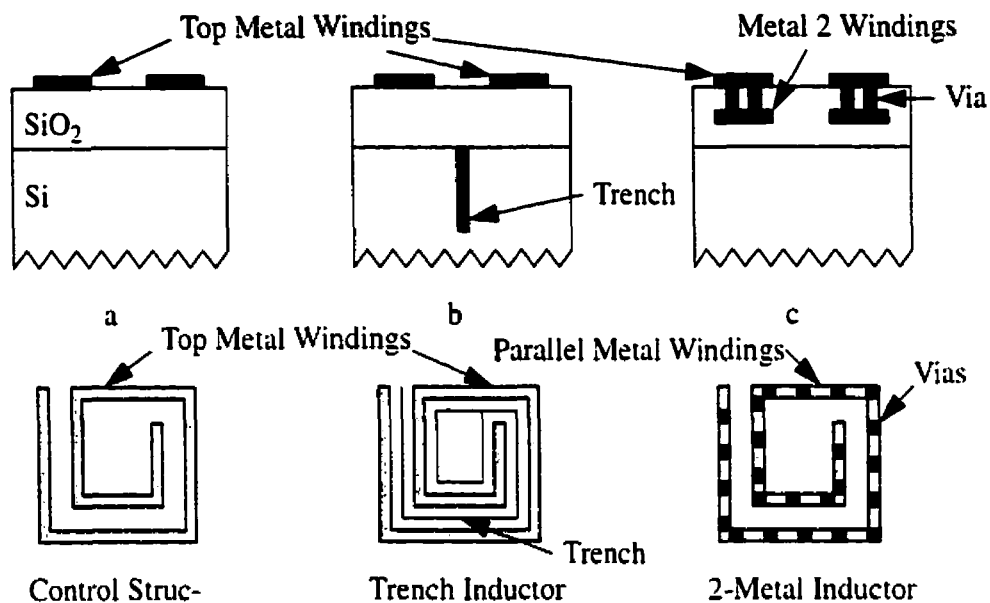


Fig. 2.7: Cross section close-up (top row) and entire top (bottom row) views of inductors fabricated in: a) top metal only, b) top metal with an inter-winding substrate trench, and c) two metal layers joined by vias along the entire length of the inductor ($5\mu\text{m}$ maximum via spacing).

The purpose of the inter-winding trench was to impede inter-winding currents flowing in the substrate, thereby reducing losses in the substrate and increasing Q .

Adding a parallel metal winding to the top metal winding was done to reduce the series winding resistance of the inductors, thereby increasing Q . In the fabrication process used the top metal layer had a resistivity of $10\text{m}\Omega$ per square, and the second metal layer had a resistivity of $28\text{m}\Omega$ per square. Thus at DC the 2-metal inductors were expected to

have $\left(\frac{1}{10m\Omega} + \frac{1}{28m\Omega}\right)^{-1} = 7.37m\Omega$ of sheet resistance, or a winding resistance 26% lower than that of the top metal only inductors. At the intended measurement frequencies (>1GHz) however, the resistivity of the windings was expected to be subject to skin effect. Fig. 2.8 shows a plot of skin depth between 100MHz and 100GHz for an aluminum conductor with $\sigma = 3.54 \times 10^7 \frac{S}{m}$ and $\mu = \mu_0$. The frequency dependent resistance of this type of winding structure cannot be easily calculated. However, because the skin depth ($\delta_s = 2.7\mu m$ at 1GHz) is not much smaller than the trace thickness ($3\mu m$ and $1\mu m$ for the top and second from top metal layers respectively), the series winding resistance of the 2-metal inductor was expected to be lower than that of the control structure.

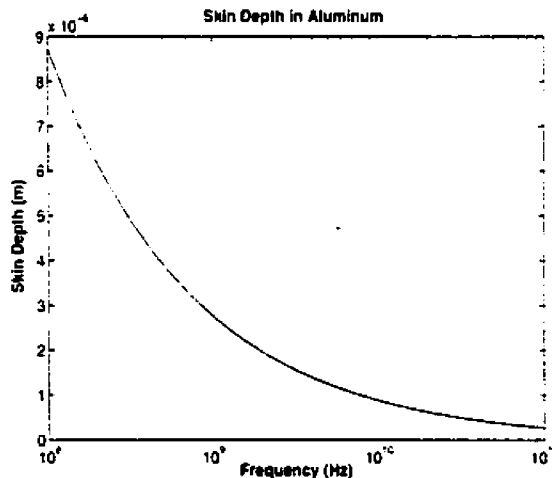


Fig. 2.8: Skin depth from 100MHz to 100GHz in the aluminum winding metallization.

2.3.1 Dimensions of Fabricated Inductors

Basic top metal versions of each inductor were simulated using the electromagnetic simulator Momentum included with Series IV Libra from EEsof.

Momentum simulations showed that a line width of $10\mu\text{m}$ yielded what appeared to be the best Q for both the square and octagonal inductors. The line spacing was chosen to be $3\mu\text{m}$ (the minimum permitted by the process) in keeping with the spacing guide-line of section 2.2.4. Table 2.1 lists other relevant dimensions for each of the square inductors.

Target Inductance (nH)	Number of Turns	Length of Side (μm)	Length of Underpass (μm)	Width of Underpass (μm)
1.5	2.75	150	29	20
1.0	2.75	130	29	20
0.5	2	100	43	10
0.4	2	96	37	10

Table 2.1: Dimensions of the square inductors. Each inductor had a line width of $10\mu\text{m}$, a line spacing of $3\mu\text{m}$, and $80\mu\text{m}$ clearance to surrounding metal.

The underpass lengths for the 1.0nH and 1.5nH square inductors were made as small as possible given the fabrication process spacing rules. Two exceptions to this were the 0.4nH and 0.5nH inductors (see Fig. 2.9). These two had much longer underpass segments for reasons related to a study that was to be conducted by Nortel Networks that used these inductors in a VCO. Since each inductor was to be compared only to a different construction of itself (the control), these extended underpass segments were not expected to affect the conclusions that were to be drawn at the end of the study.

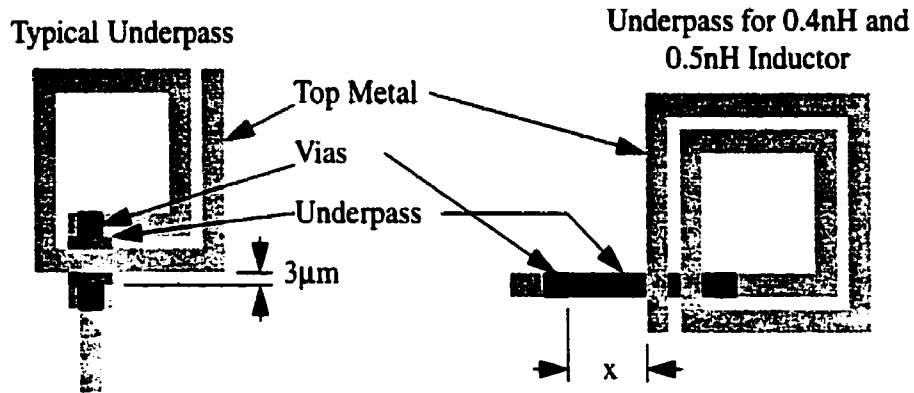


Fig. 2.9: Underpasses for the Square Inductors

The octagonal inductors were drawn using the concept of a decaying radius on an inwardly spiraling circle. Fig. 2.10 shows a single turn octagonal inductor with radii labelled. R_0 is the distance from the center to the start of the inductor spiral and will be referred to as the maximum outer radius in this document. R_7 (on top of R_0) is the distance from the center to the end of the first turn of the inductor and will be referred to as the minimum inner radius in this paper. R_7 must be smaller than R_0 by an amount that accounts for the trace width and the spacing between windings. Thus the incremental decrease in radius from corner to corner spiraling inward is $(R_0 - R_7)/8$. The radius to each corner can be found using (EQ 2.9).

$$R_n = R_{n-1} - \frac{R_0 - R_7}{8} \quad (\text{EQ 2.9})$$

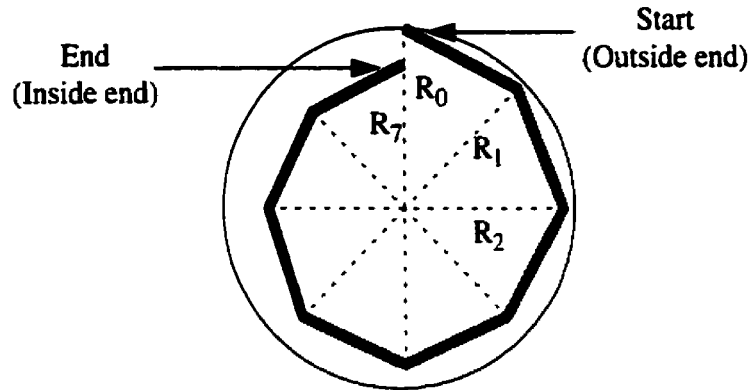


Fig. 2.10: A single turn of an octagonal inductor.

Table 2.2 lists the dimensions of the octagonal inductors fabricated in this study. The 1.0nH and the 0.4nH octagonal inductors had to be lengthened to accommodate the probe pads and feed lines used to measure the inductors (see Fig. 2.11). In the case of the 0.4nH octagonal inductor, 1/16 of a turn had to be added to the beginning (the outside end) of the inductor. In the case of the 1.0nH octagonal inductor, 3/16 of a turn were added for layout reasons. 1/16 of a turn was added to the outside end of the inductor, while 1/8 of a turn was added to the inside end of the inductor.

Target Inductance (nH)	Number of Turns	Maximum Outer Radius (μm)	Min. Inner Radius of Inner Winding (μm)
1.5	2.5	100	65
1.0	2*	100	72
0.5	1.5	80	59
0.4	1.25*	80	62

* indicates inductors that were modified later for layout reasons

Table 2.2: Dimensions of octagonal inductors. Each inductor had a line width of $10\mu\text{m}$, a line spacing of $3\mu\text{m}$, and a clearance of $80\mu\text{m}$ to surrounding metal.

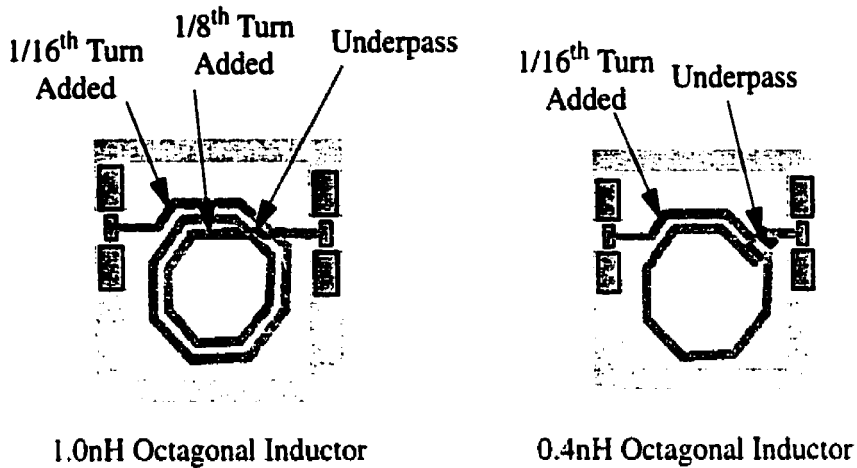


Fig. 2.11: Modifications to the 1.0nH and 0.4nH octagonal inductors. Note the 0.4nH inductor has a shorter and wider underpass than the 1.0nH inductor. It should also be noted that these diagrams are not to scale. The distance between the outer edge of the spiral and the enclosing metal was $80\mu\text{m}$.

2.3.2 Layout of Inductors Studied

All but the 0.4nH and 0.5nH square inductors were fabricated for two port measurements (Fig. 2.12). The 0.4nH and 0.5nH square inductors were fabricated for one port measurements (Fig. 2.18) because a two port layout would have required more chip area than was available. Each inductor had an accompanying set of open and shorted probe pads for de-embedding purposes as shown in Fig. 2.12.

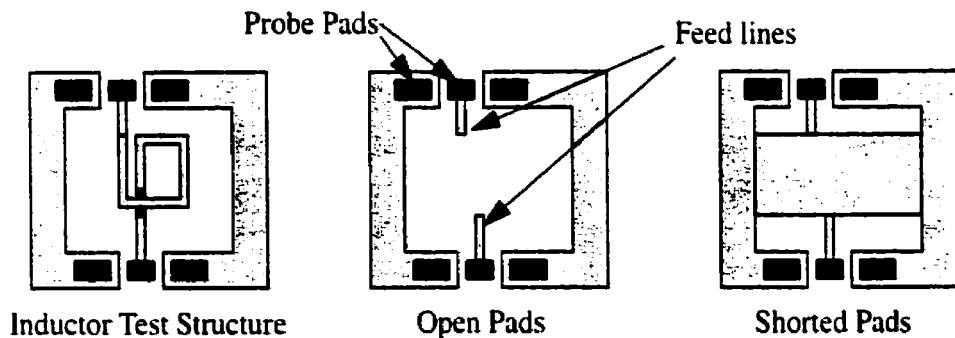


Fig. 2.12: Typical layout of inductors for two port measurements

2.4 Measurement and De-embedding

The probe pads had parasitic capacitances and the feed lines had parasitic resistances and inductances. These parasitics were on the same order of magnitude as the inductor impedances and therefore had to be removed from the measurement through de-embedding. Two different de-embedding methods were employed for the two port inductors, and a third de-embedding method was used for the one port inductors.

2.4.1 The Modified Cho Method of De-embedding

The first of the two port de-embedding techniques was a modified version of the de-embedding technique used by Cho [6] for the measurement of transistors. The original technique used by Cho was based on the measurement of three port devices. The technique used in this work was simplified for two port devices. This modified Cho de-embedding technique assumes the pad and feed line parasitics can be modelled as shown in Fig. 2.13. Measurements of the inductor test structure, the open pads, and the shorted pads (see Fig. 2.12) provide sets of Y parameters: Y_{total} , Y_{open} , and Y_{short} respectively which are used in the modified Cho de-embedding method.

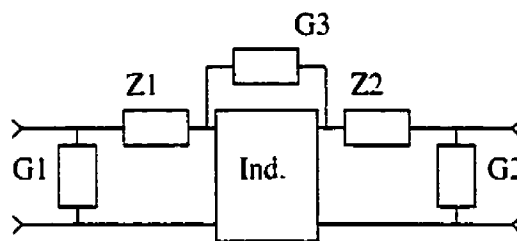


Fig. 2.13: Inductor surrounded by pad and feed line parasitics - modified from Cho's circuit [6].

Fig. 2.13 details the impedances and reactances used to model the pad and feed line parasitics for the modified Cho method. With the inductor in Fig. 2.13 removed, the model (Fig. 2.14) represents the open pad structure shown in Fig. 2.12. Open pad Y parameters provide values for the pad shunt parasitics G1 and G2, and the feed line to feed line coupling parasitic, G3.

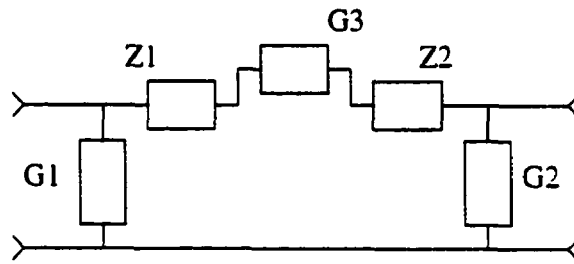


Fig. 2.14: Modified Cho model for open pad parasitics.

If we assume $\frac{1}{G3} = Z1$ and $\frac{1}{G3} = Z2$ then:

$$Y_{11openpads} = G1 + G3 \quad (\text{EQ 2.10})$$

$$Y_{22openpads} = G2 + G3 \quad (\text{EQ 2.11})$$

$$G3 = \frac{-(Y_{21openpads} + Y_{12openpads})}{2} \quad (\text{EQ 2.12})$$

G1 and G2 can be removed from the inductor test structure measurements (Y_{total}) by subtraction.

$$Y_{11a} = Y_{11total} - G1 \quad (\text{EQ 2.13})$$

$$Y_{22a} = Y_{22total} - G2 \quad (\text{EQ 2.14})$$

$$Y_{12a} = Y_{12total} \quad (\text{EQ 2.15})$$

$$y_{21a} = y_{21total} \quad (\text{EQ 2.16})$$

Where the subscript "a" denotes Y parameters for the inductor test structure with G1 and G2 removed.

Y parameters of the shorted pads are used to find Z1 and Z2. The shorted pad circuit model is shown in Fig. 2.15 and was derived by removing the inductor in Fig. 2.13 and grounding both sides of G3.

$$Z1 = (y_{11short} - G1)^{-1} \quad (\text{EQ 2.17})$$

$$Z2 = (y_{22short} - G2)^{-1} \quad (\text{EQ 2.18})$$

The "a" subscripted Y parameters found in (EQ 2.13) - (EQ 2.16) were then converted to "a" subscripted Z parameters through matrix inversion. The series impedances are then removed from the "a" subscripted Z parameters.

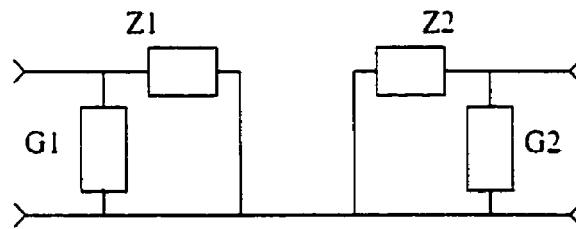


Fig. 2.15: Shorted pad circuit model for the modified Cho method of de-embedding.

$$s_{11b} = s_{11a} - Z1 \quad (\text{EQ 2.19})$$

$$s_{22b} = s_{22a} - Z2 \quad (\text{EQ 2.20})$$

$$s_{12b} = s_{12a} \quad (\text{EQ 2.21})$$

$$z_{21b} = z_{21a} \quad (\text{EQ 2.22})$$

The new set of “b” subscripted Z parameters correspond to the inductor test structure without G1, G2, Z1, and Z2. The Y parameters for the inductor spiral by itself are found by converting Z_b to Y_b through matrix inversion and adding or subtracting G3 as follows:

$$y_{11ind} = y_{11b} - G3 \quad (\text{EQ 2.23})$$

$$y_{12ind} = y_{12b} + G3 \quad (\text{EQ 2.24})$$

$$y_{21ind} = y_{21b} + G3 \quad (\text{EQ 2.25})$$

$$y_{22ind} = y_{22b} - G3 \quad (\text{EQ 2.26})$$

The subscript “ind” refers to the spiral inductor parameters.

A series of MATLAB files were written to implement these equations (and those of the other two de-embedding methods) and are included in Appendix C.

2.4.2 The Modified Koolen Method of De-embedding

The second two port de-embedding method was derived from work by Koolen [5] and uses a two port version of Koolen’s parasitic model for transistor measurements.

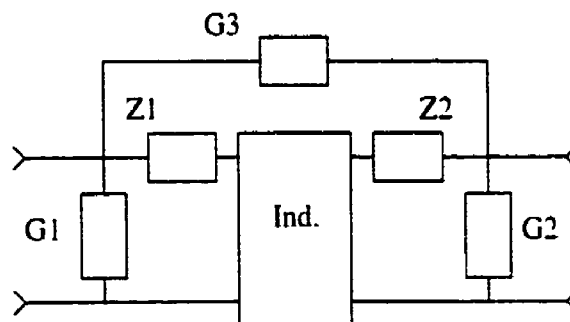


Fig. 2.16: Modified Koolen model of an inductor embedded in pad and feed line parasitics.

The modified Koolen method assumes an equivalent circuit as shown in Fig. 2.16.

Once again open and shorted pads are measured (Fig. 2.17) to determine the Y parameters of the parasitic components. The Y parameters of the spiral inductor without parasitics are found using (see Appendix B for derivation of (EQ 2.27)):

$$Y_{ind} = [(Y_{total} - Y_{open})^{-1} - (Y_{short} - Y_{open})^{-1}]^{-1} \quad (\text{EQ 2.27})$$

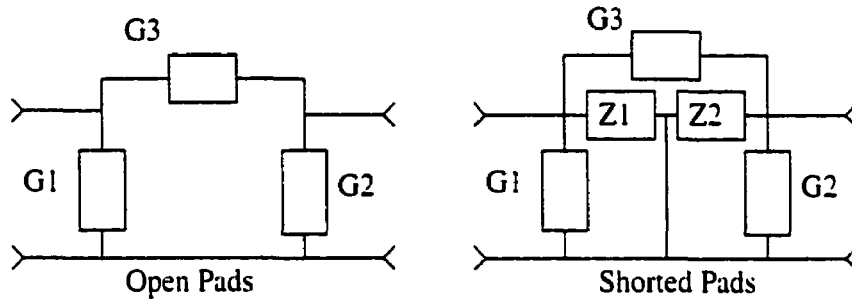


Fig. 2.17: Modified versions of Koolen's open and short pad parasitics models.

2.4.3 One Port Inductor De-embedding

As mentioned previously the 0.4nH and 0.5nH square inductors were fabricated for one port measurements (Fig. 2.18). Open pads were also fabricated to provide data for the feed line de-embedding process. Due to chip area constraints, shorted pads were not fabricated. Only the feed line parasitics were de-embedded from the inductor measurements on the one port inductors. The grounding lines for the one port spirals were left as part of the inductor measurements.

Fig. 2.19 shows the one port inductor test structure circuit model including pad and feed line parasitics. $G1$ represents the shunt impedance and $Z1$ the series impedance of the feed line from the probe pads. $Z2$ represents the grounding line series impedance that remained part of the inductor measurement. $G1$ was found from the y_{11open} measurement

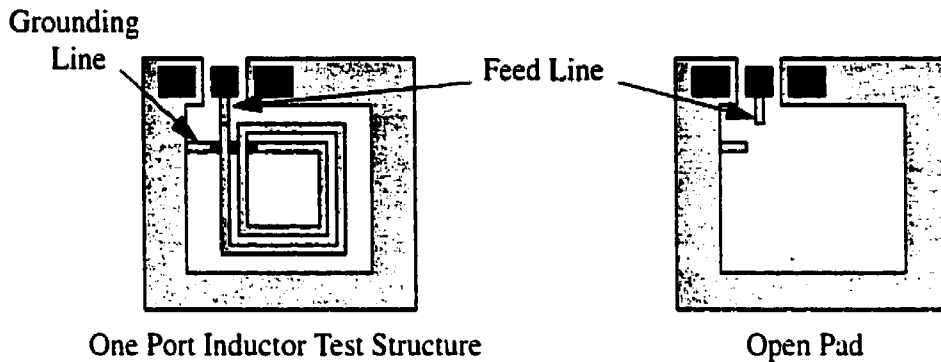


Fig. 2.18: One port inductor test structure and open pad layout.

of the open pad structure. $Z1$ was estimated using HP EEsof Series IV. To ensure accurate results, the open pad was first simulated and the simulator substrate parameters optimized such that the simulated results matched the measured open pad results. Using the opti-

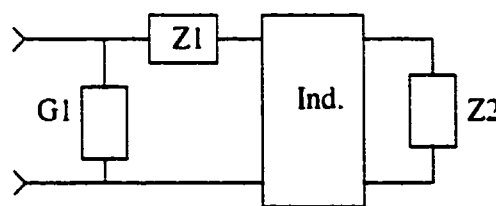


Fig. 2.19: One port inductor with surrounding parasitics.

mized substrate parameters ($\epsilon_r = 11.7$, substrate thickness = $80\mu\text{m}$, metal thickness = $3\mu\text{m}$, and loss tangent = 0.25) the shorted pad was simulated and $Z1$ extracted. The impedance of the inductor was then determined from:

$$z_{in} = (y_{11total} - G1)^{-1} - Z1 \quad \text{(EQ 2.28)}$$

It is important to note that because the above mentioned values of substrate thickness and loss tangent were used as fitting parameters, they do not represent actual physical values.

2.5 Summary

This chapter discussed the characteristics of on-silicon spiral inductors. The effects of inductor design parameters such as line spacing and line width were also discussed. Two fabrication techniques which have the potential of augmenting inductor Q were presented. The design of eight inductors to be fabricated using the two techniques was also presented. The final part of the chapter described the methods by which inductor characteristics were to be extracted from on-wafer measurements. The following chapter discusses the measured results of the fabricated inductors.

CHAPTER 3: Inductor Measurement and Results

The inductors presented in Chapter 2 were fabricated in the Nortel Networks NT55 process [25]. The inductors were then measured on wafer using an Alessi S3-APRB wafer probing station. Wafer probing was conducted using two 40A-GSG-175-DP wafer probes from GGB Industries. S-parameter measurements were made using an HP8510C network analyzer with an HP8517B S-parameter test set. Anritsu K118 semi-rigid co-axial cable was used to connect the probes to the HP8517B as shown in Fig. 3.1. All measurements were taken over the frequency range of 1GHz to 40GHz. The measurement system was calibrated up to the probe tips using a GGB Industries CS-5 calibration substrate. Each inductor had associated open and shorted pads that were measured along with the inductor in order to facilitate de-embedding of pad parasitics.

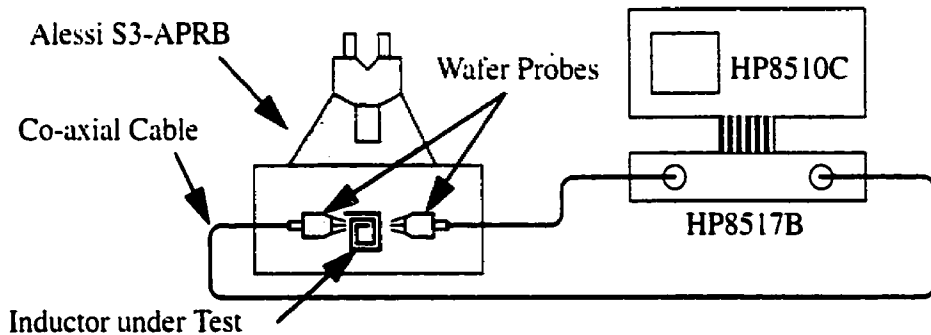


Fig. 3.1: Inductor measurement setup configuration.

A series of MATLAB M-files were written to perform the de-embedding procedures outlined in Chapter 2. The MATLAB code performs a series of steps, shown in Fig. 3.2, to obtain Q and L values for a spiral, given raw S-parameter data of the inductor test struc-

ture, the open pads, and the shorted pads. The first step is to convert all the S-parameter data to Y-parameters, since the de-embedding methods described in Chapter 2 pertain to Y-parameters. The next step is to perform the actual de-embedding of the spiral inductor from the pad and feedline parasitics using either the modified Koolen, modified Cho, or 1-port method. The two port Y-parameter network describing the spiral inductor is then used to find the input impedance to the spiral inductor (Z_{in}) with the underpass side grounded (the connection of intended use in the oscillator work). L and Q values can be calculated from Z_{in} using the equations in Fig. 3.2. The code used to perform these steps in MATLAB is given in Appendix C.

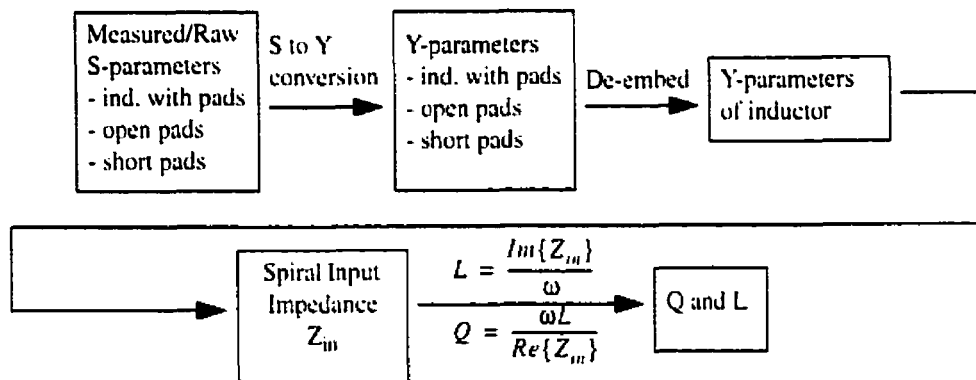


Fig. 3.2: Flow chart describing the steps the de-embedding code performs to obtain L and Q for the spiral inductor from measured S-parameter data.

3.1 Inductor Measurement Results

The following table lists the inductor sizes and how many sets of each were measured. In this study, a set refers to one basic, one 2-metal, and one trench inductor version. The inductor versions are described in Chapter 2.

Inductor	Number of Sets Measured
0.4 octagonal	9
0.5 octagonal	10
1.0 octagonal	11
1.5 octagonal	9
0.4 square	10
0.5 square	10
1.0 square	11
1.5 square	10

Table 3.1: Inductor sizes and number measured.

The following tables show measured results for each inductor, averaged over the number of samples measured.

De-embed Method	Target Ind. (nH)	Basic			2 Metal			Trench		
		L (nH)	Q	Peak Q Freq	L (nH)	Q	Peak Q Freq	L (nH)	Q	Peak Q Freq
Koolen	1.0	1.01	10.7	7GHz	0.95	9.3	6GHz	1.0	10.7	7GHz
Koolen	1.5	1.32	10	5.2GHz	1.26	9.1	4.6GHz	1.34	9.9	5.2GHz
Cho	1.0	1.0	10.7	7GHz	0.94	9.2	6GHz	1.0	10.7	7GHz
Cho	1.5	1.32	10	5.2GHz	1.26	9.1	4.6GHz	1.33	9.9	5.2GHz

Table 3.2: Average measured results of the two port square inductors.

De-embed Method	Target Ind. (nH)	Basic			2 Metal			Trench		
		L (nH)	Q	Peak Q Freq	L (nH)	Q	Peak Q Freq	L (nH)	Q	Peak Q Freq
Koolen	0.4	0.46	22.5	15GHz	0.44	19	15GHz	0.46	25	15GHz
Koolen	0.5	0.53	17	11GHz	0.50	15.5	11GHz	0.53	17	12GHz
Koolen	1.0	1.42	12	4.8GHz	1.36	9.8	4.4GHz	1.41	11.9	4.4GHz
Koolen	1.5	1.41	12.7	5GHz	1.34	11.8	4.4GHz	1.40	12.5	5GHz
Cho	0.4	0.45	19	15GHz	0.43	16.5	15GHz	0.45	20	15GHz
Cho	0.5	0.52	16	11GHz	0.50	14.5	11GHz	0.52	16.1	11GHz
Cho	1.0	1.42	12	4.8GHz	1.36	10.1	4.4GHz	1.4	11.9	4.4GHz
Cho	1.5	1.40	12.7	5GHz	1.34	11.7	4.4GHz	1.40	12.5	5GHz

Table 3.3: Average measured results of the octagonal inductors (all two port).

De-embed Method	Target Ind. (nH)	Basic			2 Metal			Trench		
		L (nH)	Q	Peak Q Freq	L (nH)	Q	Peak Q Freq	L (nH)	Q	Peak Q Freq
1 Port	0.4	0.54	11.7	10.5GHz	0.51	9.8	10.5GHz	0.54	11.9	10.5GHz
1 Port	0.5	0.58	11.3	10.5GHz	0.55	9.3	10.5GHz	0.58	11.3	10.5GHz

Table 3.4: Average measured results for one port square inductors.

It should be noted that the peak Q and peak Q frequency of the 0.4nH octagonal trench inductor were difficult to discern (as shown by the plot in Fig. 3.13). The peak Q frequency was therefore considered to be 15GHz - the peak Q frequency value of the 0.4nH octagonal basic inductor.

The "target inductance" values are used in the rest of this document as a designator when referring to a particular inductor.

The plots in Fig. 3.6, Fig. 3.7, and Fig. 3.10 - Fig. 3.13 show average values of inductance and Q for each two port inductor found using the modified Cho method of de-embedding. Plots of the same data obtained through the modified Koolen de-embedding method are similar in shape, and the differences between the results obtained using each method are captured in Table 3.2 and Table 3.3. The plots in Fig. 3.8 and Fig. 3.9 show results for the one port inductors, obtained using the one port de-embedding method. Average measured values of key parameters for the one port inductors are presented in Table 3.4.

Each inductance curve exhibits a nearly flat region followed by a steep upwardly curved region. A steep downward curved region is also present for inductors whose self resonant frequencies were within the 1GHz - 40GHz measurement range. These inductance curve characteristics result from the interaction between the inductance and the parasitic capacitances present in the spiral as discussed in Chapter 2. The relatively flat initial part of the trace shows that the inductive portion of the spiral dominates. When the inductance trace curves upward, it indicates that the inductance of the spiral and the parasitic capacitance of the spiral are approaching resonance. The inductance trace then reaches a peak and drops off rapidly, passing through zero, to a minimum value. The point where the inductance is zero is the self resonant frequency of the spiral. When the inductance curve drops below zero, the parasitic capacitance dominates, and the spiral has effectively become a capacitor. It should be noted that spiral inductors typically exhibit many self

resonant frequency points. The present study is limited to behaviour up to the first self resonant frequency.

All the Q curves start at a low value, rise to a peak, and drop off. If the self resonant frequency of the spiral is within the measurement range, Q will fall toward zero. Quality factor is determined by the inductance and the losses of the spiral through the relation

$$Q = \frac{\omega L}{R} \quad (\text{EQ 3.1})$$

derived in Chapter 2, where L is the inductance looking into the terminals of the spiral at a particular frequency, and R is the resistance looking into the spiral terminals at the same frequency. The circuit in Fig. 3.3 is assumed in (EQ 3.1) and is valid only before self resonance at the frequency which L and R are found.

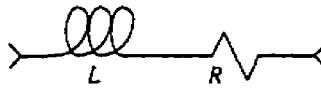


Fig. 3.3: Inductor with loss for calculation of Q .

The frequency at which each Q curve reaches its peak is in the relatively flat portion of the inductance trace. The initial rise in Q results from ωL increasing with frequency faster than R . In the initial, relatively flat portion of the inductance curve, series winding losses dominate which can be approximated by [20]

$$R_s = \frac{l}{\omega \sigma \delta (1 - e^{-l/\delta})} \quad (\text{EQ 3.2})$$

where w is the width of the inductor winding (Fig. 3.5), l is the overall length of the inductor, σ is the conductivity of the winding metal, t is the thickness of the winding, and δ is the skin depth as given by (EQ 2.8). (EQ 3.2) and ωL are plotted together in Fig. 3.4, showing that ωL increases more rapidly with frequency than R_s .

Beyond the initial flat region of the inductance curve, one may expect Q to increase since ωL increases faster than R_s . However, this is not the case. Q rolls off as the slope of the inductance curve increases, indicating a rise in substrate losses, which eventually become the dominant source of spiral inductor loss.

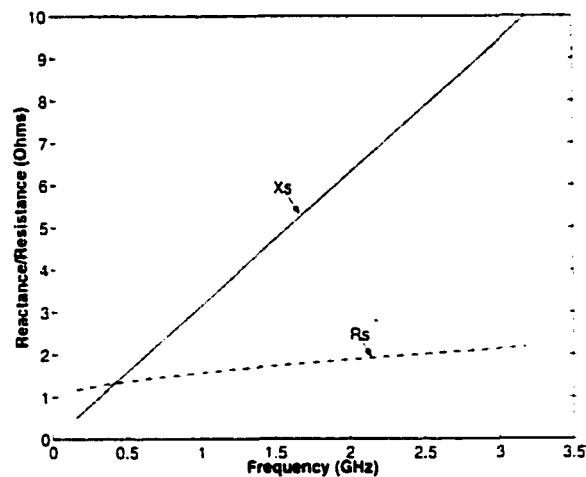


Fig. 3.4: Series resistance (R_s) and series reactance ($X_s = \omega L$) over frequency for inductor with $w = 10\mu m$, $L = 1000\mu m$, $\sigma = 3.54 \times 10^7 S/m$, and $\mu = \mu_0$.

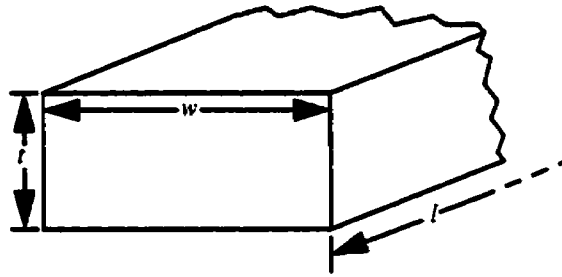


Fig. 3.5: Segment of an inductor winding.

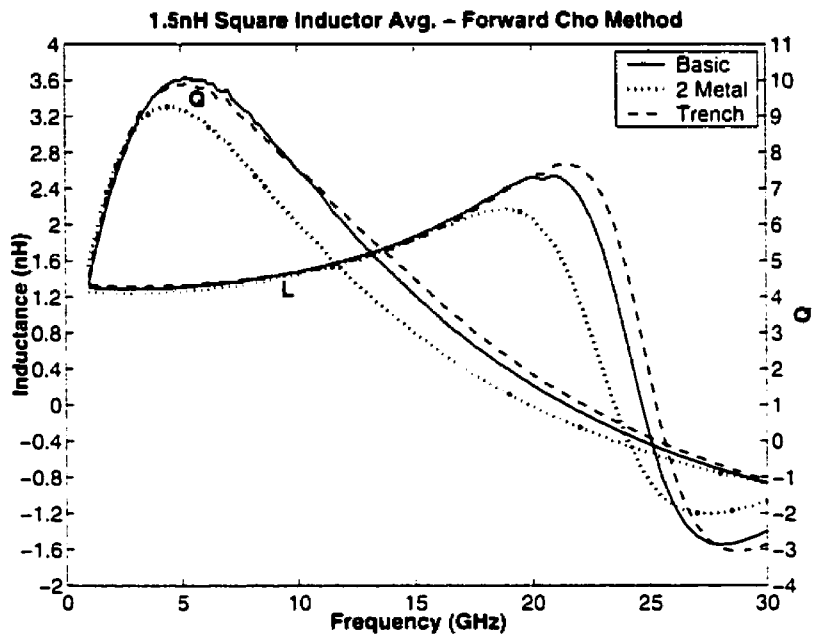


Fig. 3.6: Plot of each type of 1.5nH square inductor - average of 10 samples.

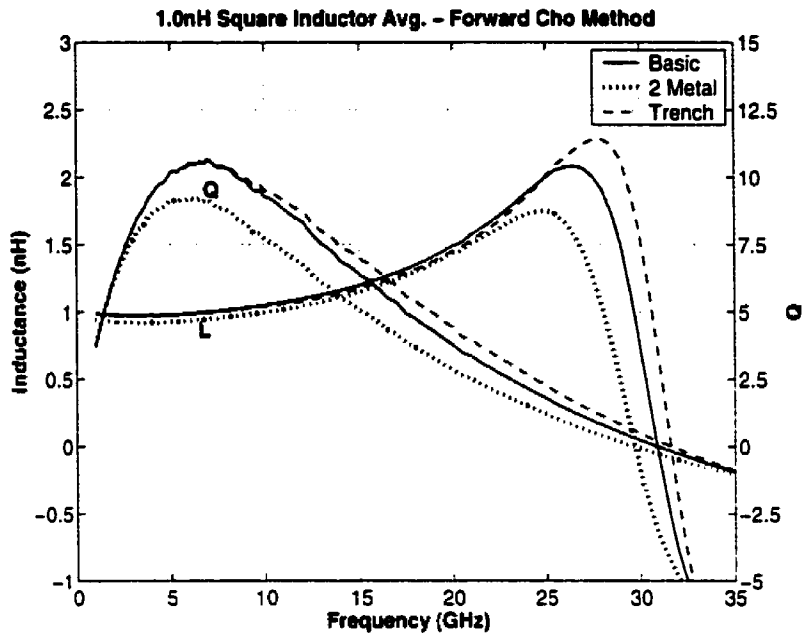


Fig. 3.7: Plots of each type of 1.0nH square inductor - average of 11 samples.

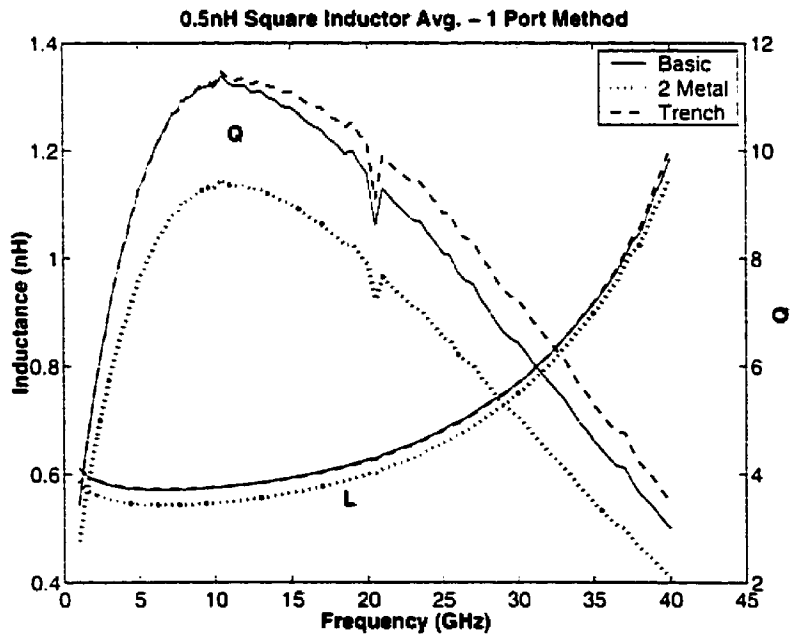


Fig. 3.8: Plot of each type of 0.5nH square inductor - average of 10 samples.

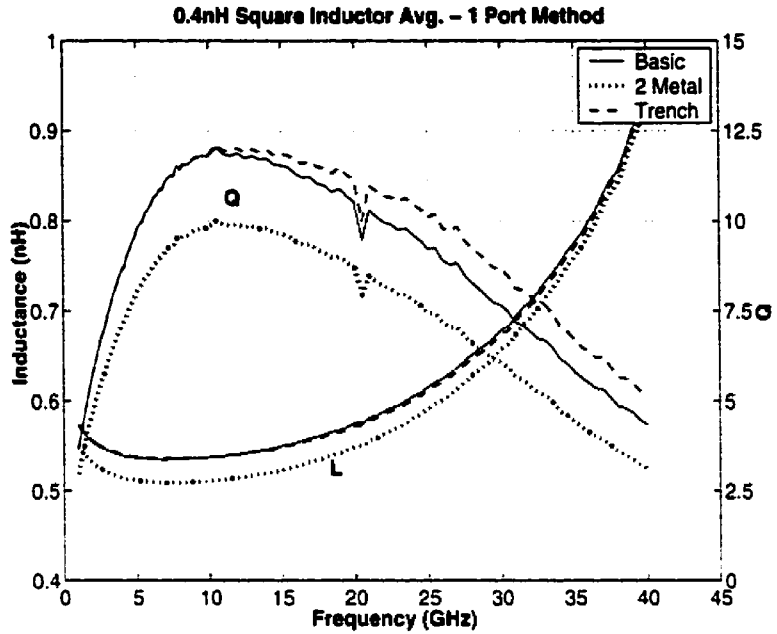


Fig. 3.9: Plots of each type of 0.4nH square inductor - average of 10 samples.

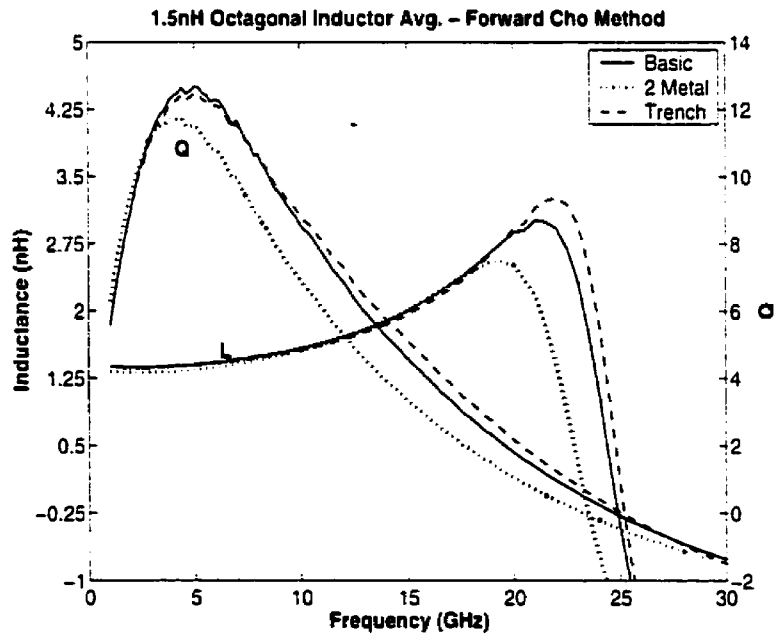


Fig. 3.10: Plot of each type of 1.5nH octagonal inductor - average of 9 samples.

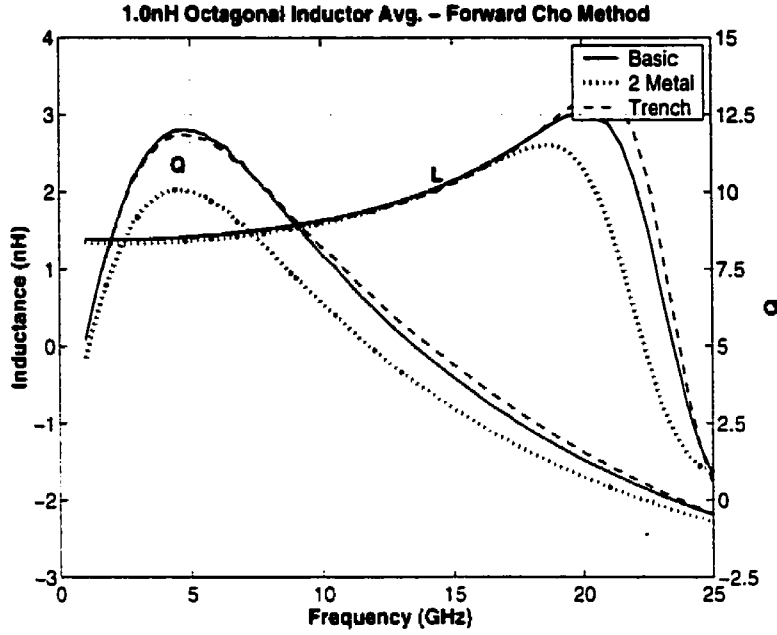


Fig. 3.11: Plots of each type of 1.0nH octagonal inductor - average of 11 samples.

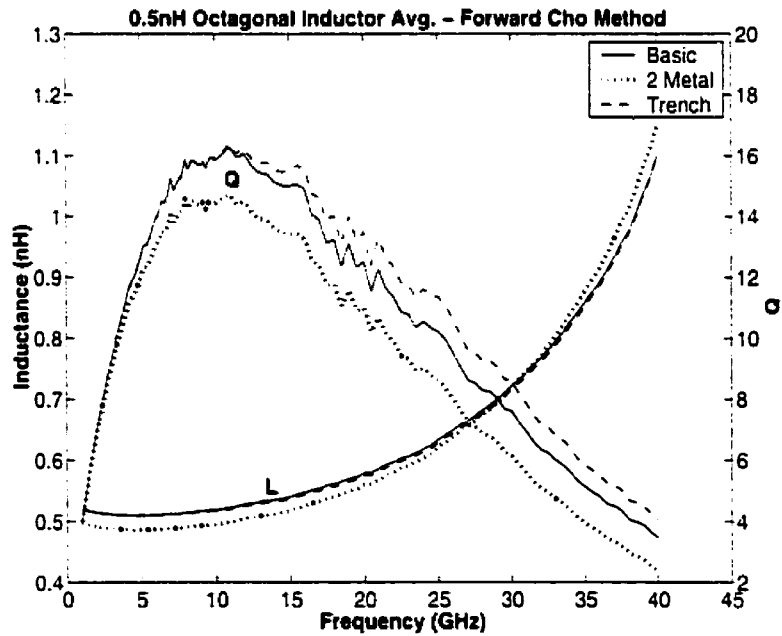


Fig. 3.12: Plot of each type of 0.5nH octagonal inductor - average of 10 samples.

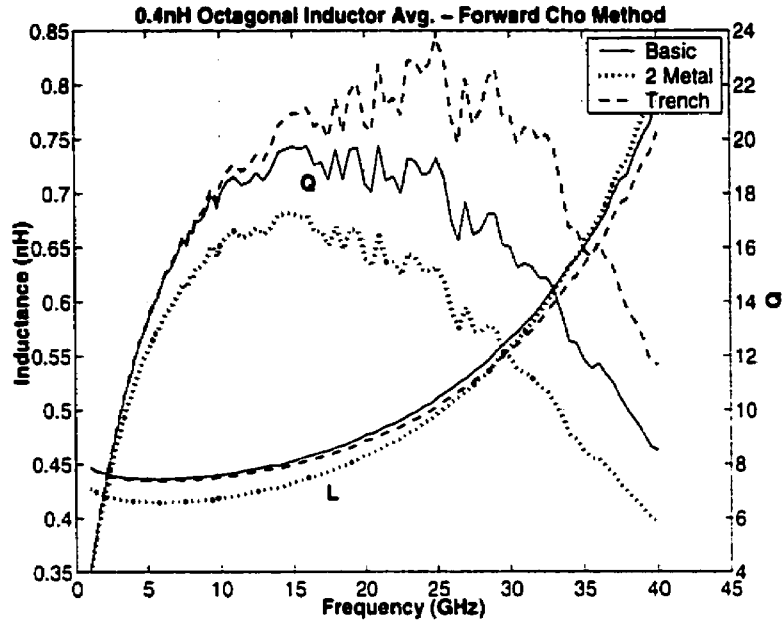


Fig. 3.13: Plot of each type of 0.4nH octagonal inductor - average of 9 samples.

3.1.1 Inductor Measurement Error

The primary source of error in the inductor measurements was due to inconsistency in the way the probes contacted the aluminum probe pads. Aluminum is not an ideal probe pad material as a thin layer of aluminum oxide forms on the surface of the pad which must be pierced in order to obtain proper contact. This meant a larger downward force on the probe pads, compared to that required for gold pads, was required to obtain a good low resistivity contact. The amount of z-direction adjustment required on the probes to achieve electrical contact was not consistent across the wafer.

Probe contact resistance can substantially affect the Q of an inductor as the following case illustrates. Using the Q and L values for the 0.5nH octagonal inductor, R in (EQ 3.1)

is

$$R = \frac{\omega L}{Q} = \frac{2\pi(11 \times 10^9)(0.52 \times 10^{-9})}{16} = 2.2 \Omega \quad (\text{EQ 3.3})$$

where R is the losses looking into the spiral inductor. Clearly a few hundred milliohms of contact resistance will significantly affect the spiral's measured losses.

To minimize the effect of the inconsistent probe contact problem, each inductor test structure was placed along side its open and shorted pad structures in a cluster (Fig. 3.14). Clusters were distributed across the wafer area. Each structure in a cluster was measured by hopping a short distance from one set of pads to the next.

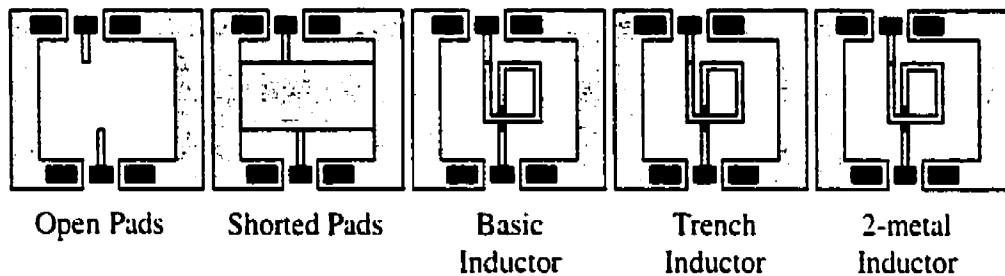


Fig. 3.14: A cluster of test structures for a square inductor.

The probe z-axis setting was adjusted once for the first pads in a cluster and then left unchanged for the remaining measurements in the cluster, meaning each measurement in the cluster would experience similar contact resistances. These contact resistances can be considered part of the feedline parasitic resistance and were, ideally, removed from the spiral inductor measurement when the pad and feedline impedances were subtracted from the inductor test structure measurements.

To verify the consistency of the measurements, a 0.5nH and a 1.0nH inductor were selected to be measured on four separate occasions. Since the results of the 0.5nH inductor showed the highest variation, they are presented in Table 3.5.

Analysis of the measurement error data presented in Table 3.5 indicates that the maximum error in peak Q was 7%, the maximum error in peak Q frequency was 10%, and the maximum error in inductance at the peak Q frequency was 2%. The variations in peak Q and peak Q frequency are attributable to inconsistencies in the probe contact resistance. Inductance which is relatively insensitive to contact resistance variations showed a much smaller maximum error. While the sample set was relatively small, the numbers presented in Table 3.5 provide a rough error figure for the key inductor parameters presented in this document.

Trial #	Peak Q	Peak Q Frequency	Inductance at Peak Q Frequency
1	16.0	11 GHz	0.52nH
2	16.3	10GHz	0.52nH
3	15.2	11GHz	0.52nH
4	15.2	11GHz	0.53nH

Table 3.5: Four measurements of the same 0.5nH octagonal inductor.

3.2 Discussion of Inductor Results

The following sections discuss the results given in Table 3.2, Table 3.3, and Table 3.4, as well as the plotted results in Fig. 3.6 to Fig. 3.13.

3.2.1 Comparison of Modified Koolen and Modified Cho De-embedding Methods

Obtaining accurate measurements of any on-chip component is complicated by the probe pads that provide the connection between the component and the measurement probes. Pad and feedline parasitics must be de-embedded from the measurement. Chapter 2 explains in detail the three (modified Koolen, modified Cho, and 1-port) de-embedding methods used in this study. Results using each method are compared and discussed in this section. It is not possible at this time, however, to make any conclusion regarding which of the two methods is more accurate.

Referring to Table 3.2 and Table 3.3 some differences between the modified Koolen and modified Cho method are evident. In de-embedding the 1.0nH and 1.5nH square and octagonal inductors, the two methods differed by a maximum of 1% in L, as seen with the 1.0nH square inductor: by a maximum of 7% in Q, as seen with the 1.5nH square inductor: and undetectably in peak Q frequency. De-embedding the 0.4nH and 0.5nH inductors using the two methods yielded a maximum 20% difference in peak Q, demonstrated by the 0.4nH octagonal trench inductor, and a maximum 2% difference in L as demonstrated by the 0.4nH octagonal two metal inductor. The measurements in Table 3.2 through Table 3.4 were taken at the peak Q frequency which, as can be seen in Fig. 3.15, is where the difference between the Q curves of the two de-embedding methods is at its maximum. Differences in the inductance curves are small over the frequency range of measurement.

The difference in Q curves can not be attributed simply to the small differences in inductance. (EQ 3.1) shows that Q is directly proportional to L and therefore the 2% dif-

ference in inductance for the 0.4nH octagonal inductor does not account for the 20% difference in Q. The reason for the discrepancies in Q must therefore be in how each method accounts for losses, modelled as resistance in the denominator of (EQ 3.1).

The differences between the two de-embedding methods are more significant with the smaller (0.4nH and 0.5nH) inductors than with the larger (1.0nH and 1.5nH) inductors. The smaller inductors had a lower impedance when compared to the larger inductors but the pads were the same size for all the inductors. Thus pad and feed line parasitics were a more significant factor when measuring the impedance of the smaller, 0.4nH and 0.5nH, inductors than for the larger, 1.0nH and 1.5nH, inductors. Because the pad and feedline parasitics were a more significant factor, differences between the Koolen and Cho methods in removing these parasitics formed a more significant portion of the smaller inductor final results.

Beyond the peak Q frequency, Q curves from each de-embedding method approach each other, but do not become co-incident as they were before the peak. The two methods assume different lumped element models for the feed line and pad parasitics which become less accurate as frequency increases. Because the two models make different assumptions, they break down in different ways, leading to the small difference between the Q curves beyond the peak Q frequency.

The differences between these two de-embedding methods are significant and demonstrate the need for further study in this area. The modified Cho method of de-embedding

provided lower peak Q values for each inductor. Since neither method of de-embedding has been proven to be more accurate than the other, the more conservative results (those obtained using the modified Cho method) are used throughout the remainder of this document unless otherwise stated.

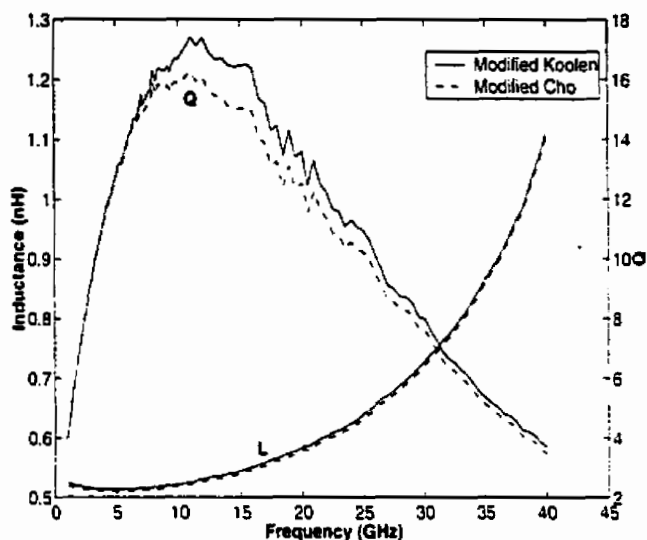


Fig. 3.15: Q and L curves of the basic 0.5nH octagonal inductor using the two de-embedding methods.

3.2.2 Effect of Using Two Metal Layers to Fabricate Inductor Windings

The 2-metal inductor layout was expected to show an improvement in Q over the control inductor (basic inductor) layout because of the reduction in series winding resistance provided by the second metal layer. The results, however, showed the 2-metal inductors had a lower (7% to 18%) Q than the basic inductor versions. The use of metal layers beneath the top metal layer brought the inductor closer to the under-lying lossy silicon substrate, increasing substrate losses through higher capacitive and inductive coupling. As well, the 2-metal inductors could not make use of second metal layer underpasses as

did the basic and trench inductors. Underpasses for the 2-metal inductors were created in the bottom metal (highest resistivity) layer, adding to the series losses.

The 2-metal inductors also demonstrated inductance values that were 4% to 7% lower when compared to the basic inductors. Adding the second metal layer to the windings increased the inter-winding capacitance of the inductors, and increased the winding capacitance to the grounded substrate. These increased capacitances served to decrease the overall inductance of the spiral. The closer proximity of the 2-metal spirals to the silicon substrate also lead to greater inductive coupling between current flowing in the inductor windings and mirrored currents flowing in the substrate, further reducing the overall inductance of the 2-metal spirals.

Plots of the 1.0nH and 1.5nH square and octagonal inductor results (Fig. 3.6, Fig. 3.7, Fig. 3.10, and Fig. 3.11) indicate the 2-metal inductors had a SRF on the order of 4% lower than the SRF of the basic inductor versions. As discussed above, the 2-metal spirals had higher parasitic capacitances, which lead to the lower demonstrated self resonant frequencies.

3.2.3 Effect of Trench on Inductor Performance

In general the trench inductors performed similarly to the basic inductors. SRF was on average slightly higher as shown in Table 3.6. The plots shown in Fig. 3.6 through Fig. 3.13 show that the trench inductor Q roll-off at frequencies above the peak Q fre-

quency was more gradual than in the case of the basic inductors. Trench inductor peak Q values were, in general, close to those of the basic inductors.

Starting at or beyond the peak Q frequency the results show trench inductor Qs to be higher than basic inductor Qs. The 0.4nH trench inductor showed a Q increase of >5% at 15GHz compared to the 0.4nH basic inductor; this result is shown in Fig. 3.13. The trenches are an insulating barrier which impede the inter-winding current flow shown in Fig. 2.2. This current not only produces ohmic loss, but also reduces the overall inductance of the spiral. Improvement in Q was therefore expected at higher frequencies where substrate losses dominate. However, it is not possible, at this time, to determine if there is a relationship between the peak Q frequency and the frequency at which the trenches seem to produce a higher Q.

Table 3.6 summarizes the effect that the trenches have on SRF. Only SRF values for the 1.0nH and 1.5nH inductors are provided because the smaller inductor values had SRFs higher than the 40GHz bandwidth of the network analyzer used to measure the inductors.

Target L (nH)	Ind. Shape	SRF (GHz) Basic	SRF (GHz) Trench
1.5	Square	24.5	25
1.5	Octagonal	24.5	25
1.0	Square	31	31.5
1.0	Octagonal	23.5	23.5

Table 3.6: Measured average self resonant frequencies of inductors with $L > 0.5$ nH

The data suggests the presence of trenches increases the SRF of the spiral by a small amount (0.5GHz in most cases). This can be attributed to the increase in inter-winding

impedance introduced by the trenches. Greater inter-winding impedance, means less capacitive coupling between the windings (lower C_p in Fig. 2.3), and therefore increases the self resonant frequency.

3.2.4 Effect of Inductor Size on Performance

The small inductors (0.4nH and 0.5nH) had a shorter overall trace length and a smaller overall surface area compared to the 1.0nH and 1.5nH inductors. The shorter trace length leads to a lower overall inductance; and the smaller surface area leads to less capacitive coupling to the substrate. Both the smaller inductance and the lower substrate capacitance push the SRF and the peak Q frequency higher as observed in the results (Table 3.2, Table 3.3, and Table 3.4).

3.2.5 Effect of Inductor Shape on Performance

Circular and octagonal spiral inductors have shown up to 10% lower series losses when compared to square inductors of the same inductance value [10]. Square inductors have abrupt discontinuities at the corners which lead to losses due to current crowding and more capacitive coupling to the substrate. Circular inductors have no discontinuities and therefore do not suffer from spurious mode effects. While octagonal inductors also have discontinuities at each corner, the discontinuities are not as sharp as in the case of the square inductors. Generally the performance of octagonal inductors is comparable to that of circular inductors.

Square inductors are popular because they occupy less chip area than circular and octagonal inductors, and can be produced in any silicon IC fabrication process. Many semi-conductor fabrication processes are unable to resolve curved shapes and therefore do not permit circular spirals. For this reason octagonal inductors are often used, as they are acceptable to most fabrication processes but provide performance comparable to that of circular inductors.

The highest Q inductor in this study was an octagonal 0.4nH trench inductor with a Q of 20 at 15GHz which, to the author's knowledge, is the highest reported Q for an on-silicon spiral inductor fabricated in a standard production process.

3.3 Spiral Inductor Simulation

At the beginning of this research work target inductance values of 0.4nH, 0.5nH, 1.0nH, and 1.5nH were selected as these inductance values were of initial interest for potential future oscillator work. Chapter 4 discusses an oscillator that uses the 0.5nH octagonal trench inductor.

The inductors were drawn and simulated using the HP EEsof Series IV layout tool and HP EEsof Series IV Momentum (a method of moments EM simulator) respectively. Through an iterative process of simulation and modification, dimensions for each inductor were found that, in simulation, provided the target inductance values and $Q > 15$.

3.3.1 Octagonal Inductor Simulation

When simulating the special case of closely spaced vertically stacked metal traces, the Momentum simulator required its analysis mesh to be exactly the same on each of the closely spaced layers. Due to the close spacing between the bottom of the inductor windings and the underpass metal (1 μ m), the analysis mesh had to be manually drawn on and near the underpass in order to make the meshing on the windings match the meshing on the underpass. While this technique worked well for the square inductors whose vertices fell on the drawing grid of the layout tool, the octagonal inductors had vertices off the drawing grid of the Libra layout tool. This made the process of defining the Momentum analysis mesh very difficult as it had to be drawn without the benefit of grid snapping. As a result, the Momentum generated analysis mesh was not correctly generated on and near the underpass for the octagonal inductors. Thus the underpasses were left out of the simulation of the octagonal inductors. Octagonal inductor simulation results were not taken to be accurate, and were only used as a rough guide in selecting the octagonal inductor dimensions given in Table 2.2. Simulation results for the octagonal inductors are therefore not presented here.

It is also important to note that the 0.4nH and 1.0nH octagonal inductors were modified, as discussed in Section 2.3.1, to simplify the layout, which added further differences between the simulated structure and the measured structure.

3.3.2 Comparison of Square Inductor Simulations and Measurements

Each of the square inductors was simulated in its final form after fabrication using HP ADS version 1.1 Momentum which is a later version of Series IV Libra Momentum. The switch from Libra to ADS had to be made due to an intermittent bug in Libra Momentum that would not allow user defined analysis mesh generation. The material parameters that were used in all the electromagnetic simulations are given in Table 3.7.

Element	Parameter	Value
Substrate	thickness	380 μ m
	bulk resistivity	10 Ω cm
	ϵ_r	11.7
Oxide Layer	thickness	4.8 μ m
	ϵ_r	3.9
	loss tangent	0
Top Metal	resistivity	10m Ω /square
	height above substrate	4.8 μ m
Second metal (for underpass)	resistivity	30m Ω /square
	height above substrate	3.3 μ m

Table 3.7: Material values used in HP EEs of Momentum for each inductor.

Inductor	Q_{peak}		F_{peak} (Q_{peak} Frequency)		L at F_{peak}		SRF	
	Sim.	Meas.	Sim.	Meas.	Sim.	Meas.	Sim.	Meas.
0.4nH	23	12	19GHz	10.5GHz	0.43nH	0.54nH	>>*	>>
0.5nH	20	11	13GHz	10.5GHz	0.51nH	0.58nH	>>	>>
1.0nH	16	11	6.5GHz	7GHz	1.05nH	1.0nH	36GHz	31GHz
1.5nH	15	10	5GHz	5GHz	1.44nH	1.31nH	30GHz	24.5GHz

* the symbol >> means the SRF was beyond the 40GHz range of the test equipment

Table 3.8: Simulated and measured parameters for the basic square inductors.

Table 3.8 shows key simulated and measured parameters for each of the basic square inductors. The data in Table 3.8 is taken from the plots given in Fig. 3.17 to Fig. 3.20 which show simulated and measured Q and L values. Note the plot of simulated 0.4nH square inductor results (Fig. 3.20) shows anomalous values between 2GHz and 7GHz. Repeated simulations provided the same anomalous results. These values were considered inaccurate; however it is not clear why ADS Momentum generated these anomalous results.

As can be seen from the data in Table 3.8 there were significant differences between the simulated and measured parameters for each inductor with the greatest differences found in the 0.4nH inductor results. For the 0.4nH inductor the simulated peak Q was 92% above the measured Q, and the simulated inductance was 20% lower than the measured. The smallest differences between simulated and measured data were found in the 1.0nH inductor results. For the 1.0nH inductor, simulated peak Q was 45% higher than the measured peak Q, simulated inductance was very close to the measured inductance with a 5% deviation, and the simulated SRF was 16% higher than the measured.

In each case the simulator provided a higher SRF and peak Q than was measured. The discrepancies in simulated and measured data were attributed to assumptions made in the simulator code. The most significant of these assumptions was the modelling of all metal layers as two dimensional structures (zero thickness). This led to inaccuracies in three areas: the capacitance between windings, the capacitance between the windings and the underpass metal, and the resistance of the windings.

The two dimensional nature of the simulated winding metal permitted for only fringe capacitance between the windings. The winding metal was in reality $3\mu\text{m}$ thick and the windings were spaced $3\mu\text{m}$ apart. The one to one ratio between winding spacing and winding thickness suggests that parallel plate capacitance was not negligible, which contributed to the overall error in estimating the self resonant frequency of the spiral.

By discounting the conductor thickness, the simulator increased the distance between the windings and the underpass as shown in Fig. 3.16. The actual physical structure has a top metal to underpass metal spacing of approximately $1.2\mu\text{m}$ [25]. The simulator neglects the thickness of the underpass thereby placing it $2.2\mu\text{m}$ beneath the top metal layer. Assuming only parallel plate capacitance between the windings and the underpass. (EQ 3.4) shows the extra distance drops the winding to underpass capacitance by 45%.

$$\frac{C_{\text{simulated}}}{C_{\text{actual}}} = \frac{\left(\frac{\epsilon A}{1.2\mu\text{m}}\right)}{\left(\frac{\epsilon A}{2.2\mu\text{m}}\right)} = 0.55 \quad (\text{EQ 3.4})$$

The assumption of infinitesimal metal thickness also created errors in estimating the winding losses. Because the metal had zero depth, the EM simulator was unable to consider skin effects in the windings. The simulator used a simple user provided sheet resistance value to calculate winding losses. As provided by [25], the top metal sheet resistance was $10\text{m}\Omega$ per square, and the underpass metal sheet resistance was $30\text{m}\Omega$ per

square. The sheet resistance values reflect the DC resistance and do not account for skin effect.

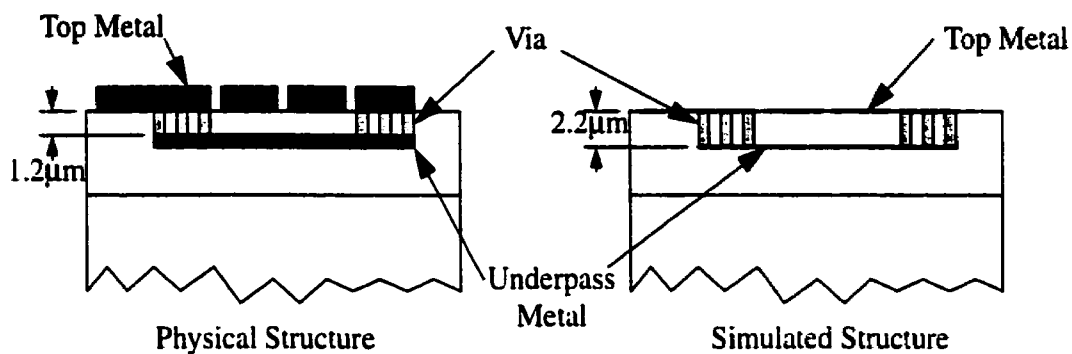


Fig. 3.16: Cross section views of simulator metallization layering and actual physical metallization layering, for underpass portion of inductor.

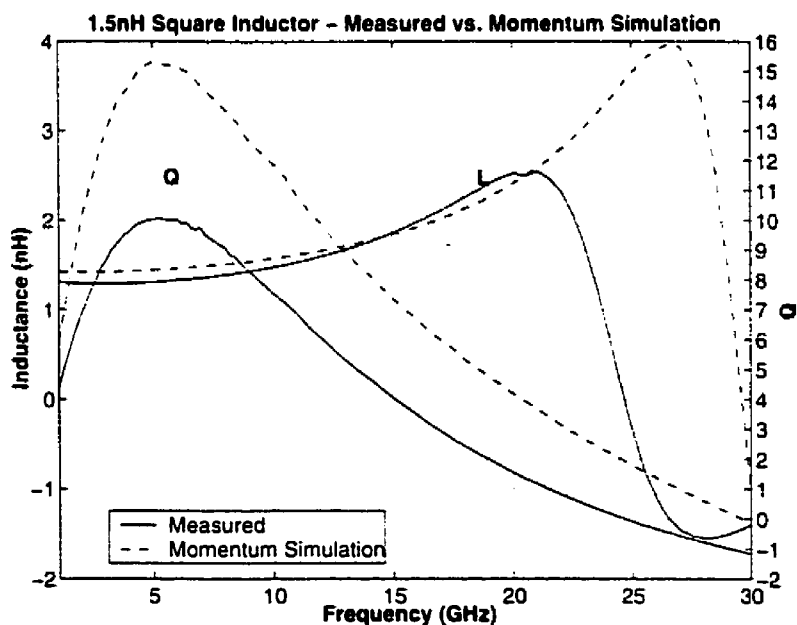


Fig. 3.17: Measured and simulated data for the 1.5nH square inductor.

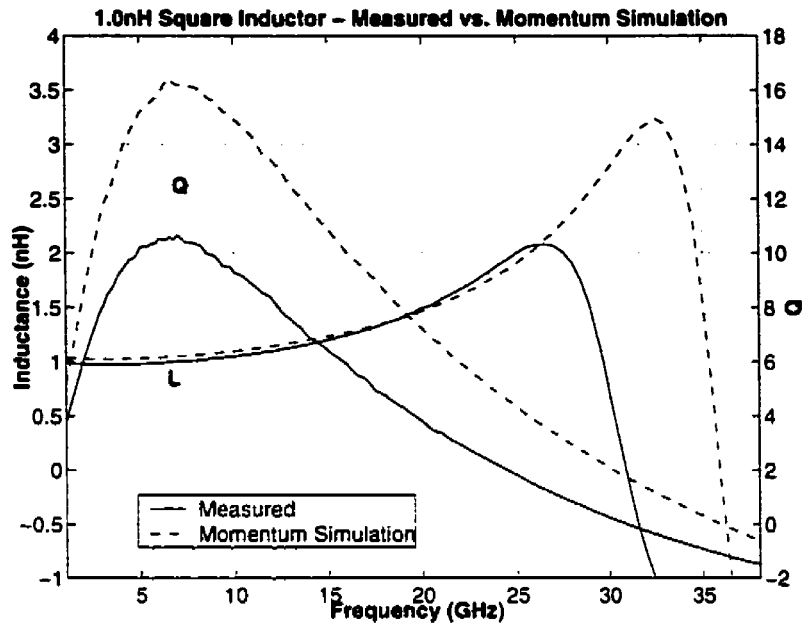


Fig. 3.18: Measured and simulated data for the 1.0nH square inductor.

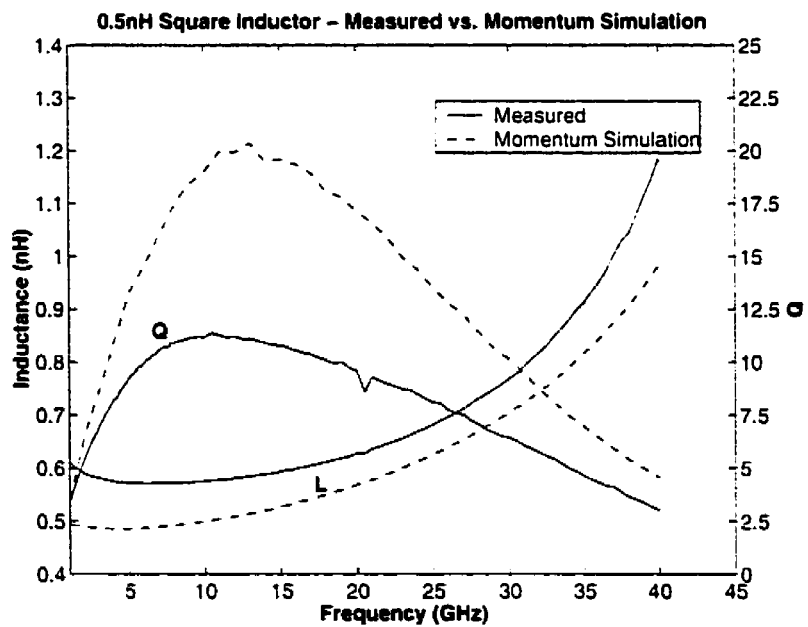


Fig. 3.19: Measured and simulated data for the 0.5nH square inductor.

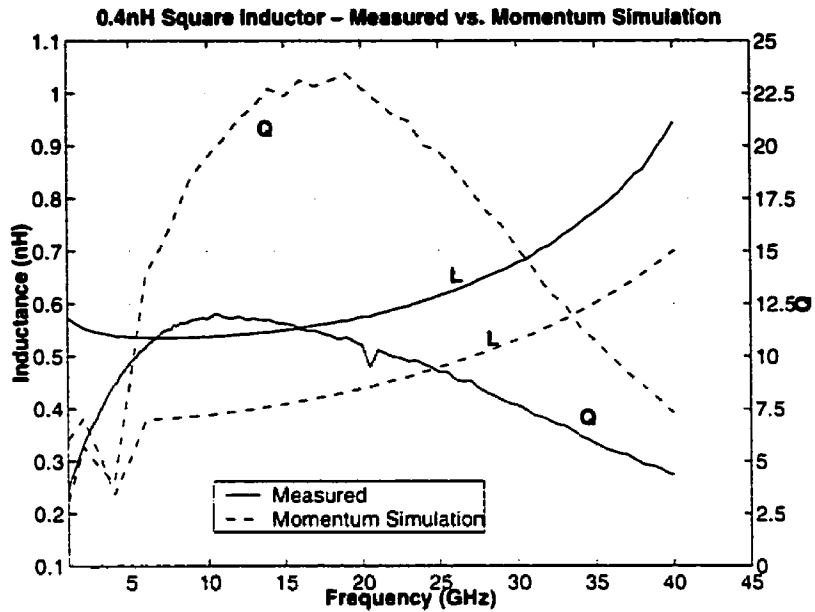


Fig. 3.20: Measured and simulated data for the 0.4nH square inductor.

3.4 Summary

This chapter discussed the measurement apparatus used to measure the fabricated on-chip spiral inductors. Measured results for all the inductors were also presented, along with analysis of the results. This chapter also compared some of the measured results with simulated results.

The following chapter discusses oscillator design theory and the design of a fully integrated oscillator that incorporates the 0.5nH octagonal trench inductor.

CHAPTER 4: Oscillator Theory and Design

A radio-frequency oscillator is a circuit that generates a periodic signal from the energy it receives through DC bias. In the transmit and receive frequency range of wireless circuits, oscillators are generally made using a negative resistance cell or gain block and a resonating structure. Since the resonator, in part, determines the spectral purity of the oscillator, a fundamental understanding of its operation is required prior to oscillator design. Consequently the basic LCR resonator will be examined first.

4.1 Parallel LCR Resonators

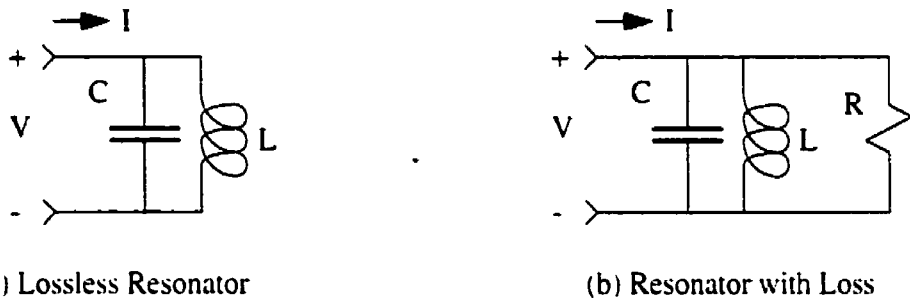


Fig. 4.1: Parallel LC resonator structures: a) lossless and b) with loss.

The ratio of input voltage to input current for the resonator in Fig. 4.1b can be found through circuit analysis.

$$I = \frac{V}{1/(sC)} + \frac{V}{sL} + \frac{V}{R} \quad (\text{EQ 4.1})$$

$$\frac{V}{I} = \left(\frac{1}{C}\right) \frac{s}{s^2 + \frac{s}{RC} + \frac{1}{LC}} \quad (\text{EQ 4.2})$$

the roots of the denominator (p_1, p_2) are

$$p_1 = -\frac{1}{2RC} + \sqrt{\frac{1}{4R^2C^2} - \frac{1}{LC}} \quad (\text{EQ 4.3})$$

$$p_2 = -\frac{1}{2RC} - \sqrt{\frac{1}{4R^2C^2} - \frac{1}{LC}} \quad (\text{EQ 4.4})$$

When the circuit is excited by a single impulse of current $I(s) = 1$, the voltage response will drop exponentially due to dissipation in the resistor. However, as the voltage drops to its steady-state value, it may oscillate depending on the values of R, C, and L.

The requirement for damped oscillation of the resonator is $\frac{1}{LC} > \frac{1}{4R^2C^2}$. Under this condition the circuit is said to be underdamped and will oscillate in an exponentially decreasing fashion. The decay constant is a function of the resonator quality factor (Q). If $Q = \infty$ the oscillator signal does not decay.

4.1.1 Resonator Quality Factor

When discussing resonators, quality factor (Q) refers to the ratio of peak stored energy to power dissipated per cycle. The general formula for Q is

$$Q = \frac{2\pi(E_{pk})}{(P_{loss}/cycle)} \quad (\text{EQ 4.5})$$

and can be used to determine the Q of the LCR circuit of Fig. 4.1b. E_{pk} is the peak energy stored in the system, and $P_{loss}/cycle$ is the power dissipated in the circuit per cycle. At resonance the inductor and capacitor alternate in storing energy over a cycle; thus the peak stored energy can be defined as being in either the inductor or the capacitor. Therefore

$$E_{pk} = \frac{1}{2} V_{pk}^2 C \quad (\text{EQ 4.6})$$

Where V_{pk} is the peak voltage across the circuit. The loss per cycle is simply the power dissipation in the resistor divided by T , the period of the oscillation.

$$P_{loss}/(cycle) = \left(\frac{V_{rms}^2}{R} \right) T \quad (\text{EQ 4.7})$$

where V_{rms} is the root mean square voltage across the circuit. Using $T = \frac{2\pi}{\omega}$ and

$V_{rms} = \frac{V_{pk}}{\sqrt{2}}$, the power loss per cycle becomes

$$P_{loss}/(cycle) = \left(\frac{V_{pk}^2}{2R} \right) \left(\frac{2\pi}{\omega} \right) \quad (\text{EQ 4.8})$$

Using (EQ 4.6) and (EQ 4.8), (EQ 4.5) reduces to

$$Q = \omega RC \quad (\text{EQ 4.9})$$

An alternative expression for Q , used later in this work, is:

$$Q = \frac{\omega}{2} \left| \frac{d\phi}{d\omega} \right| \quad (\text{EQ 4.10})$$

where $\frac{d\phi}{d\omega}$ is the rate of change of resonator impedance angle with respect to frequency.

It can be shown that analyzing the circuit in Fig. 4.1b and using (EQ 4.10) to find Q yields (EQ 4.9). (EQ 4.10) is useful when determining the Q of a resonator from measured input voltages and currents.

4.1.2 Parallel Resonator with Series Inductor Losses

The oscillator designed in this work incorporated a resonator with losses in series with the inductor as shown in Fig. 4.2. This resonator structure will be referred to as the parallel resonator with series loss or PRSL.

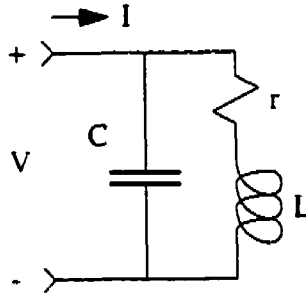


Fig. 4.2: Parallel resonator with series inductor losses.

The input impedance to this circuit can be found through circuit analysis.

$$I = \frac{V}{r + sL} + VC s \quad (\text{EQ 4.11})$$

$$\frac{V}{I} = \left(\frac{1}{r + sL} + sC \right)^{-1} \quad (\text{EQ 4.12})$$

$$\frac{V}{I} = \frac{r + sL}{s^2 + s\frac{r}{L} + \frac{1}{LC}} \quad (\text{EQ 4.13})$$

$$\frac{V}{I} = Z_m = \left(\frac{1}{C} \right) \frac{s + \frac{r}{L}}{s^2 + s\frac{r}{L} + \frac{1}{LC}} \quad (\text{EQ 4.14})$$

The input impedance given in (EQ 4.14) has a frequency response that is different from that of the parallel LCR circuit. The magnitude of the parallel LCR resonator's input impedance is highest when the input impedance's phase angle is zero. This is not the case for the PRSL, where the zero phase crossing and peak magnitude occur at the same frequency only when the series losses (r) approach zero.

If the inductor quality factor, defined as $Q_l = \frac{\omega L}{r}$, is greater than 10, the PRSL can be approximated as a parallel LCR resonator [21]. The plots in Fig. 4.3 demonstrate that as Q_l increases, the behaviour of the PRSL approaches that of the parallel LCR resonator.

In Fig. 4.3a the Q of the parallel LCR resonator and the Q_l of the PRSL are 2. The magnitude and the phase of the PRSL vary significantly from the parallel LCR circuit's magnitude and phase. Note also that the zero phase angle crossing of the PRSL does not occur at the same frequency as its peak magnitude. In Fig. 4.3b the Q and Q_l of both the resonator types are 10. The magnitude plots of the two resonator types are so similar that they are indistinguishable in Fig. 4.3b. In Fig. 4.3c the Q and Q_l of each resonator circuit are 20. Once again the magnitude curves are indistinguishable, and in this case, the phase curves are nearly coincident near their zero phase angle crossings.

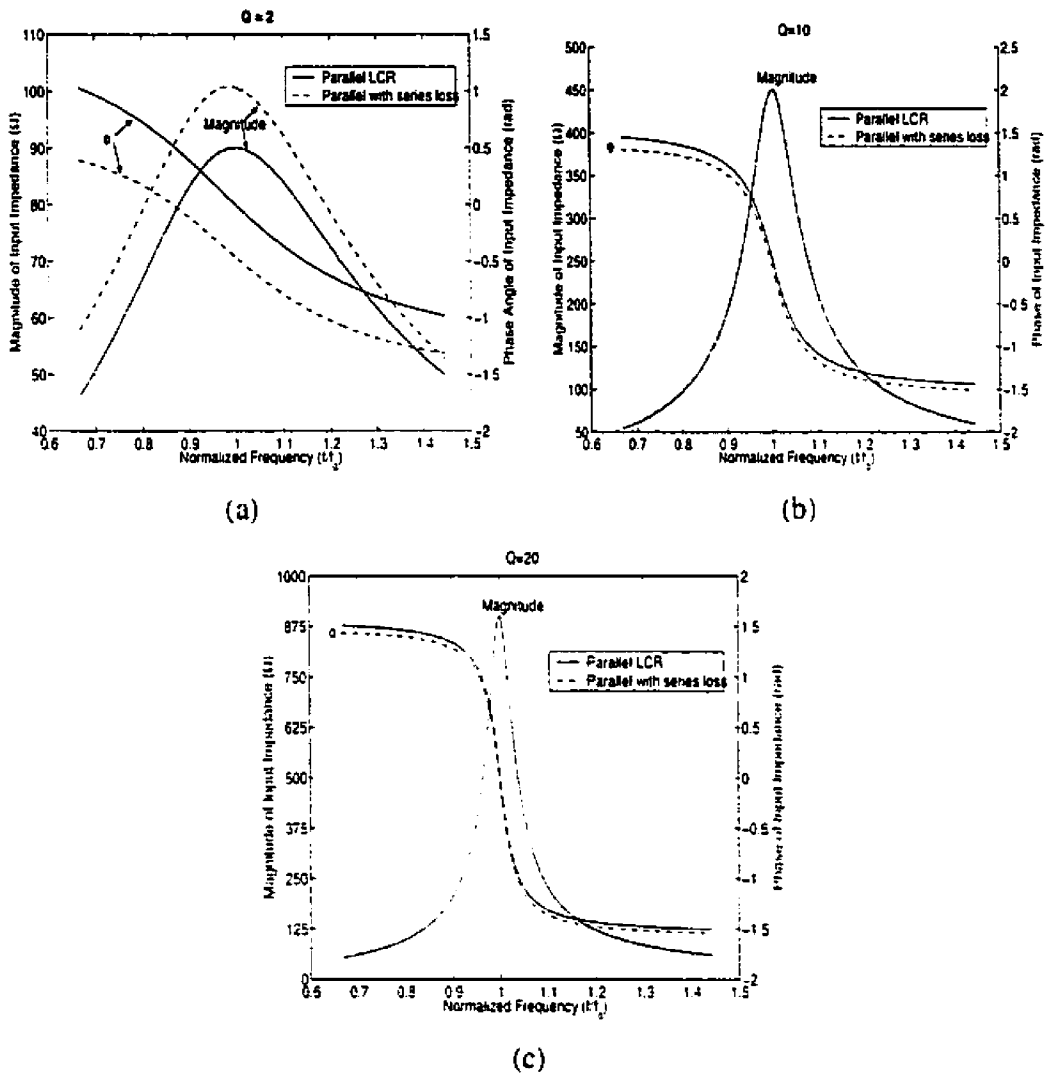


Fig. 4.3: Parallel resonator with parallel losses and parallel resonator with series losses: a) for $Q=2$, b) for $Q=10$, and c) for $Q=20$. Note the magnitude curves for the two types of resonator appear coincident in plots b and c.

4.1.3 Sustained Oscillation

In the case of the parallel LCR resonator, a sustained oscillation can occur if the resonator losses are compensated for, transforming the parallel LCR resonator into the lossless LC resonator of Fig. 4.1a. (EQ 4.3) and (EQ 4.4) would then simplify to

$$p_1 = j/\sqrt{LC} \quad (\text{EQ 4.15})$$

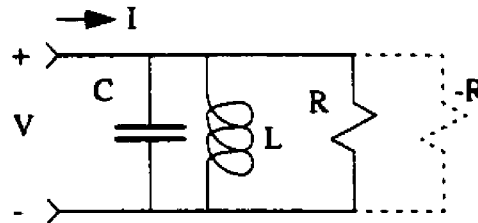
$$p_2 = -j/\sqrt{LC} \quad (\text{EQ 4.16})$$

and the circuit would oscillate at a frequency of $1/\sqrt{LC}$.

Resonator loss compensation can be achieved by adding a power source that replenishes dissipated oscillation energy in parallel with the resonator. The power source can be represented by a negative resistance as shown Fig. 4.4. With the losses compensated, the LCR resonator sustains oscillation like the lossless parallel LC resonator of Fig. 4.1a.

In practical oscillators, diodes or transistor amplifiers are used to form the replenishing power source. If the power provided to the resonator by the power source is exactly equal to the power dissipated, the oscillation signal energy will neither increase nor decrease. Since the initial oscillation energy in the resonator is typically noise, it is desirable to have the oscillation signal increase to a usable level. In the case of the parallel LCR resonator, this is done by making the magnitude of the negative resistance smaller than the resonator loss resistance. To ensure oscillation buildup is robust against variations in the parallel LCR resonator losses, the magnitude of the negative resistance is typically made smaller than the loss resistance by a factor of three [8].

The oscillation amplitude limits when the magnitude of the negative resistance created by the transistor or diode circuit increases, through large signal effects such as cut-off or saturation, to the value of the resonator resistance.



Resonator with Loss Cancelled

Fig. 4.4: LC resonator with losses cancelled by -R.

4.2 Phase Noise

One of the most critical characteristics of an oscillator, with respect to the radio system, is its phase noise level. Phase noise refers to the random phase fluctuations present in the output signal of all oscillators. Phase noise degrades the signal to noise ratio of communication systems and therefore places a limit on the system performance. Consequently, phase noise is specified at the system level and is hence a design requirement for the oscillator.

In spite of its importance to system performance, predicting phase noise continues to prove difficult. A number of different phase noise calculation methods have been published with various claims of success. The most widely known and cited phase noise equation is based on work by Leeson [13], and was used in this research to predict phase

noise. Leeson's equation centers around the noise filtering capabilities of the resonator circuit, and the noise generated by losses in the resonator and by the negative resistance element (Fig. 4.4). Section 4.3 will discuss how an amplifier with positive feedback is used to create the negative resistance element.

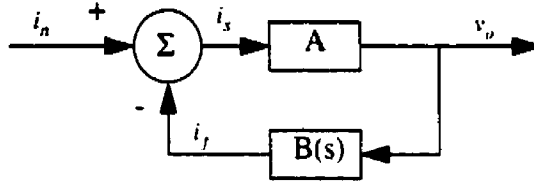


Fig. 4.5: Oscillator feedback loop for phase noise model derivation.

Fig. 4.5 shows a basic feedback loop used for phase noise model derivation. In the loop, $B(s)$ is considered a resonator circuit admittance, converting the output voltage (v_o) to a current (i_f). The factor A is considered a transimpedance amplifier response, converting i_s to the output voltage. The transfer function of the loop can be found as follows.

$$i_s = i_n - i_f \quad (\text{EQ 4.17})$$

$$v_o = Ai_s \quad (\text{EQ 4.18})$$

$$i_f = B(s)v_o \quad (\text{EQ 4.19})$$

Substituting (EQ 4.18) and (EQ 4.19) into (EQ 4.17) gives:

$$\frac{v_o}{A} = i_n - B(s)v_o \quad (\text{EQ 4.20})$$

$$\frac{v_o}{i_n} = \frac{A}{1 + AB(s)} \quad (\text{EQ 4.21})$$

When the oscillation condition is satisfied in steady state (the signal is no longer growing), the denominator of (EQ 4.21) must equal zero. Therefore $AB(s) = -1$ at the resonant frequency of the circuit. For the purposes of this discussion, the amplifier (or negative resistance element) is considered to be ideal and therefore A is a constant with respect to frequency. $B(s)$ does vary with frequency, and can be approximated around the resonant frequency (ω_0) using a Taylor series [14] where $\Delta\omega$ represents a small change in frequency from ω_0 :

$$B(j\omega) = B(\omega_0) + \Delta\omega \frac{dB}{d\omega} \quad (\text{EQ 4.22})$$

and (EQ 4.21) becomes

$$\frac{v_o}{i_u} = \frac{A}{1 + A \left(B(\omega_0) + \Delta\omega \frac{dB}{d\omega} \right)} \quad (\text{EQ 4.23})$$

Recalling that $AB(j\omega_0) = -1$, (EQ 4.23) simplifies to

$$\frac{v_o}{i_u} = \frac{A}{\left(\Delta\omega A \frac{dB}{d\omega} \right)} \quad (\text{EQ 4.24})$$

Since $AB(j\omega)$ has an amplitude and a phase component and A is a constant, $AB(j\omega)$ can be decomposed to $AB(j\omega) = |A||B(j\omega)|e^{j\phi}$ and $A \frac{dB}{d\omega}$ can be written

$$A \frac{dB}{d\omega} = |A| \frac{d|B|}{d\omega} e^{j\phi} + |A||B| j e^{j\phi} \left| \frac{d\phi}{d\omega} \right| \quad (\text{EQ 4.25})$$

The right hand side of (EQ 4.25) is composed of two orthogonal terms; so the magnitude of $A \frac{dB}{d\omega}$ becomes

$$|A| \left| \frac{dB}{d\omega} \right| = \sqrt{|A|^2 \left| \frac{dB}{d\omega} \right|^2 + |A|^2 |B|^2 \left| \frac{d\phi}{d\omega} \right|^2} \quad (\text{EQ 4.26})$$

As shown in Fig. 4.6 the magnitude of B (the resonator admittance) changes slowly near ω_r , where as its phase changes rapidly; thus the $|A|^2 \left| \frac{dB}{d\omega} \right|^2$ term in (EQ 4.26) can be ignored.

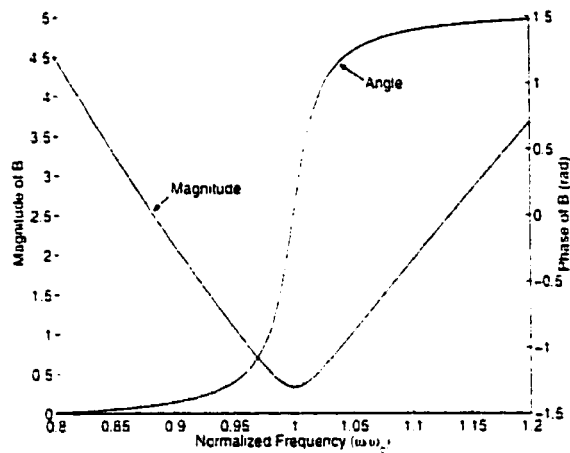


Fig. 4.6: Magnitude and phase response of an LCR resonator with a Q of 30.

Because $|AB| = 1$ at ω_r , $|A|^2 |B|^2 = 1$ at small frequency offsets from ω_r . Therefore.

$|A| \left| \frac{dB}{d\omega} \right|$ reduces to

$$|A| \left| \frac{dB}{d\omega} \right| = \left| \frac{d\phi}{d\omega} \right| \quad (\text{EQ 4.27})$$

Substituting back into (EQ 4.24),

$$\frac{v_o}{i_n} = \frac{A}{\left(\Delta\omega \left| \frac{d\phi}{d\omega} \right| \right)} \quad (\text{EQ 4.28})$$

Using a rearranged form of (EQ 4.10), $\left| \frac{d\phi}{d\omega} \right| = \frac{2Q}{\omega_o}$, (EQ 4.28) becomes

$$\frac{v_o}{i_n} = \frac{A\omega_o}{(2Q\Delta\omega)} \quad (\text{EQ 4.29})$$

The input signal (i_n) in this analysis is the noise current due to resonator losses. The output signal (v_o) is the voltage across the resonator and is found by multiplying the mean

squared noise current per hertz by the transfer function in (EQ 4.29) squared: $v_o^2 = \left| \frac{v_o}{i_n} \right|^2 i_n^2$.

The noise current i_n is defined as

$$i_n^2 = \frac{4kT}{R} \quad (\text{EQ 4.30})$$

and has units of $\frac{\text{Amperes}^2}{\text{Hz}}$, where k is Boltzmann's constant, T is the temperature of the

resonator in Kelvins. R is the resistance looking into the resonator at ω_o . v_o^2 therefore becomes

$$v_o^2 = \frac{A^2\omega_o^2}{4Q^2\Delta\omega^2} \left(\frac{4kT}{R} \right) \quad (\text{EQ 4.31})$$

This noise signal accounts for both amplitude noise and phase noise. The noise energy is assumed to divide equally between these two types of noise. Since oscillators usually operate with active devices either cut-off or in saturation for part of the cycle, amplitude noise at the output of the oscillator is usually significantly suppressed relative to the phase

noise portion, and phase noise is therefore usually considered the dominant form of noise in an oscillator. The phase portion of the noise, v_{pn}^2 , is therefore $\frac{v_n^2}{2}$.

$$v_{pn}^2 = \frac{A^2 \omega_n^2}{4Q^2 \Delta\omega^2} \left(\frac{2kT}{R} \right) \quad (\text{EQ 4.32})$$

Recall A is simply the negative resistance which at steady state oscillation exactly cancels the tank losses R . Therefore $A^2 = R^2$ and (EQ 4.32) becomes

$$v_{pn}^2 = \frac{\omega_n^2}{4Q^2 \Delta\omega^2} (2kTR) \quad (\text{EQ 4.33})$$

Phase noise is usually given as mean square noise voltage relative to the mean square signal voltage so (EQ 4.33) becomes

$$\frac{v_{pn}^2}{v_{sig}^2} = \frac{\omega_n^2}{4Q^2 \Delta\omega^2} \left(\frac{2kTR}{v_{sig}^2} \right) \quad (\text{EQ 4.34})$$

(EQ 4.34) is the double sideband noise power. Phase noise is typically given as the single sideband noise power which is obtained by dividing (EQ 4.34) by two.

$$\frac{v_{pn}^2}{v_{sig}^2} = \frac{\omega_n^2}{8Q^2 \Delta\omega^2} \left(\frac{2kTR}{v_{sig}^2} \right) \quad (\text{EQ 4.35})$$

To cleanup the left hand side of (EQ 4.35), the equation $PN = \frac{v_{pn}^2}{v_{sig}^2}$ is used, where PN

denotes phase noise. Also, using the relation for output signal power, $P_{sig} = \frac{v_{sig}^2}{R}$,

(EQ 4.35) is rewritten as:

$$PN = \frac{\omega_o^2}{8Q^2\Delta\omega^2} \left(\frac{2kT}{P_{sig}} \right) \quad (\text{EQ 4.36})$$

This equation only accounts for the noise produced by losses in the resonator. It does not account for noise from the unstable amplifier providing the negative resistance. To account for amplifier noise, a factor F , which is often taken to be the noise factor of the amplifier, is inserted in (EQ 4.36) to produce equation (EQ 4.37). The noise factor of an amplifier is defined as [15] the total output amplifier output noise power divided by the output noise power due to the input source. The noise factor of an amplifier is derived under small signal conditions and is dependent on the impedances at the input and output of the amplifier.

$$PN = \frac{\omega_o^2}{8Q^2\Delta\omega^2} \left(\frac{2FkT}{P_{sig}} \right) \quad (\text{EQ 4.37})$$

(EQ 4.37) is a simplified version of Leeson's equation that shows the importance of high resonator Q factor for reducing phase noise. In this derivation the negative resistance element was assumed to be ideal, however, in reality it will load the resonator as well as provide energy. Q in (EQ 4.37) must therefore be the resonator Q with the loading of the amplifier and any other external loading (some oscillators draw their output directly from the resonator). The Q of the loaded resonator is known as the loaded Q , and the unloaded resonator Q is called the unloaded Q .

-R cell flicker noise contributions to phase noise can be included by modifying (EQ 4.37) to:

$$\frac{v_{pn}^2}{v_{sig}^2} = \frac{\omega_o^2}{4Q^2\Delta\omega^2} \left(\frac{2FkT}{P_{sig}} \right) \left(1 + \frac{\omega_c}{\Delta\omega} \right) \quad (\text{EQ 4.38})$$

where ω_c is the flicker noise corner frequency of the negative resistance device. Flicker noise in electronic devices is usually attributed to the random trapping and releasing of charges by impurities in the semiconductor material. Flicker noise power decreases as frequency increases demonstrating a $1/f$ characteristic. The flicker noise corner frequency of a device is the frequency at which the flicker noise power of the device is equal to the white noise power (i.e. thermal noise) of the device.

Flicker noise contributions were not considered in this work due to the lack of a reliable ω_c value for the bipolar process used in the design of the oscillator. Thus phase noise estimations made in Section 4.5.5 used (EQ 4.37).

4.3 Generation of Negative Resistance

Generally an amplifier containing a positive feedback loop is used to generate the required negative resistance. This type of amplifier configuration is often called a -R cell. In the case of microwave oscillators this amplifier can be as simple as a single transistor or even a Gunn diode. Rather than appearing purely resistive -R cells usually add some capacitance to the circuit that needs to be accounted for in the design of an oscillator (Fig. 4.7).

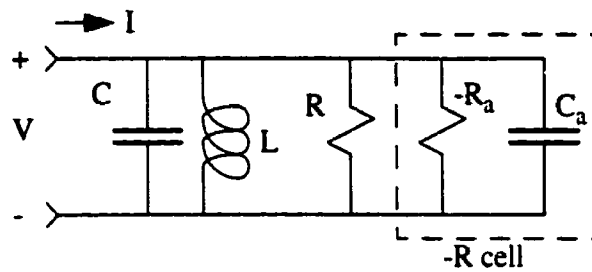


Fig. 4.7: Small-signal circuit of LCR resonator with unstable amplifier.

If R_a is made equal to R then the circuit will oscillate with an amplitude that neither decreases nor increases. In practical oscillators however R_a is made smaller to guarantee cancellation of resonator losses and to permit the oscillation signal to grow. Signal amplitude will increase until large signal effects such as saturation or cutoff increase the magnitude of R_a to the point that $|-R_a| = |R|$.

4.3.1 The Cross-coupled Differential Pair

One type of -R cell is the cross-coupled differential pair. Shown in Fig. 4.8, this circuit has been used at microwave frequencies on silicon [9].

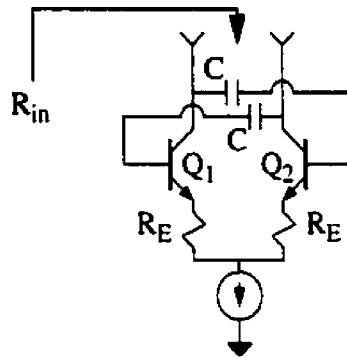


Fig. 4.8: Cross-coupled differential pair circuit (biasing not shown).

Using the small signal T model [7] and assuming the capacitors in Fig. 4.8 are large enough to ignore, it is possible to find an expression for the input impedance of the cross-coupled pair.

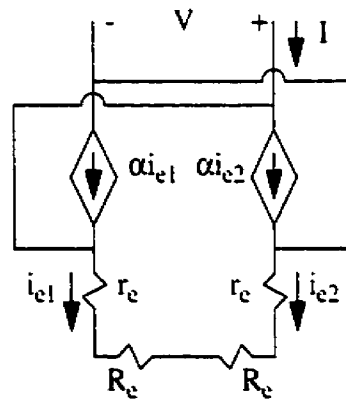


Fig. 4.9: Small signal model of cross-coupled pair.

$$V = i_{e1}(r_e + R_E) - i_{e2}(r_e + R_E) \quad (\text{EQ 4.39})$$

since $i_{e1} = -i_{e2}$,

$$V = 2i_{e1}(r_e + R_E) \quad (\text{EQ 4.40})$$

Examining the current flow in the circuit we find:

$$I = \alpha i_{e2} + (i_{e1} - \alpha i_{e1}) \quad (\text{EQ 4.41})$$

where α is the common base current gain and is defined as $\alpha = \frac{\beta}{\beta + 1}$.

Once again using $i_{e1} = -i_{e2}$,

$$I = i_{e1} - 2\alpha i_{e1} \quad (\text{EQ 4.42})$$

Dividing (EQ 4.40) by (EQ 4.42) gives:

$$\frac{V}{I} = \frac{2i_{e1}(r_e + R_E)}{i_{e1} - 2\alpha i_{e1}} \quad (\text{EQ 4.43})$$

if we assume $\alpha = 1$, then

$$\frac{V}{I} = (-2)(r_e + R_E) \quad (\text{EQ 4.44})$$

Thus the impedance looking into the cross-coupled pair is negative as shown in (EQ 4.44). For simplicity this analysis ignored parasitics in the bipolar junction transistors (BJT).

4.3.2 The Cross-coupled Differential Pair with Emitter-Follower Buffers

A useful modification to the cross-coupled differential pair can be made by adding emitter-followers to the feedback path as shown in Fig. 4.10. The addition of the emitter-follower transistors Q_3 and Q_4 buffers the resonator from the differential pair input impedance (increasing the loaded resonator Q) and provides a frequency tuning method which is discussed in Section 4.4.

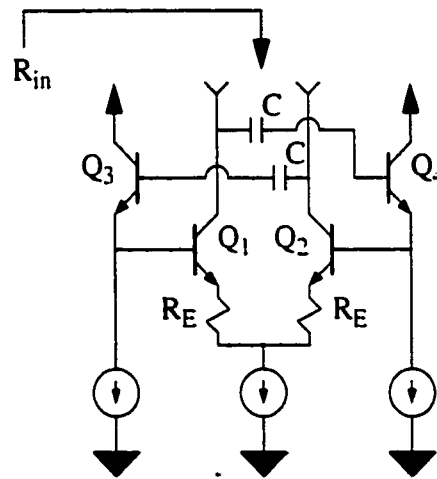


Fig. 4.10: Cross-coupled Differential Pair with Emitter-Follower Buffers (biasing not shown).

Small signal analysis of this circuit (ignoring transistor parasitics) shows that its terminal impedance is similar to that of the plain cross-coupled differential pair. The small signal equivalent circuit is shown in Fig. 4.11.

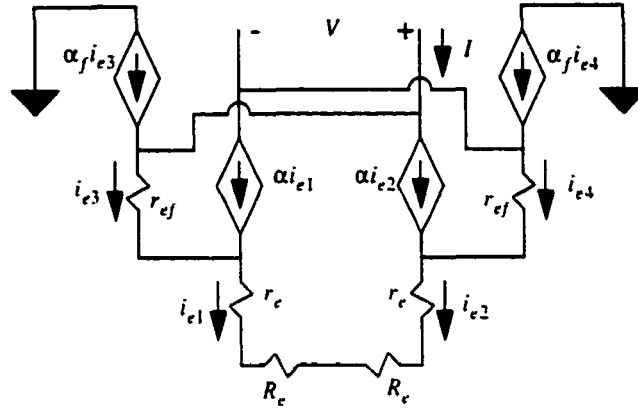


Fig. 4.11: Small Signal equivalent circuit of cross coupled pair with emitter-followers.

$$V = i_{e3}r_{ef} + i_{e1}(r_e + R_E) - i_{e2}(r_e + R_E) - i_{e4}r_{ef} \quad (\text{EQ 4.45})$$

Due to the mirrored nature of the circuit

$$i_{e2} = -i_{e1} \quad \text{and} \quad (\text{EQ 4.46})$$

$$i_{e4} = -i_{e3} \quad (\text{EQ 4.47})$$

Reducing (EQ 4.45) using (EQ 4.46) and (EQ 4.47) gives:

$$V = 2i_{e3}r_{ef} + 2i_{e1}(r_e + R_E) \quad (\text{EQ 4.48})$$

i_{e3} is related to i_{e1} by

$$i_{e3} = i_{e1} - \alpha i_{e1} \quad (\text{EQ 4.49})$$

V finally reduces to

$$V = 2i_{e1}[r_{ef}(1 - \alpha) + r_e + R_E] \quad (\text{EQ 4.50})$$

Similarly an expression for I can be found:

$$I = \alpha i_{e2} + i_{e3} - \alpha_f i_{e3} \quad (\text{EQ 4.51})$$

Using (EQ 4.46) and (EQ 4.49) the expression for I becomes

$$I = -\alpha i_{e1} + (i_{e1} - \alpha i_{e1})(1 - \alpha_f) \quad (\text{EQ 4.52})$$

$$I = i_{e1}(1 - \alpha - \alpha_f - \alpha + \alpha\alpha_f) \quad (\text{EQ 4.53})$$

The expression for the small signal input impedance to the cross coupled differential pair with emitter-followers is

$$\frac{V}{I} = \frac{2i_{e1}[r_{ef}(1 - \alpha) + r_e + R_E]}{i_{e1}(1 - \alpha - \alpha_f - \alpha + \alpha\alpha_f)} = \frac{2[r_{ef}(1 - \alpha) + r_e + R_E]}{(1 - 2\alpha - \alpha_f + \alpha\alpha_f)} \quad (\text{EQ 4.54})$$

If we assume for simplicity that all the transistors have a current gain $\beta > 100$, then $\alpha = 1$, $\alpha_f = 1$ and (EQ 4.54) reduces to

$$\frac{V}{I} = -2(r_e + R_E) \quad (\text{EQ 4.55})$$

The above analysis shows that placing the emitter-followers in the feedback path of the cross coupled pair, ideally, has little effect on the negative resistance generated.

The circuits of Fig. 4.8 and Fig. 4.10 present a negative resistance at their terminals, which indicates -R cells provide energy to the resonator. However, this is not the whole story; the resonator must supply energy to the -R cell in order to get more back (the -R cell is an amplifier that requires some stimulus). This energy lost by the resonator is a form of resistive loading that decreases the resonator's loaded Q.

Placing emitter-followers in the feedback path reduces the resistive loading of the -R cell on the resonator. The emitter-followers buffer the resonator from the differential pair

impedance. Appendix A shows the derivation of the input and output impedance of the emitter-follower. The input impedance is

$$z_{in} = r_{\pi} + (1 + \beta)R_L \quad (\text{EQ 4.56})$$

where R_L is the impedance of the differential pair transistor that is connected to the emitter of the emitter-follower. The loading on the resonator is reduced by a factor of $(1 + \beta)$, increasing the loaded Q.

Another advantage of the emitter-follower buffers is their use in tuning oscillation frequency as described in the next section.

4.4 Frequency Tuning

Fully integrated oscillators often control the oscillation frequency via a reverse biased diode which provides a voltage controlled capacitance. With the emitter-follower buffered differential pair shown in Fig. 4.10, oscillation frequency can be controlled by varying the bias current in the emitter-follower buffers or in the differential pair. Each transistor connected to the resonator loads the resonator by adding some amount of parasitic resistance and reactance. The parasitic reactance reduces the oscillation frequency of the resonator. Oscillation frequency can be controlled by varying the degree of transistor parasitics presented to the resonator.

4.4.1 Emitter-Follower Current Controlled Frequency Tuning

As shown in Fig. 4.10, the bases of the emitter-follower buffers are capacitively coupled to the resonator. The base of an emitter-follower has several parasitic capacitances as shown in the small signal model in Fig. 4.12.

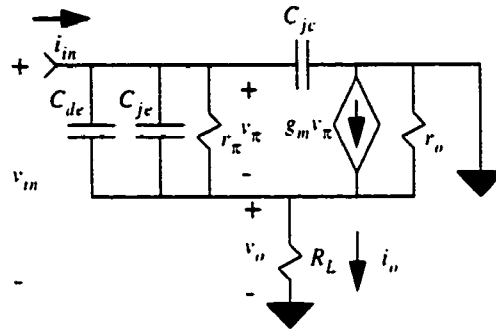


Fig. 4.12: Emitter-follower small signal model with parasitic capacitances.

C_{je} is the base-emitter junction capacitance and C_{jc} is the base-collector junction capacitance. Both of these parasitic capacitances result from the charge differentials in the transition region of their respective junctions and are therefore dependent on the voltage across the junctions. C_{de} is the base-emitter diffusion capacitance (often called the charge storage capacitance) which is created by the presence of minority charge carriers when the junction is forward biased. The base-collector junction does not have a parasitic diffusion capacitance because it is reverse biased under normal (active region) operation of the BJT. Under forward bias conducting conditions the diffusion capacitance dominates as the depletion region disappears, eliminating the junction capacitance. Diffusion capacitance is directly proportional to bias current and can be calculated using [16]

$$C_{de} = \frac{q}{kT} \tau_p I_{bDC} \quad (\text{EQ 4.57})$$

where q is the magnitude of the charge on an electron, k is Boltzmann's constant ($1.38 \times 10^{-23} \frac{J}{K}$), T is the temperature in Kelvins, τ_p is the average lifetime of a minority charge carrier, and I_{bDC} is the DC base current. (EQ 4.57) shows that the bias current can be used to control the base-emitter capacitance, which is part of the resonator's effective capacitance.

It should be noted that the outcome of this effect is complicated by C_{de} 's role in determining the current gain of the transistor. Because the oscillator is designed for 14.5GHz and the f_T of the transistors used is 37GHz, the transistor's current gain is rolling off with frequency and is determined from [19]

$$\beta(j\omega) = \frac{\beta_0}{1 + j\omega r_\pi (C_\pi + C_u)} \quad (\text{EQ 4.58})$$

where β_0 is the low frequency current gain, and $C_\pi = C_{de} + C_{je}$. The input impedance of the emitter-follower is dependent on the base impedance of the emitter-follower transistor (z_{be}), on the emitter impedance (z_E), and on the current gain ($\beta(j\omega)$).

$$z_{in} = z_{be} + (1 + \beta(j\omega))z_E \quad (\text{EQ 4.59})$$

Therefore, C_{de} not only affects z_{be} in a direct fashion, but also indirectly affects (through the current gain) how an emitter impedance appears at the base.

4.4.2 Differential Pair Bias Current Controlled Frequency Tuning

The differential pair loads the resonator in two ways. The first is the impedance presented to the resonator by the collector of the differential pair transistors. This impedance changes little with bias current. The second way the differential pair loads the tank is indirectly through the emitter-followers. The bases of the differential pair transistors load the emitter nodes of the emitter-followers as shown in Fig. 4.13.

To simplify the analysis of the circuit in Fig. 4.13, no emitter degeneration is assumed on the differential pair transistor. The base-collector capacitance of the differential pair transistor has been broken into two capacitors using Miller's Theorem: C_c , and a base to ground capacitance that is absorbed in $z_{\pi 2}$. C_{μ} is the emitter-follower base to collector capacitance and is left out of the input impedance calculation (EQ 4.60) for simplicity.

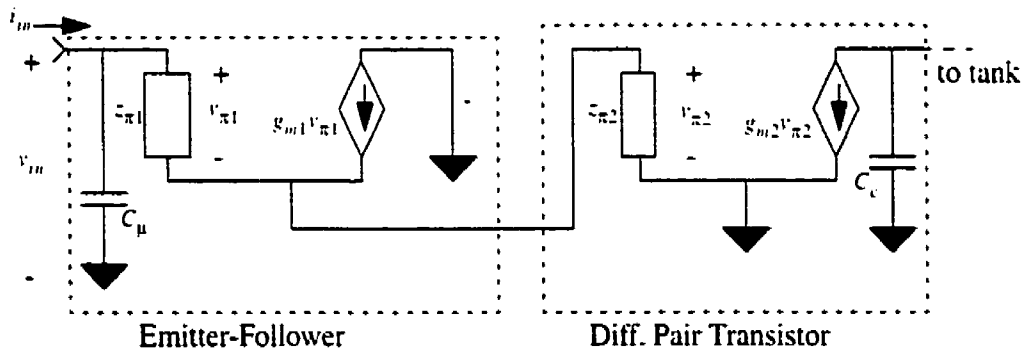


Fig. 4.13: Small signal model of emitter-follower with differential pair transistor as load.

The input impedance of the emitter-follower with a differential pair transistor load is given by

$$z_{in} = z_{\pi 1} + (1 + \beta_1(j\omega))z_{\pi 2} \quad (\text{EQ 4.60})$$

Differential pair bias current tuning uses the same principle as the emitter-follower bias current tuning: control of the diffusion capacitance C_{de} which affects $z_{\pi 2}$ in (EQ 4.60). The relationship between changes in differential pair transistor C_{de} and the oscillation frequency is complicated by the current gain of the emitter-follower transistors as shown in (EQ 4.60).

It is important to note that this analysis was done in the small signal regime assuming all the transistors were operating in the active mode. Changes in bias current can cause some transistors to operate in the saturation region for part of the oscillation cycle, complicating the analysis.

4.5 Design of Bias Current Tuned Oscillator

As mentioned in Chapter 1, the oscillator designed in this work was to use bias current to tune the oscillation frequency, and to target the specifications in Table 4.1.

Parameter	Target Value
Frequency	14 - 15 GHz
Phase Noise	-119 dBc/Hz @ 1MHz offset
	-99 dBc/Hz @ 100kHz offset
	-79 dBc/Hz @ 10kHz offset
	-59dBc/Hz @ 1kHz offset

Table 4.1: Target specifications for bias tuned oscillator.

This section describes the key design choices that were made in the design of the bias current tuned oscillator presented in this document. With the exception of the inductor

analysis, all simulations on the oscillator circuit were performed using SpectreRF version 4.4.2.1. Simulations were performed without considerations of transmission line effects due to the lack of reliable models.

Due to process availability issues, the bias current tuned oscillator was designed for fabrication in the NT35 process defined in [17]. All the substrate and metallization properties, as well as the minimum allowable spacings of this process were consistent with the NT55 process used to fabricate the spiral inductors discussed in Chapters 2 and 3. Inductor performance in the NT35 process was therefore assumed to be identical to inductor performance found using the NT55 process.

4.5.1 Selection of Inductor

The design of this oscillator took place before measured results were available on the inductors presented in Chapter 2. Preliminary simulation work on the square spirals indicated that the 0.5nH and 0.4nH inductors were the only inductors that had self resonant frequencies high enough for use in a 14.5GHz circuit. It was assumed that an octagonal inductor configuration with substrate trenches would provide a higher Q than the simulated square spirals. The 0.5nH octagonal trench inductor was therefore selected for use in the resonator portion of the oscillator.

A Q of 20 and an exact inductance of 0.5nH were assumed for the inductor used. This did not provide enough information to derive all the component values of the spiral inductor model presented in Section 2.1. Using the above mentioned assumptions, a very sim-

ple inductor model was created (Fig. 4.14), where $L = 0.5nH$ and R was found by using the equation for inductor Q :

$$Q_l = \frac{\omega L}{R} \quad (\text{EQ 4.61})$$

$$R = \frac{\omega L}{Q_l} = \frac{2\pi(14.5 \times 10^9 \text{ Hz})(0.5 \times 10^{-9} \text{ H})}{20} = 2.3 \Omega \quad (\text{EQ 4.62})$$

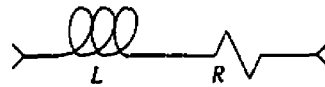


Fig. 4.14: Simple model of spiral inductor

The capacitance needed in parallel with this inductor to cause resonance at 14.5GHz was determined as follows:

$$\omega_r^2 = \frac{1}{LC} \quad (\text{EQ 4.63})$$

$$C = \frac{1}{\omega_r^2 L} = 241 \text{ fF} \quad (\text{EQ 4.64})$$

This initial value of capacitance included parasitic capacitance from the transistors.

4.5.2 Selection of Transistor Size

Because of the very low value of total resonator capacitance, the transistors had to be selected such that their parasitic capacitances did not exceed the required 241fF. The differential pair transistors (Q1 and Q2 in Fig. 4.15) were chosen to have a single $5\mu\text{m}$ long

emitter (the process used offered $0.35\mu\text{m}$ wide emitters). The selected emitter-follower transistors (Q3 and Q4) had emitter lengths of $2.5\mu\text{m}$.

The DC bias currents were set to maximize the f_T of each transistor. Emitter currents for Q1 and Q2 were set to 1.6mA , and emitter currents for Q3 and Q4 were set to 0.7mA .

Fig. D.1 of Appendix D shows a complete schematic of the oscillator circuit.

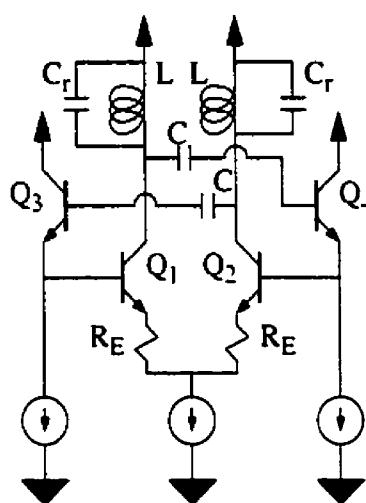


Fig. 4.15: Bias current controlled oscillator.

4.5.3 Oscillator Simulation Results

Fig. 4.16a shows the resonator signal (the voltage at the collector of Q1 minus the voltage at the collector of Q2) during oscillator startup. Fig. 4.16b shows the steady state resonator signal spectrum with the oscillator tuned for 14.9GHz . The resonator signal shows no second harmonic component and a third harmonic amplitude level of 0.015V (compared to the 0.309V amplitude of the fundamental). Suppression of the second harmonic is a result of the balanced differential nature of the circuit. The actual fabricated circuit

was not expected to provide perfect second harmonic suppression because of anticipated inherent process mismatches in the circuit components.

The accuracy of the simulated third harmonic amplitude was highly questionable, due to the narrow band nature of the spiral inductor model used in the simulation. The model (shown in Fig. 4.14) did not account for spiral inductor characteristics such as self resonance and the frequency dependence of losses. In reality the spiral inductor would behave very differently than the model at the third harmonic frequency of 44.8GHz.

4.5.4 Output Buffer

The oscillator had to drive the 50Ω input impedance of the measurement equipment used to characterize the oscillator. This was realized through the use of a differential cascode output buffer stage (Fig. 4.17). R_c is the collector resistance of the common base stage and was set to 50Ω to maximize the power to the 50Ω load (R_L). C_B is a DC blocking capacitor that was part of the measurement setup.

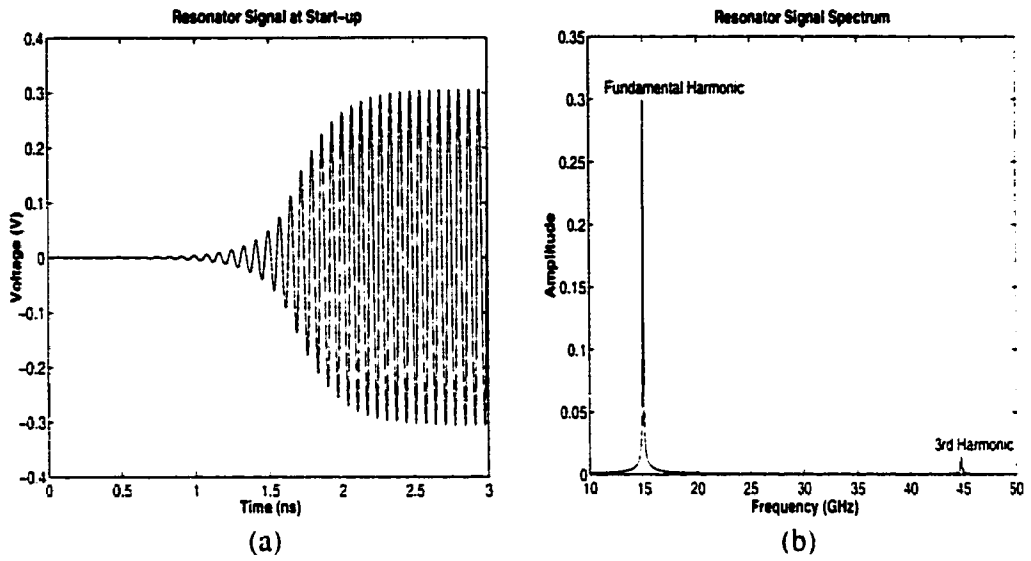


Fig. 4.16: Simulated results for (a) the oscillator resonator signal buildup during startup, and (b) the steady state resonator signal spectrum.

An output power of 0dBm was targeted since that was the minimum acceptable input power to the phase noise test set. Component values were calculated as follows:

$$V_{L_{rms}}^2 = P_{out}(2R_L) = (0.001W)(100\Omega) = 0.1V^2 \quad (\text{EQ 4.65})$$

$$V_{L_{rms}} = 0.316V \quad (\text{EQ 4.66})$$

$$V_{L_{pk}} = 0.447V \quad (\text{EQ 4.67})$$

This voltage was required across the load and the collector resistors, therefore the peak collector current in Q3 and Q4 was set to:

$$I_{L_{pk}} = \frac{V_{L_{pk}}}{2(R_L \parallel R_C)} = \frac{0.447V}{50\Omega} = 8.94mA \quad (\text{EQ 4.68})$$

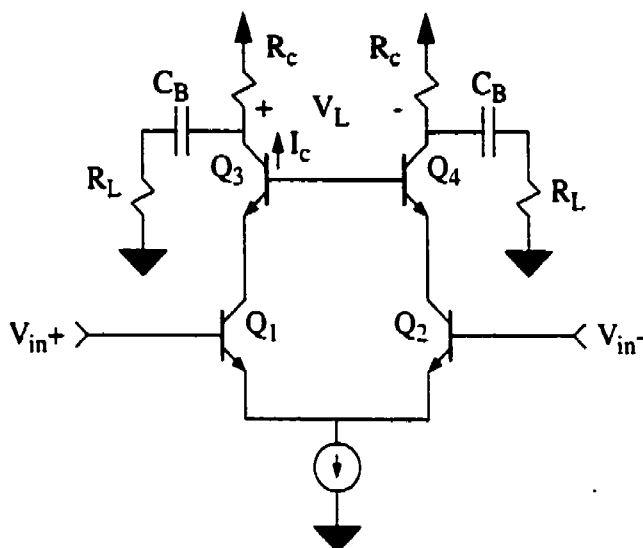


Fig. 4.17: Cascode output buffer stage.

Simulation revealed the amplifier's gain compression was not permitting the input signal to fully swing the output voltage. The amplifier's bias current was therefore boosted to 15mA, which permitted the amplifier to satisfy the output signal swing requirement. Transistors Q1, Q2, Q3, and Q4 were sized to provide the highest f_T at the assigned bias current. Using reference [17] devices with two 20 μm long emitters were selected.

The output of the oscillator, ideally, would have been the emitter node of the emitter-followers. However, placing a highly capacitive load (the bases of the input differential pair of the output buffer) at the emitters destabilized the emitter-followers. Instead the output was taken directly from the resonator at the differential pair collector node (Fig. 4.18). This connection had the disadvantage of directly loading the resonator, which

increased the resonator capacitance and increased the oscillator phase noise by reducing the resonator's loaded Q .

Simulations revealed the capacitance presented by Q5 and Q6 were too large to be compensated for by reducing C_p , causing the oscillator to oscillate well below 14.5GHz. Simulations also revealed the resonator signal voltage dropped, as a result of the connection, to the point that its voltage swing was no longer sufficient to drive the output buffer.

Another buffer stage (called the pre-driver) was therefore placed between the oscillator and the output buffer. The pre-driver had the same topology as the output buffer, but used smaller devices with emitter lengths of $10\mu\text{m}$, and a bias current of approximately 3.5mA in each transistor. The collector resistors in the pre-driver were set to 125Ω which provided an acceptable output impedance as seen by the input to the output buffer.

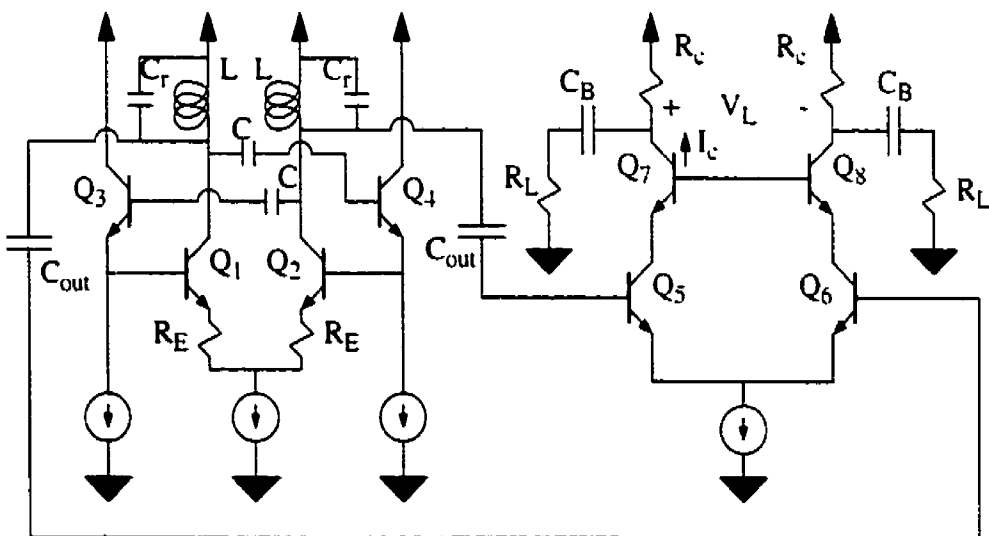


Fig. 4.18: Oscillator connected to output buffer.

The final circuit topology is shown in Fig. 4.19. A full schematic of the final circuit is provided in Appendix D, along with all component values.

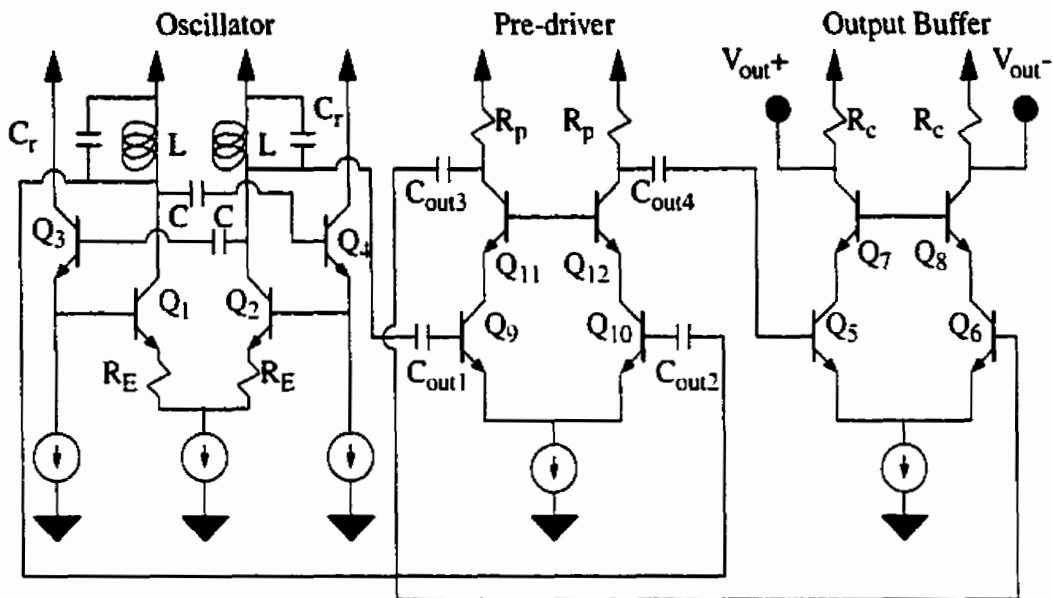


Fig. 4.19: Oscillator with initial and output buffers.

4.5.5 Phase Noise Calculation

Estimation of the oscillator's phase noise performance was done using (EQ 4.37).

repeated here for convenience:
$$PN = \frac{\omega_n^2}{8Q^2\Delta\omega^2} \left(\frac{2FKT}{P_{sig}} \right)$$

The parameter values for (EQ 4.37) were found through simulation. P_{sig} , the power in the resonator signal, was not found directly. It is related to V_{sig} by the equation

$$P_{sig} = \frac{V_{sig}^2}{Re\{z_{resonator}\}} \quad (\text{EQ 4.69})$$

V_{sig} was found to be $0.6V_{pk-pk}$ (or $0.212V_{rms}$) from large signal transient simulation.

To determine the loaded Q , the resonator was separated from the rest of the oscillator and then loaded with the resistance needed to drive the -R cell, and the capacitance provided by the -R cell. To find the capacitive loading (C_{CL}) of the -R cell, the input capacitance of the circuit in Fig. 4.20 was determined through linear AC small signal simulation. C_{CL} was found to be 133fF.

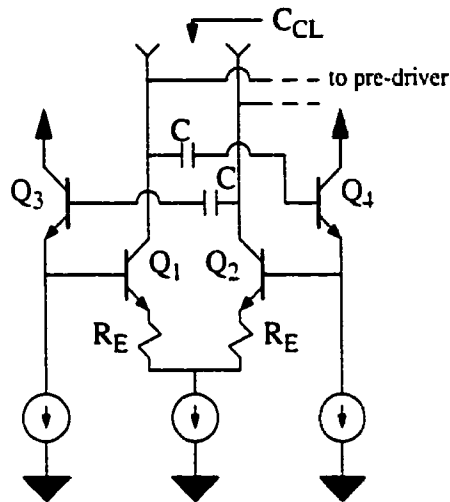


Fig. 4.20: -R cell circuit used to determine C_{CL} .

The determination of the resistive loading of the -R cell required some circuit modification. Reference [22] suggests the resistive loading can be found by breaking the connection from the emitters of the emitter-followers to the bases of the differential pairs, and placing additional components to maintain the loading on each node as shown in

Fig. 4.21. Through linear AC small signal analysis the input resistance was found to be

$$R_{OL} = 1350\Omega.$$

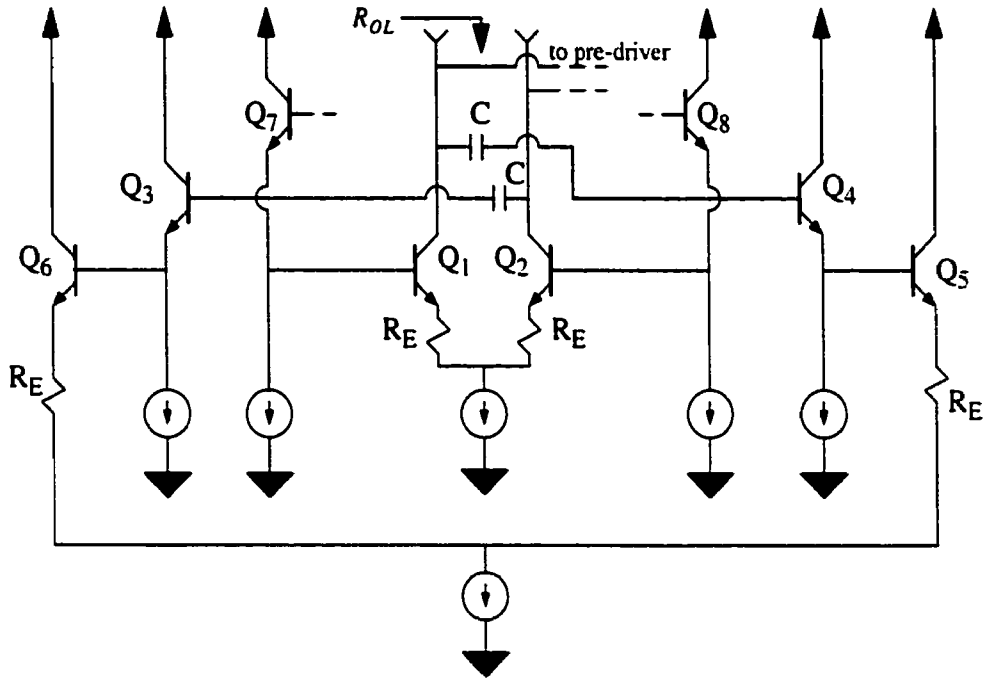


Fig. 4.21: Active part of oscillator with feedback loop opened and extra components added to maintain correct loading.

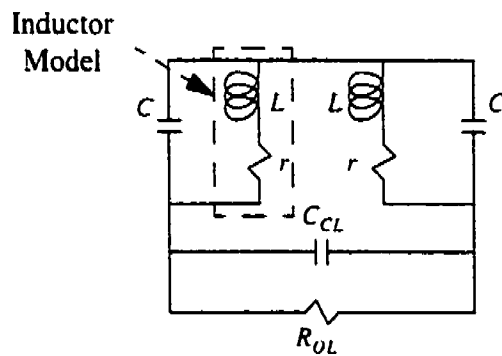


Fig. 4.22: Resonator circuit for the determination of loaded Q.

Using the resonator circuit of Fig. 4.22, simulation revealed a phase slope of

$$\frac{d\phi}{d\omega} = 2.36 \times 10^{-10}, \text{ which (using (EQ 4.10)) lead to a loaded Q of 8.64.}$$

The noise power in the resonator was not found directly. Instead the noise voltage across the terminals of the circuit in Fig. 4.21 was determined by placing a resistor, equal to the resistance of the resonator at the resonant frequency, across the terminals and running a linear small signal noise simulation as suggested by [22]. The simulation provided a squared noise voltage value of 127 aV^2 , which is related to the noise power by

$$2FkT = \frac{v_n^2}{\text{Re}\{z_{\text{resonator}}\}} \quad (\text{EQ 4.70})$$

The ratio of noise power to signal power was then simplified to

$$\frac{2FkT}{P_{\text{sig}}} = \frac{\frac{v_n^2}{\text{Re}\{z_{\text{resonator}}\}}}{\frac{V_{\text{sig}}^2}{\text{Re}\{z_{\text{resonator}}\}}} = \frac{v_n^2}{V_{\text{sig}}^2} \quad (\text{EQ 4.71})$$

With the previously simulated values, the phase noise of the oscillator was estimated at 1MHz offset.

$$PN = \frac{\omega_n^2}{8Q^2 \Delta\omega^2} \left[\frac{v_n^2}{V_{\text{sig}}^2} \right] = \frac{4\pi^2 (11.65 \times 10^9)^2}{32\pi^2 (8.64)^2 (1 \times 10^6)^2} \left[\frac{127 \times 10^{-18} \text{V}^2}{0.045 \text{V}^2} \right] = 6.41 \times 10^{-10} \quad (\text{EQ 4.72})$$

Phase noise is typically specified in units of dBc/Hz which are obtained by taking 10 times the log of (EQ 4.72).

$$10\log(PN) = -92 \text{ dBc/Hz} \quad (\text{EQ 4.73})$$

Values of phase noise calculated at offset frequencies of 1KHz, 10KHz and 100kHz appear in Table 4.2. These estimated values of phase noise indicated the designed oscillator would exceed the targeted phase noise by 30dB at each offset frequency.

Offset Frequency	Target Value (dBc/Hz)	Estimated Value (dBc/Hz)
1kHz	-59	-32
10kHz	-79	-52
100kHz	-99	-72
1MHz	-119	-92

Table 4.2: Targeted and estimated phase noise values for the bias current tuned oscillator.

Notice the ω_n value used in (EQ 4.72) was $\omega_n = 2\pi(11.65 \times 10^9)$ rad/s, not the $\omega_n = 2\pi(14.9 \times 10^9)$ rad/s simulated large signal output angular frequency of the oscillator. 11.65GHz was used because small signal simulation of the oscillator indicated that was the initial startup frequency of the oscillator. The 28% shift in oscillation frequency from 11.65GHz to 14.5GHz indicates the transistor parasitics (which are on the same order as the resonator component values) change significantly as the oscillation signal power grows.

Another important aspect to note is the assumed cancellation of impedances in (EQ 4.71). V_{sig} was determined from large signal analysis and had a frequency of 14.9GHz, v_n was found from small signal linear analysis at 11.65GHz. As demonstrated by the large shift in oscillation frequency, the impedance across which V_{sig} was deter-

mined, was not the same impedance over which v_n was found. Therefore the cancellation of impedances in (EQ 4.71) must be considered a rough approximation.

The above phase noise estimation was primarily based on small signal startup conditions, not the steady-state large signal conditions under which the oscillator operates and phase noise was measured. The estimated phase noise was therefore only a “best guess” at what the oscillator’s measured phase noise would be. Phase noise estimation remains a difficult and poorly understood procedure. This is an area that requires further research.

It should also be noted that the estimation of phase noise did not include any flicker noise contribution as discussed in Section 4.2. The oscillator phase noise was therefore anticipated to be greater than the estimated phase noise at small offset frequencies, and to approach the estimated phase noise at large offset frequencies. These small offset frequencies and large offset frequencies were not possible to quantify due to the lack of a flicker noise corner frequency as mentioned in Section 4.2.

4.6 Summary

This chapter discussed parallel LC resonators with loss, requirements for sustained oscillation, and the estimation of phase noise using Leeson’s equation. A discussion of cross coupled -R cells was presented followed by an explanation of frequency tuning through bias current manipulation. The design of the bias current tuned oscillator fabricated as part of this study was then presented followed by a calculation of expected phase noise.

CHAPTER 5: Oscillator Measurement and Results

This chapter presents measured results for the oscillator discussed in Chapter 4. The phase noise of the oscillator was such that measurements had to be performed using a frequency discriminator. To explain why this method of phase noise measurement was used, a brief discussion of the two most common phase noise measurement techniques (using a spectrum analyzer, and using a phase locked reference source) are presented, followed by an explanation of the frequency discriminator method. Phase noise measurements for the oscillator are then presented and discussed, followed by presentation and discussion of measured values for frequency tuning range; output power; frequency pushing and pulling figure; and second harmonic power.

5.1 Phase Noise Measurement

There are several ways of measuring phase noise in oscillators including: direct spectrum measurement using a spectrum analyzer, phase noise conversion to base band using a phase locked loop, or phase noise conversion to base band using a frequency discriminator.

5.1.1 Direct Spectrum Measurement

Direct spectrum measurement is the most readily available method of phase noise measurement, requiring only a spectrum analyzer. The oscillator signal is fed directly into a spectrum analyzer where the power spectral density is measured at the desired offset fre-

quency from the carrier, and compared to the peak signal power. Many spectrum analyzers on the market have a feature to calculate the phase noise based on display marker positions.

This method can be significantly limited by the spectrum analyzer's dynamic range and by the phase noise of the spectrum analyzer's LO. Also, it is not possible to distinguish between phase noise and AM noise using a spectrum analyzer, therefore phase noise measurements using a spectrum analyzer are typically higher compared with measurements taken using a phase locked reference source. It is also very difficult to measure the phase noise of oscillators with a significant amount of carrier drift. Over all, this method of phase noise measurement is the least accurate of all the methods discussed here.

The oscillator tested in this work had approximately 1MHz of short term (less than one second) frequency drift which made phase noise measurements on the spectrum analyzer impossible.

5.1.2 Phase Locked Reference Source Method

The phase locked reference source method uses a reference source phase locked to the signal from the oscillator under test. Fig. 5.1 shows the basic setup for the phase locked reference source method. If the reference source signal and the oscillator signal are at the same frequency and in quadrature (90° out of phase), a mixer into which these signals are fed will down convert the oscillator (and reference source) phase noise to baseband. A full mathematical explanation of this process is provided in the next section. The phase noise

down converted to baseband is filtered from the higher frequency mixer products and then fed to a baseband signal analyzer where it is measured.

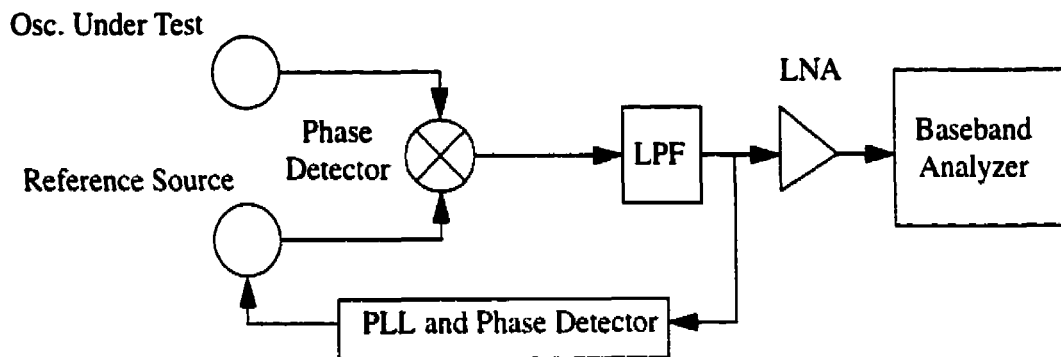


Fig. 5.1: Basic phase detector setup for phase noise measurement.

For accurate measurement the reference source should ideally have much lower phase noise than the oscillator under test. For example if the oscillator under test and the reference source have equal phase noise, the measured oscillator phase noise would be 3dB higher than if the reference source had no phase noise. If the reference source's phase noise is 10dB below that of the oscillator, the measured phase noise will be higher by only 0.4dB.

Quadrature maintenance and frequency locking are automatically performed by the PLL, limiting this measurement technique to oscillators with short term frequency drift within the loop bandwidth of the PLL. The limitation arises because the reference source must lock to the oscillator under test. Consequently for the measurement to be achieved phase lock must be maintained over the drift range of the oscillator under test.

The oscillator tested in this work had a frequency drift of approximately 1MHz which was well beyond the tracking bandwidth of the PLL.

5.1.3 The Frequency Discriminator Method

The frequency discriminator method, also called the delay line method, is similar to the phase locked reference source method in that the test signal phase noise is down converted and measured by a baseband analyzer. Because of this method's insensitivity to oscillator frequency drift, it was used to measure the phase noise of the oscillator reported in this work. The frequency discriminator method compares the oscillator signal to itself. as a result signals fed to the phase detector are always at the same frequency.

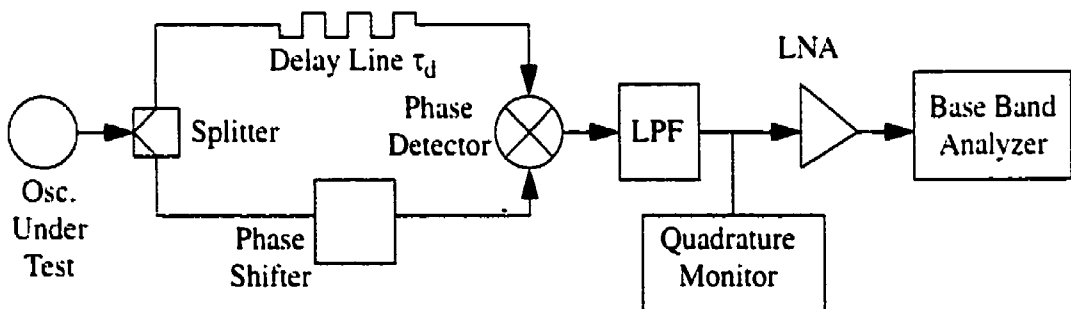


Fig. 5.2: The frequency discriminator method of phase noise measurement [11].

As shown in Fig. 5.2, this method divides the oscillator signal in two with one part going to a delay line, and the other part to a phase shifter as shown in Fig. 5.2. The delayed and phase shifted signals are then multiplied together with a mixer. The phase difference between the two signals is adjusted by the phase shifter such that the output of the phase detector is 0V DC. indicating the delayed signal and the phase shifted signal are

in quadrature. Note that it is equally valid to place the phase shifter in the branch containing the delay line.

The low pass filter removes any harmonics from the phase detector output, leaving only the baseband signal which is the oscillator's phase noise.

A full explanation of the frequency discriminator method, using Fig. 5.2, is now presented.

5.1.4 Theory of the Frequency Discriminator Method

The oscillator phase noise can be thought of as a series of sinusoidal signals frequency modulating the output signal. If we consider one of these signals modulating the oscillator signal with a modulation frequency of f_m , an FM peak deviation of Δf , and a center frequency of f_c , then the oscillator output signal is

$$V_o(t) = V_o \cos\left(2\pi f_c t + \frac{\Delta f}{f_m} \cos(2\pi f_m t)\right) \quad (\text{EQ 5.1})$$

The splitter divides the signal into two equal parts V_R and V_L , where V_R is the part that is fed to the delay line.

$$V_L(t) = V_R(t) = v \cos\left(2\pi f_c t + \frac{\Delta f}{f_m} \cos(2\pi f_m t)\right) \quad (\text{EQ 5.2})$$

where for an ideal splitter $v = V_o / \sqrt{2}$.

After passing through the delay line V_R becomes

$$V_{RD}(t) = v \cos\left(2\pi f_u(t - \tau_d) + \frac{\Delta f}{f_m} \cos(2\pi f_m(t - \tau_d))\right) \quad (\text{EQ 5.3})$$

V_L after passing through the phase shifter becomes

$$V_{LD}(t) = v \cos\left(2\pi f_u t + \frac{\Delta f}{f_m} \cos(2\pi f_m t) + \phi\right) \quad (\text{EQ 5.4})$$

V_{RD} and V_{LD} are multiplied together by the mixer producing

$$\begin{aligned} V_m(t) = K_\phi & \left[\cos\left(2\pi f_u(t - \tau_d) + \frac{\Delta f}{f_m} \cos(2\pi f_m(t - \tau_d)) - 2\pi f_u t - \frac{\Delta f}{f_m} \cos(2\pi f_m t) - \phi\right) \right. \\ & \left. + \cos\left(2\pi f_u(t - \tau_d) + \frac{\Delta f}{f_m} \cos(2\pi f_m(t - \tau_d)) + 2\pi f_u t + \frac{\Delta f}{f_m} \cos(2\pi f_m t) + \phi\right) \right] \end{aligned} \quad (\text{EQ 5.5})$$

$$\begin{aligned} V_m(t) = K_\phi & \left[\cos\left(-2\pi f_u \tau_d - \phi + \frac{\Delta f}{f_m} (\cos(2\pi f_m(t - \tau_d)) - \cos(2\pi f_m t))\right) \right. \\ & \left. + \cos\left(4\pi f_u t - 2\pi f_u \tau_d + \phi + \frac{\Delta f}{f_m} (\cos(2\pi f_m(t - \tau_d)) + \cos(2\pi f_m t))\right) \right] \end{aligned} \quad (\text{EQ 5.6})$$

where K_ϕ is the phase detector constant.

V_m is then filtered to remove the signal component with angular frequency $4\pi f_u$ giving

$$V(t) = K_\phi \left[\cos\left(-2\pi f_u \tau_d - \phi + \frac{\Delta f}{f_m} (\cos(2\pi f_m(t - \tau_d)) - \cos(2\pi f_m t))\right) \right] \quad (\text{EQ 5.7})$$

Using $2\pi f_m(t - \tau_d) = -(\pi f_m \tau_d - 2\pi f_m(t - \tau_d/2))$ and $2\pi f_m t = \pi f_m \tau_d + 2\pi f_m(t - \tau_d/2)$, V

becomes

$$\begin{aligned} V(t) = K_\phi & \left[\cos\left(-2\pi f_u \tau_d - \phi + \frac{\Delta f}{f_m} \cos(-(\pi f_m \tau_d - 2\pi f_m(t - \tau_d/2)))\right) \right. \\ & \left. - \cos(\pi f_m \tau_d + 2\pi f_m(t - \tau_d/2)) \right] \end{aligned} \quad (\text{EQ 5.8})$$

Making use of the trigonometric relations $\cos(A) = \cos(-A)$ and

$\cos(A - B) - \cos(A + B) = 2\sin(A)\sin(B)$, V becomes

$$V(t) = K_o \left[\cos \left(-2\pi f_o \tau_d - \phi + 2 \frac{\Delta f}{f_m} \sin(\pi f_m \tau_d) \sin(2\pi f_m (t - \tau_d/2)) \right) \right] \quad (\text{EQ 5.9})$$

Recall that the phase shifter is set such that the two input signals (V_{RD} and V_{LD}) are in

quadrature. Thus $2\pi f_o \tau_d + \phi = \frac{\pi}{2}$ and (EQ 5.9) becomes

$$V(t) = K_o \left[\cos \left(-\frac{\pi}{2} + 2 \frac{\Delta f}{f_m} \sin(\pi f_m \tau_d) \sin(2\pi f_m (t - \tau_d/2)) \right) \right] \quad (\text{EQ 5.10})$$

Using the trigonometric relation $\cos(A + B) = \cos(A)\cos(B) - \sin(A)\sin(B)$, V can be expressed as

$$V(t) = K_o \left[\cos \left(-\frac{\pi}{2} \right) \cos \left(2 \frac{\Delta f}{f_m} \sin(\pi f_m \tau_d) \sin(2\pi f_m (t - \tau_d/2)) \right) - \sin \left(-\frac{\pi}{2} \right) \sin \left(2 \frac{\Delta f}{f_m} \sin(\pi f_m \tau_d) \sin(2\pi f_m (t - \tau_d/2)) \right) \right] \quad (\text{EQ 5.11})$$

Since $\cos \left(-\frac{\pi}{2} \right) = 0$, (EQ 5.11) reduces to

$$V(t) = K_o \left[\sin \left(2 \frac{\Delta f}{f_m} \sin(\pi f_m \tau_d) \sin(2\pi f_m (t - \tau_d/2)) \right) \right] \quad (\text{EQ 5.12})$$

If $2 \frac{\Delta f}{f_m} < 0.2$ then $\sin \left(2 \frac{\Delta f}{f_m} \right) \approx 2 \frac{\Delta f}{f_m}$ and V simplifies to

$$V(t) = 2K_o \frac{\Delta f}{f_m} \sin(\pi f_m \tau_d) \sin(2\pi f_m (t - \tau_d/2)) \quad (\text{EQ 5.13})$$

The baseband analyzer in Fig. 5.2 receives $V(t)$ from the filter and measures its amplitude, ΔV , where

$$\Delta V = 2K_{\phi} \frac{\Delta f}{f_m} \sin(\pi f_m \tau_d) = 2K_{\phi} \pi \tau_d \Delta f \frac{\sin(\pi f_m \tau_d)}{\pi \tau_d f_m} \quad (\text{EQ 5.14})$$

If $f_m < \frac{1}{2\pi\tau_d}$ then $\frac{\sin(\pi f_m \tau_d)}{\pi \tau_d f_m} \approx 1$ and ΔV reduces to

$$\Delta V = K_{\phi} 2\pi \tau_d \Delta f = K_d \Delta f \quad (\text{EQ 5.15})$$

where $K_d = K_{\phi} 2\pi \tau_d$ and is called the frequency discriminator constant.

(EQ 5.15) shows the frequency discriminator makes the peak frequency deviation of a sinusoidal signal proportional to the amplitude of the voltage signal fed to the baseband analyzer. If the frequency deviation is due to noise instead of a tone, Δf (now the peak frequency fluctuation) becomes a function of f_m , and ΔV is proportional to Δf .

$$\Delta V(f_m) = K_d \Delta f(f_m) \quad (\text{EQ 5.16})$$

(EQ 5.16) can be rearranged to solve for Δf :

$$\Delta f(f_m) = \frac{\Delta V(f_m)}{K_d} \quad (\text{EQ 5.17})$$

The root mean square value of $\Delta f(f_m)$ can then be used in the equation

$$S_{\Delta f}(f_m) = \frac{\Delta f_{rms}^2(f_m)}{BW} \quad (\text{EQ 5.18})$$

where $S_{\Delta f}$ is the spectral density of frequency fluctuations (a measure of phase noise), and BW is the bandwidth over which $\Delta f_{rms}^2(f_m)$ is measured. Another fundamental description of phase noise on a per-hertz basis is S_ϕ , the spectral density of phase fluctuations. It can be found from $S_{\Delta f}$ using the relation

$$S_\phi(f_m) = \frac{S_{\Delta f}(f_m)}{f_m^2} \quad (\text{EQ 5.19})$$

Phase noise is typically given as $L(f_m)$ which, at a certain offset frequency (f_m) from the carrier, is defined as the ratio of the power in one phase modulation sideband to the total signal power. $L(f_m)$ is expressed in dB relative the carrier, where the carrier power is assumed to be approximately equal to the total signal power. Provided this approximation is true, $L(f_m)$ is a valid description of phase noise and is related to S_ϕ by the relation:

$$L(f_m) = \frac{S_\phi(f_m)}{2} \quad (\text{EQ 5.20})$$

Reference [11] suggests the approximation is valid if the peak phase deviation of the signal does not exceed 0.2rad. If the peak deviation exceeds 0.2rad, then a significant amount of signal power exists in the sidebands, and the carrier power can not be considered as the entire signal power. This requirement is often termed the "small angle criterion." If the small angle criterion is not satisfied phase noise should be given as either $S_{\Delta f}$ or S_ϕ .

$L(f_m)$ is usually given in the units dBc/Hz which is found by taking the base ten logarithm of the result of (EQ 5.20) and multiplying by ten.

$$L(f_m) = 10 \log \left(\frac{S_{\phi}(f_m)}{2} \right) \quad (\text{EQ 5.21})$$

5.1.5 Selection of the Delay Line

The HP3048A phase noise measurement set that was used to measure the phase noise of the oscillator provided the phase detector, baseband analyzer, and a programmed routine to find K_d . The only decision left to the user was the selection of the delay line.

(EQ 5.14), reprinted here for convenience

$$\Delta V = 2\pi\tau_d \Delta f \frac{\sin(\pi f_m \tau_d)}{\pi \tau_d f_m}$$

shows that the voltage signal fed to the base band analyzer will have a $\frac{\sin x}{x}$ characteristic

(Fig. 5.3) with nulls at

$$f_m = \frac{N}{\tau_d} \quad (\text{EQ 5.22})$$

where $N = 1, 2, 3, \dots$

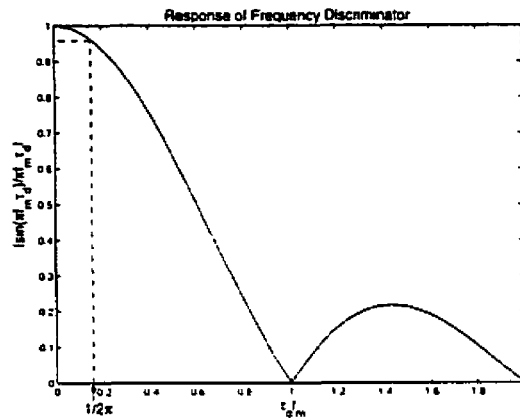


Fig. 5.3: The generic response of a frequency discriminator.

While corrections can be made to the results to account for the $\frac{\sin x}{x}$ characteristic.

generally a value for τ_d is selected that satisfies $\frac{\sin(\pi f_m \tau_d)}{\pi \tau_d f_m} = 1$. If τ_d is selected such that

$f_m < \frac{1}{2\pi\tau_d}$, the $\frac{\sin x}{x}$ term can be ignored with a maximum 4% error.

(EQ 5.14) shows that τ_d also affects the sensitivity of the discriminator. That is the higher τ_d , the greater ΔV becomes. However, increasing τ_d reduces the range of offset frequencies over which the condition $f_m < \frac{1}{2\pi\tau_d}$ is satisfied. As well, increasing τ_d means the signal must travel through a longer length of transmission line, which leads to greater signal attenuation. In theory this does not affect the sensitivity of system, however, in practice the mixer (phase detector) at the output of the delay line is power sensitive. Less input power will yield a lower K_o and therefore reduce system sensitivity. A value for τ_d

should be selected that is as large as possible while maintaining enough power at the input to the mixer (0dBm in the case of the HP3048A), and satisfying the condition $f_m < \frac{1}{2\pi\tau_d}$.

The non-delay path in Fig. 5.2 is usually less lossy than the delay path. Because of this, the signal in the non-delay path is stronger and is therefore usually used to drive the high power (7 - 10dBm) mixer port of the HP3048A.

5.2 Oscillator Measurements and Analysis

5.2.1 Phase Noise Measurements

Two oscillators designated Osc1 and Osc2 were measured. Osc1 was used in phase noise measurements. Because the phase noise measurements took place over several weeks, and required multiple reprobings of Osc1, the probe pads of Osc1 suffered significant wear. Thus Osc1 was only used for phase noise measurements and a second oscillator, Osc2, was used for all the other measurements.

Osc1 was interfaced to the measurement equipment using wafer probes and a wafer probing station (Fig. 5.4). Two DC voltage supplies were used to vary the emitter-follower current (V_{efc}) and the differential pair current (V_{tail}).

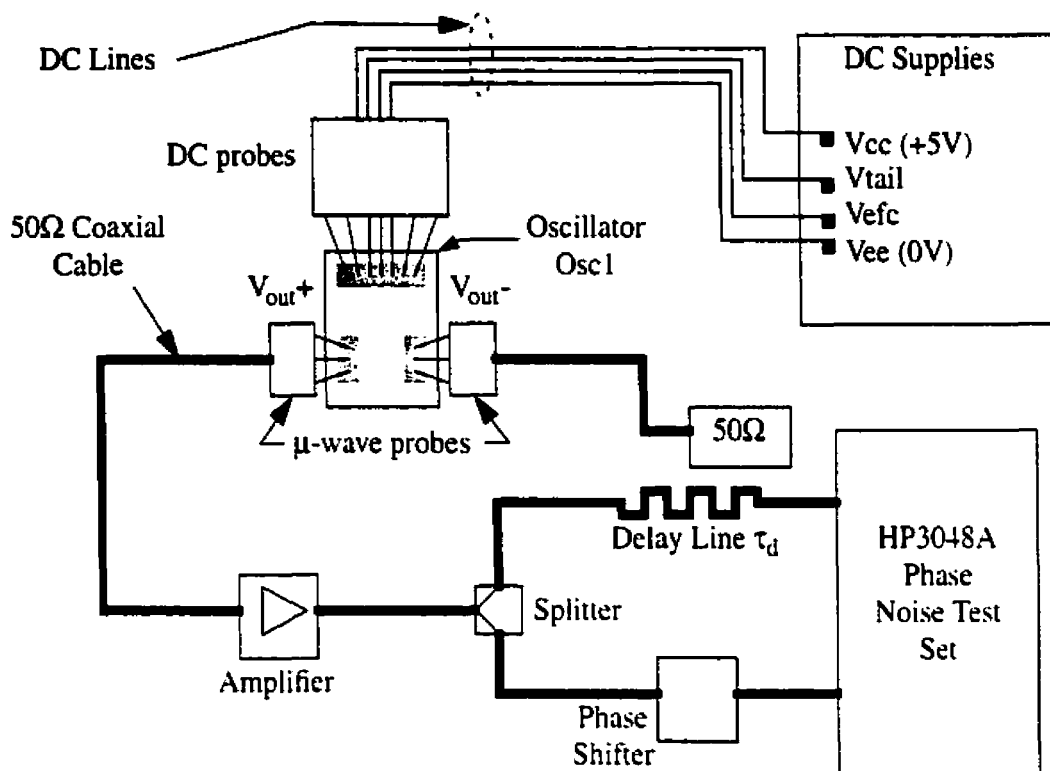


Fig. 5.4: Phase noise measurement equipment and connections.

In order to connect the differential oscillator output to the single-ended equipment inputs, one side of the oscillator's output was terminated in 50Ω and the other side was used as a single ended output. As a consequence the oscillator output power to the measurement system was reduced by 3dB. An HP83006A amplifier, with a gain of 20dB and a noise figure of 8dB, was placed at the input to the splitter to boost the oscillator signal power. The noise floor of the measurement system was increased by 8dB because of the amplifier. This was not a problem because the oscillator's phase noise side lobes were >40dB above the noise floor at the measurement offset frequencies.

The signal from Osc 1 was split in two using an HP11667B resistive power divider with 6dB of loss from the input port to either output port. The delay line was implemented using enough Sucoform 86 coaxial cable (from Huber and Suhner) to provide a delay (τ_d) of 14.5ns. Delay line attenuation was 10.9dB. Delay line characterization was conducted using an HP8510C network analyzer. The phase shifter was produced by Sage Laboratories, model number 6705K-2, serial number 135. The coaxial cables were Huber and Suhner Sucoflex 100 with K connectors. Before each measurement, the system was calibrated using the “derive from FM rate and deviation” method outlined in reference [12].

Offset Frequency (Hz)	Oscillator Signal Frequency				
	10.5GHz	11GHz	11.5GHz	12GHz	12.3GHz
1×10^{-2}	34	32	29	24	21
1×10^{-3}	3	1	-2	-5	-7
1×10^{-4}	-25	-27	-30	-34	-37
1×10^{-5}	-52	-54	-58	-60	-63
1×10^{-6}	-76	-78	-81	-84	-86
1×10^{-7}	-94	-98	-102	-104	-105

Table 5.1: Spectral density of phase noise fluctuations (dBr/Hz) for five different oscillator signal frequencies.

Table 5.1 shows measured values of phase noise, expressed as the spectral density of phase noise fluctuations, at various offset frequencies and oscillation frequencies. The spectral density of phase noise fluctuations is usually given in units of decibel radians per hertz (dBr/Hz). Table 5.1 shows that as the oscillation frequency decreases the phase noise increases. Although the oscillation frequency tuning bandwidth extended below 10.5GHz, as discussed in Section 5.2.4, phase noise measurements were not taken below

10.5GHz. Below 10.5GHz the oscillator signal's short term frequency drift became so great that the frequency discriminator setup was not able to maintain quadrature between the delayed signal and the phase shifted signal. This was due to the frequency sensitivity of the phase shifter, which translated frequency drift into a fluctuating phase deviation from the quadrature condition required by the phase detector of the frequency discriminator. The HP3048A phase noise measurement test set used in this measurement tolerated small deviations from quadrature; however when the oscillator was tuned below 10.5GHz the deviations from quadrature exceeded the acceptable range of the test set. Thus phase noise measurements below 10.5GHz were not successfully performed.

Plots of phase noise for oscillation frequencies of 10.5GHz, 11GHz, 11.5GHz, 12GHz, and 12.3GHz are presented in the following figures. Included on each plot is a dashed line [11] indicating the small angle approximation limit, below which $L(f_m)$ is valid as discussed in Section 5.1.4. Because the measured phase noise of the oscillator exceeded the values defined by the small angle approximation limit, phase noise will be discussed in units of dB_r/Hz rather than dB_c/Hz for the remainder of this document.

Also included on each plot is the condition $f_m = \frac{1}{2\pi\tau_d}$ which indicates the upper offset frequency limit of the frequency discriminator. Phase noise values to the right of the $f_m = \frac{1}{2\pi\tau_d}$ line, are not valid for reasons discussed in Section 5.1.5.

Some of the phase noise plots have spurs, which result from stray signals leaking into the measurement system. Typically these spurs can be ignored as they do not represent noise generated by the oscillator under test. In Fig. 5.6 and Fig. 5.9 spurs appear at 10MHz offset which was one of the offset frequencies of interest. In order to obtain the phase noise values in Table 5.1 for these cases, the values directly before and after the spur were averaged.

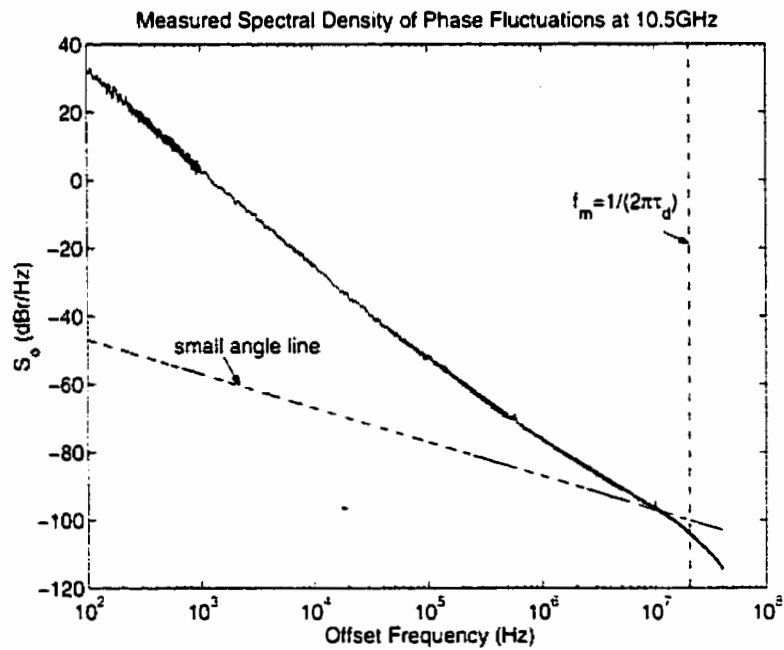


Fig. 5.5: Oscillator phase noise at 10.5GHz oscillation frequency.

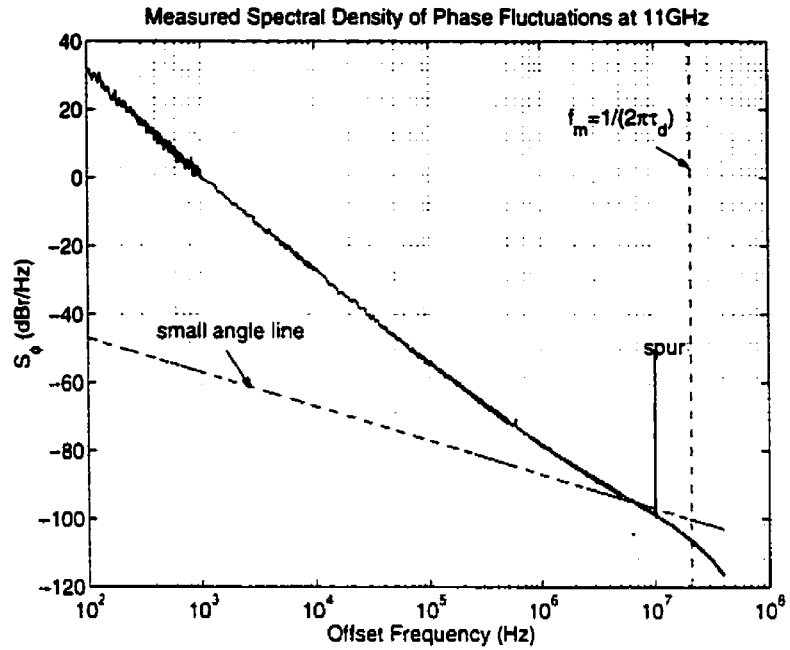


Fig. 5.6: Oscillator phase noise at 11GHz oscillation frequency.

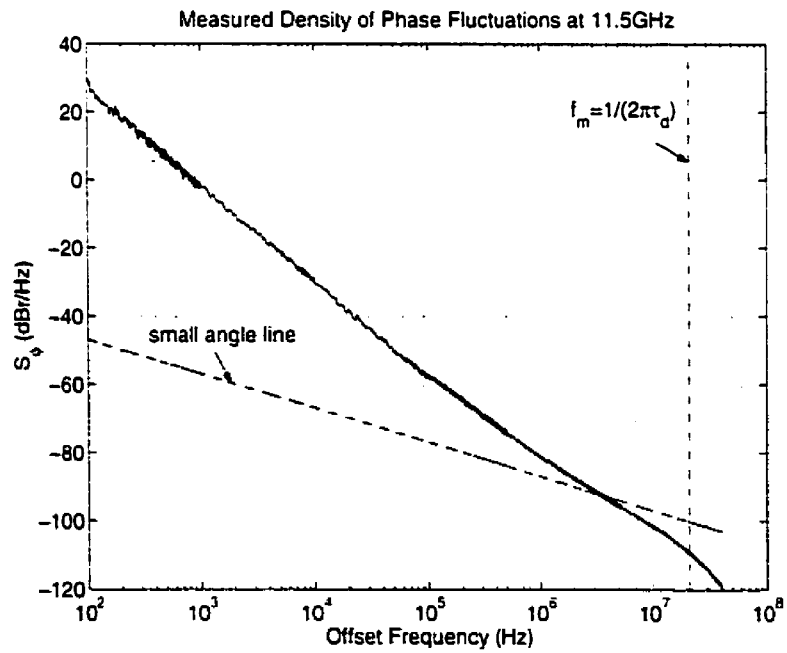


Fig. 5.7: Oscillator phase noise at 11.5GHz oscillation frequency.

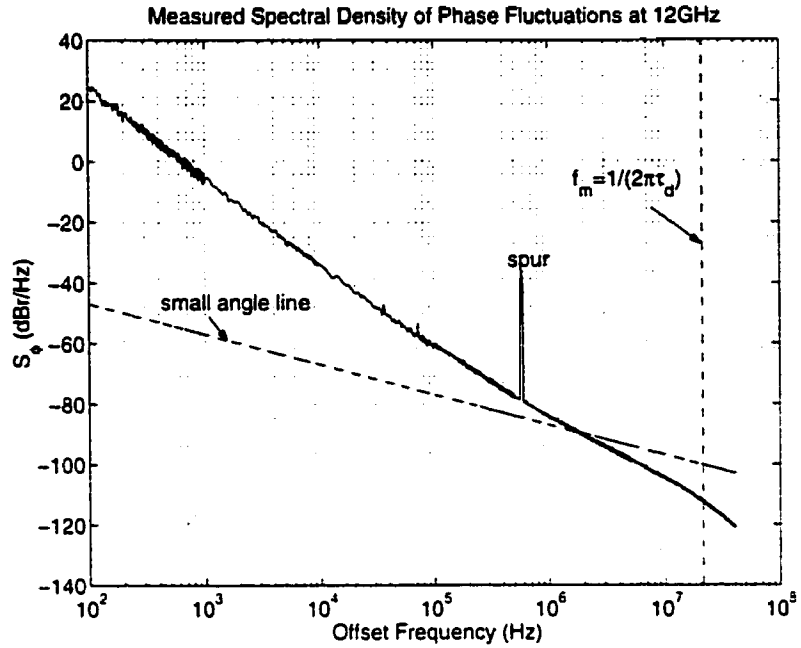


Fig. 5.8: Oscillator phase noise at 12GHz oscillation frequency.

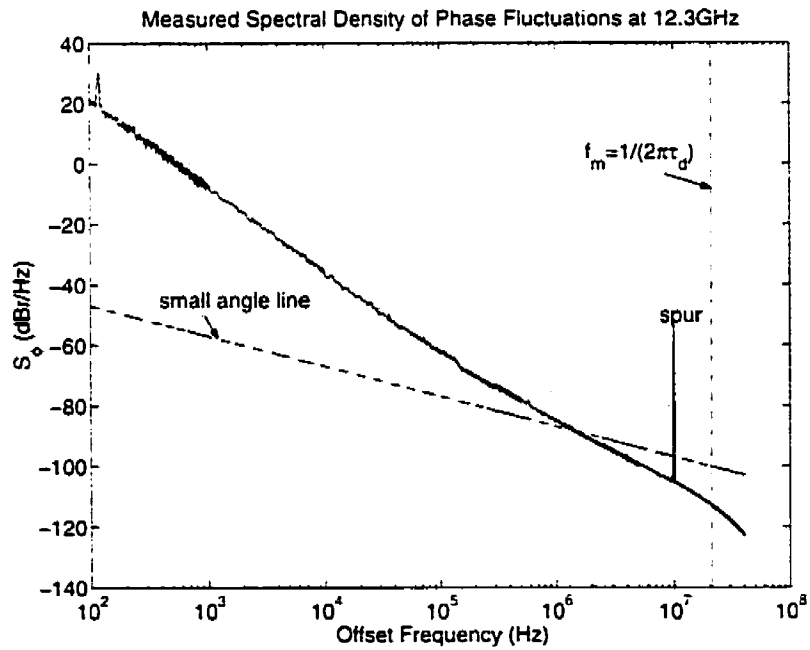


Fig. 5.9: Oscillator phase noise at 12.3GHz oscillation frequency.

5.2.2 Comparison of Estimated Phase Noise to Measured Phase Noise

The phase noise estimation made in Section 4.5.5 was based on simulation results of the oscillator running at 100MHz below its maximum oscillation frequency. Fig. 5.10 shows the measured oscillator phase noise at 100MHz below the peak oscillation frequency (12.3GHz) along with the estimated phase noise as calculated in Section 4.5.5, and the targeted phase noise. The measured phase noise was within <8dB of the estimated phase noise over the offset frequency range of 200kHz to 10MHz, where the measured phase noise trace has a slope of approximately -20dB/decade. The largest difference between the measured and estimated phase noise was 33dB, which occurred at the smallest offset frequency (100Hz) where the measured phase noise trace has a slope of approximately -30dB/decade.

Flicker noise contributions, decrease as the offset frequency increases. Because of the lack of any flicker noise considerations in the phase noise estimation as mentioned in Section 4.5.5, the difference between measured and estimated phase noise was expected to decrease as the offset frequency increased as shown in Fig. 5.10.

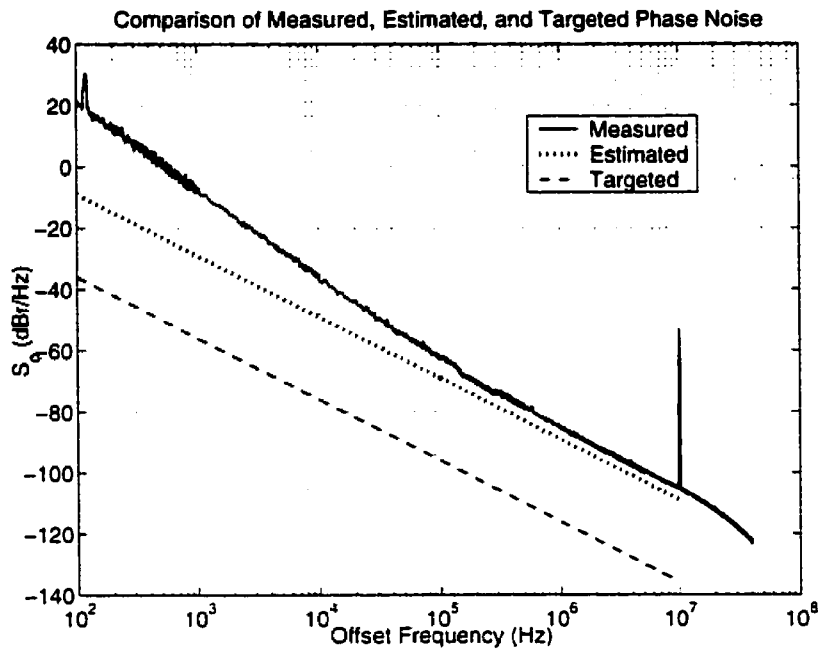


Fig. 5.10: Oscillator phase noise at 12.3GHz compared to estimated and targeted phase noise.

5.2.3 Reducing Oscillator Phase Noise

As shown in Fig. 5.10 the oscillator phase noise was well above the targeted phase noise over the measured offset frequency range. The equation used to estimate phase noise ((EQ 4.37) reproduced below for convenience) indicates reductions in phase noise could have been achieved by increasing the signal power in the resonator (P_{sig}), and by increasing the loaded Q of the resonator.

$$PN = \frac{\omega_p^2}{8Q^2 \Delta\omega^2} \left(\frac{2FKT}{P_{sig}} \right) \quad (\text{EQ 5.23})$$

The simulated voltage swing across the resonator was $0.6V_{pk-pk}$, or $0.045V_{rms}^2$. For comparison, a voltage swing of $2.8V_{pk-pk}$, or $1V_{rms}^2$, across the resonator would have dropped the phase noise by 13.4dB according to (EQ 5.23).

With the transistor sizes selected as discussed in Section 4.5.2, simulations revealed the oscillation amplitude could have been increased by increasing the value of C in the circuit of Fig. 4.15 (reproduced in Fig. 5.11 for convenience). Simulations showed that increasing C increased the coupling of the -R cell to the resonator causing more power to be delivered to the resonator. Increasing C also increased the capacitance presented by the -R cell to the resonator pulling the oscillation frequency below the targeted range. Increasing the resonator signal amplitude while maintaining the desired frequency would involve finding an optimum combination of transistor sizes and value of C . This is an area that requires future work.

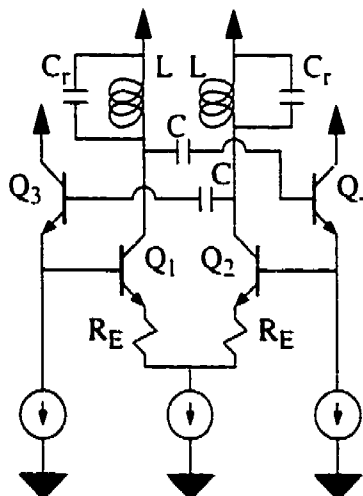


Fig. 5.11: Bias current controlled oscillator.

(EQ 5.23) shows phase noise reduction could also have been achieved by increasing the loaded Q of the resonator. Rearranging (EQ 5.23) to solve for Q , and using the targeted phase noise value of -119dBc/Hz at 1MHz offset indicates the resonator loaded Q would have required a value of 195. This value of resonator loaded Q far exceeds even the unloaded resonator Q of 20. Achieving a loaded Q of 195 from an integrated resonator on low resistivity silicon ($10\Omega\text{cm}$) was not possible using the inductors presented in this study.

5.2.4 Tuning Range and Output Power Measurements

The setup shown in Fig. 5.12 was used to measure the tuning range of the oscillator. Because the oscillator had two tuning ports, the measurements were performed by first setting the oscillator tail current tuning control line (V_{tail}), and then varying the emitter follower current control line voltage (V_{efc}). The oscillator used for these measurements (Osc2) was not the same oscillator used in the phase noise measurements. A notable difference between the two oscillators was the peak oscillation frequency. Osc1 could be tuned to produce a maximum 12.4GHz signal, where as Osc2 could be only be tuned to a maximum of about 12.3GHz . It was calculated that a change of 5fF in the parasitic capacitance associated with the resonator was required to produce the observed frequency change. Given that parasitics comprise more than half of the resonator capacitance, this

difference in peak oscillation frequency was attributable to variations in the fabrication process.

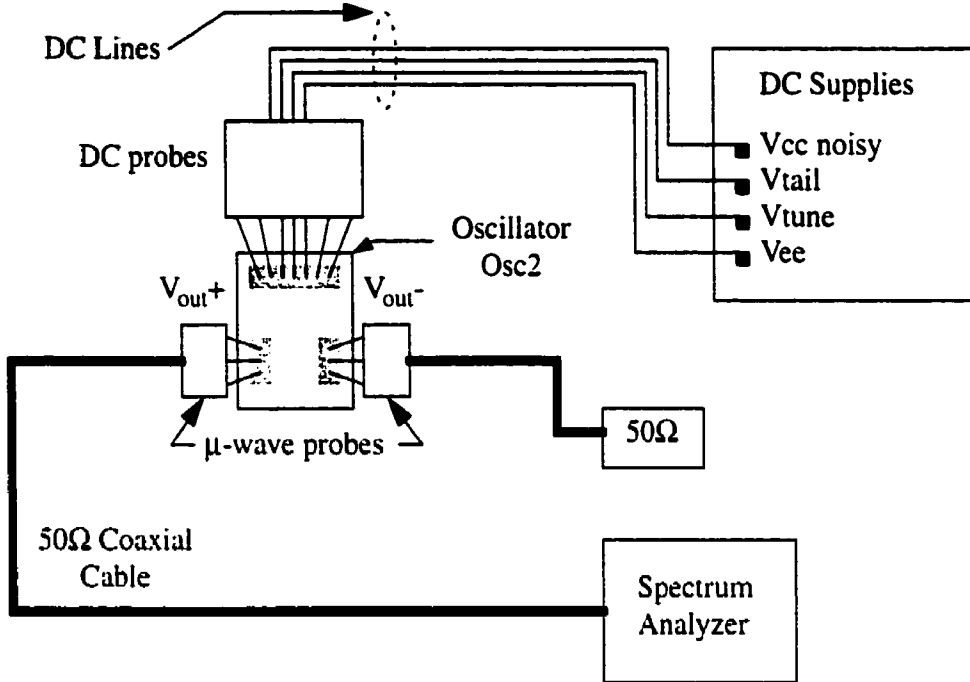


Fig. 5.12: Setup for oscillator measurements using a spectrum analyzer.

The oscillation frequency values shown in Table 5.2 and plotted in Fig. 5.13 were measured using a Rhode & Schwarz FSIQ26 Signal Analyzer. Resolution and video bandwidths of 3MHz were chosen in order to cover the 1MHz short term frequency drift of the oscillator signal.

Tuning characteristics at different values of oscillator differential pair bias current (I_{tail}) are plotted in Fig. 5.13. It should be noted that values of I_{tail} and I_{efc} (the bias current in each emitter-follower) could not be directly measured. Therefore the values of bias

currents given throughout the remainder of this document were found from SpectreRF simulations of the oscillator circuit operating under the measurement conditions.

I_{efc} (mA)	Differential Pair Current - I_{tail}							
	1.5mA	2.4mA	3.4mA	4.4mA	5.4mA	6.4mA	7.4mA	8.4mA
0.45	11.537	11.014	10.469	10.048	9.792	-	-	-
0.78	12.111	11.822	11.374	10.818	10.233	9.782	9.563	-
1.1	12.218	12.025	11.668	11.159	10.593	9.997	9.624	9.436
1.5	12.227	12.068	11.775	11.306	10.755	10.177	9.667	9.441
1.8	12.193	12.055	11.804	11.379	10.850	10.249	9.676	9.417
2.1	12.127	12.010	11.796	11.415	10.898	10.210	9.631	-
2.5	12.039	11.938	11.751	11.401	10.858	10.017	9.540	-
2.8	11.917	11.836	11.660	11.305	10.638	9.754	-	-
3.1	11.744	11.695	11.496	11.052	10.014	-	-	-
3.5	11.425	11.435	11.135	10.101	-	-	-	-

- indicates values are beyond operating range of oscillator

Table 5.2: Frequency tuning range of oscillator. All frequencies are in GHz.

The oscillator's maximum frequency of about 12.3GHz was well below the desired and simulated 15GHz maximum frequency. The 18% reduction in maximum oscillation frequency was the result of several factors. The first was the capacitance due to interconnect metallization. The software tool used to layout the oscillator calculated the metallization capacitance added about 46fF of effective capacitance to the resonator that was not accounted for in the design of the oscillator.

The second factor was the assumed inductance of the octagonal spiral used in the resonator. Spiral inductor measurements from Chapter 3 indicate the octagonal spiral used in the oscillator had an inductance of 0.53nH instead of the assumed 0.5nH. The inductance due to the metal leading to and from the inductor (a total of 143 μ m) was not considered.

Libra simulations, using the optimized substrate parameters presented in Section 2.4.3, associated 0.08nH of inductance to the lengths of metal leading to and from the inductor.

With the oscillator tuned to 15GHz, Spectre RF predicted the resonator capacitance plus the parasitic transistor capacitances would add up to provide an effective resonator capacitance of 225fF. Adding the 46fF parasitic metallization capacitance to 225fF yields 271fF of effective resonator capacitance. Replacing the assumed 0.5nH inductance with the actual 0.53nH spiral and adding the 0.08nH of feedline inductance yields a total of 0.61nH of inductance in the resonator. Using these new resonator component values changes the expected maximum oscillation frequency to 12.37GHz.

$$\omega = \frac{1}{\sqrt{LC}} = \frac{1}{\sqrt{(271 \times 10^{-15})(0.63 \times 10^{-9})}} = 7.78 \times 10^{10} \text{ rad or } 12.37 \text{ GHz} \quad (\text{EQ 5.24})$$

This new expected value of maximum oscillation frequency is very close to the measured maximum frequency of 12.4GHz for Osc1.

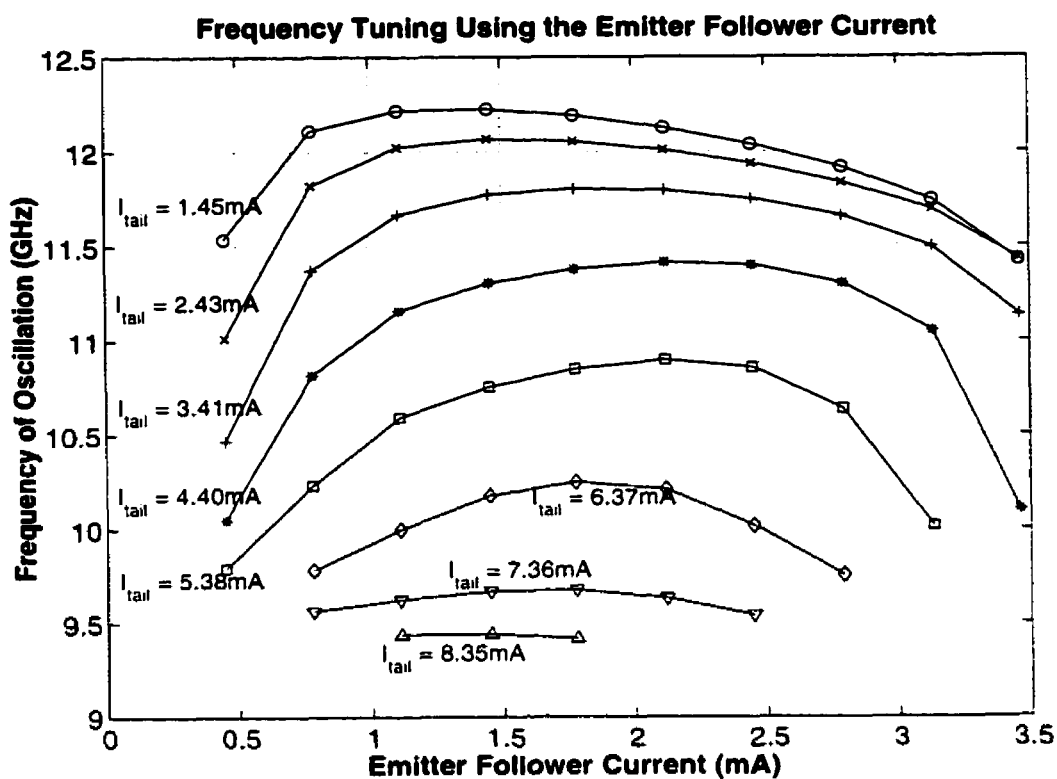


Fig. 5.13: Frequency tuning range of oscillator.

Measurements of oscillator signal power were also performed using the Rhode & Schwarz Signal Analyzer with resolution bandwidth and video bandwidth set to 3MHz. The measured values had 2.22dB added to account for cable loss between the probes and the signal analyzer, and 3dB added to account for the half of the differential signal that was not routed to the signal analyzer. The signal loss between the wafer probes and the probe pads was not characterized and therefore could not be accounted for in the power

measurements provided in Table 5.3. Fig. 5.14 shows plots of oscillator output power at different tuning voltages.

I_{efc} (mA)	Differential Pair Current - I_{tail}							
	1.5mA	2.4mA	3.4mA	4.4mA	5.4mA	6.4mA	7.4mA	8.4mA
0.45	-10.68	-9.57	-9.82	-12.65	-16.70	-	-	-
0.78	-6.43	-4.80	-4.78	-5.17	-6.03	-8.10	-11.02	-
1.1	-5.79	-4.05	-3.45	-3.75	-4.28	-5.46	-7.01	-14.54
1.5	-5.50	-3.72	-3.37	-4.22	-3.79	-4.04	-5.02	-11.04
1.8	-5.80	-3.40	-3.45	-3.58	-3.28	-3.73	-4.72	-11.44
2.1	-5.70	-4.05	-3.47	-3.43	-3.25	-3.92	-5.41	-
2.5	-5.92	-4.18	-3.26	-3.52	-3.29	-4.97	-8.03	-
2.8	-7.12	-4.03	-3.24	-4.12	-3.80	-6.81	-	-
3.1	-7.45	-4.39	-3.67	-3.64	-6.47	-	-	-
3.5	-9.82	-5.21	-4.32	-8.45	-	-	-	-

- indicates values are beyond operating range of oscillator

Table 5.3: Oscillator output power over tuning range.

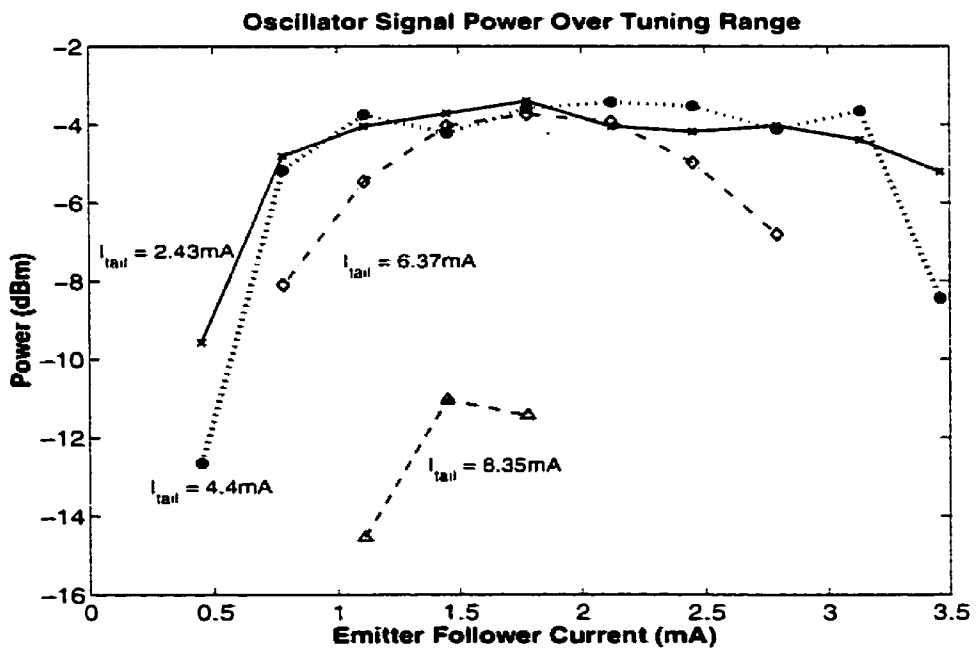


Fig. 5.14: Output power of oscillator over tuning range.

5.2.5 Frequency Pushing

Frequency pushing refers to the sensitivity of an oscillator's output signal frequency to supply voltage variations. It is measured by increasing the oscillator's supply voltage by one volt above the nominal value and observing the change in output frequency [24]. The supply voltage is then dropped to one volt below the nominal and again changes in the output frequency are measured. Frequency pushing is usually measured at frequencies across the tuning range of the oscillator. Table 5.4 gives the pushing figure and measured output frequency values at different oscillation frequencies for Osc2. Note the values of emitter-follower current (I_{efc}) and differential pair current (I_{tail}) correspond to nominal supply voltage (5V) operating conditions.

I_{tail} (mA)*	I_{efc} (mA)*	Freq at $V_{bias}=4V$	Freq at $V_{bias}=6V$	Pushing Figure (MHz/V)	Percentage Change per Volt (%/V)
3.2	1.8	11.840GHz	11.880GHz	20	0.17
3.2	2.2	11.787GHz	11.857GHz	35	0.3
3.2	2.9	11.223GHz	11.731GHz	254	2.2
1.7	2.2	12.029GHz	12.107GHz	39	0.32
6.5	2.2	10.505GHz	10.225GHz	-14	0.14

*Current values before bias voltage change.

Table 5.4: Pushing figure of oscillator.

In all but one case in Table 5.4, the oscillator shows little sensitivity to small supply voltage changes. The exception is the 254MHz/V pushing figure which corresponded to a 2.2% change in frequency per volt of supply voltage deviation. This relatively high sensitivity in oscillation frequency was traced back to the operational mode of the differential pair current source transistor. Fig. 5.15 shows the oscillator circuit with current source

transistors. With $I_{\text{tail}}=3.2\text{mA}$, $I_{\text{efc}}=2.9\text{mA}$ and 5V of supply voltage the differential pair current source transistor (Q7 in Fig. 5.15) was operating in the active region. When the supply voltage was raised to 6V the current source transistor maintained active region operation. However, when the supply voltage was dropped to 4V, the current source transistor was pushed into deep saturation. It no longer provided a high impedance at its collector. This altered the base impedance of the differential pair transistors which reflected through the emitter follower transistors and changed the resonator impedance.

The saturation of the differential pair current source indicates that the $\pm 1\text{ V}$ supply voltage change may have been too severe for this oscillator. A more practical supply voltage deviation would have been $\pm 0.1\text{ V}$, which would have maintained the normal operating modes of the transistors in the oscillator circuit.

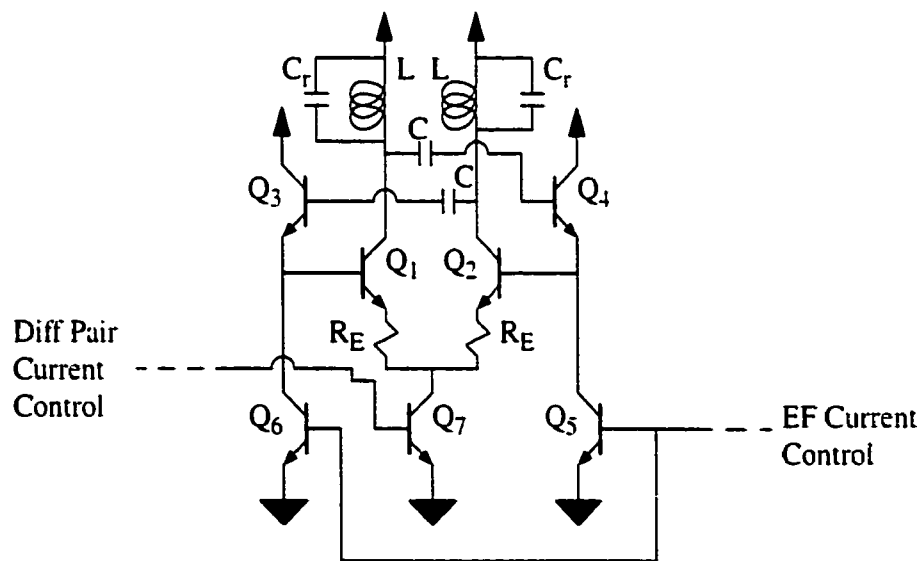


Fig. 5.15: Oscillator circuit with non-ideal current sources.

5.2.6 Second Harmonic Power

The oscillator studied in this work depended on the nonlinear characteristics of the transistors to limit the amplitude of oscillation. When a device is operated in a nonlinear mode, harmonics are generated. Table 5.5 shows second harmonic power at five different tuning voltage values. The second harmonic power is highest relative the fundamental signal (-28.7dB) when $I_{tail}=3.2\text{mA}$ and $I_{efc}=2.2\text{mA}$. The second harmonic suppression of this oscillator was attributed to its differential topology. Third harmonic levels were not measured as the third harmonic frequency far exceeded the measurement bandwidth capability of the Rhode & Schwarz signal analyzer used in these measurements.

I_{tail} (mA)	I_{efc} (mA)	Freq. (GHz)	Fundamental Power (dBm)	Second Harmonic Power (dBm)	Relative Fundamental (dB)
3.2	1.8	11.866	-3.1	-32.5	-29.4
3.2	2.2	11.847	-3.6	-32.3	-28.7
3.2	2.9	11.681	-2.8	-33.3	-30.5
1.7	2.2	12.086	-5.0	-38.5	-33.5
6.5	2.2	10.138	-2.8	-39.7	-36.9

Table 5.5: Second harmonic power of oscillator signal.

5.2.7 Frequency Pulling

Frequency pulling is a measure of changes in the oscillation frequency due to unmatched loads. Typically it is measured by noting the change in frequency due to a load with a 12dB return loss with all possible phases. Fig. 5.16 shows the setup used to measure frequency pulling. The pulling was conducted with two load terminations. The loads consisted of a 6dB loss terminated in the first case with an open circuit, and in the second

case with a short circuit. Under these load termination conditions the return loss of each load was 12dB. Ideally adjustable phase shifters would have been placed between the loads and the couplers on each output. By varying the phase shifters every possible load phase angle could have been achieved. Unfortunately two identical phase shifters were not available for this measurement. As well it would have been very difficult to synchronize the phase shifters in each output line in order to provide each output with the same load. Thus only the open and shorted loads were used in this test.

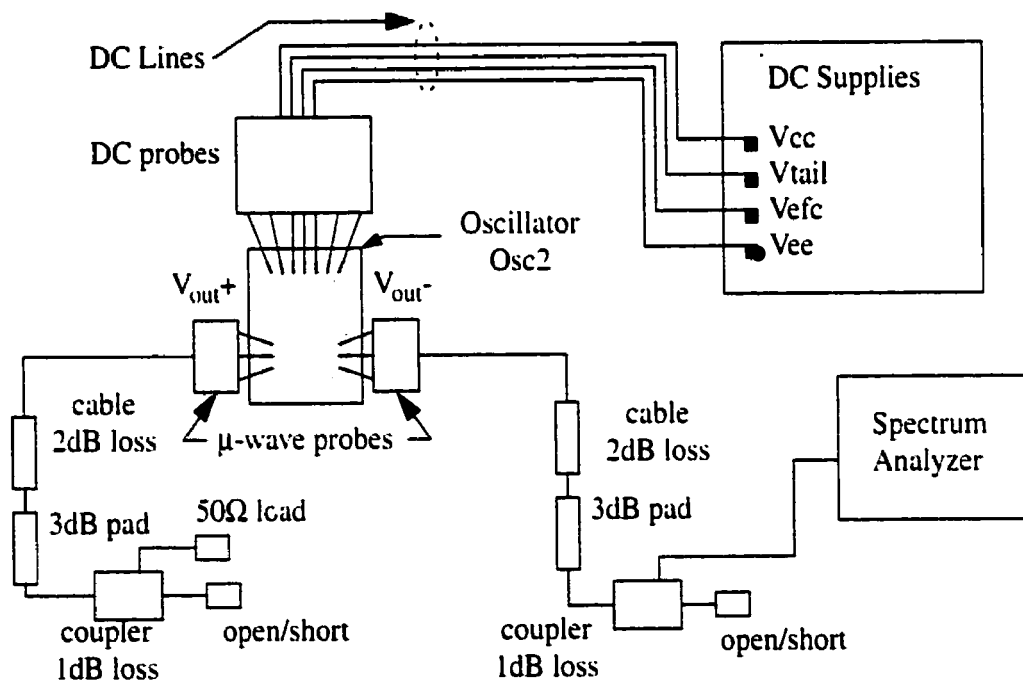


Fig. 5.16: Frequency pulling measurement setup.

The oscillator was operated with $I_{tail}=3.2\text{mA}$ and $I_{efc}=2.2\text{mA}$. Oscillation frequency was measured under loading conditions of short, open, and 50Ω . The output frequency was 11.842GHz for the 50Ω load, 11.840GHz for the short load, and 11.844GHz for the open load, giving a maximum frequency swing of 4MHz or 0.03% relative the carrier fre-

quency. This insensitivity of the oscillator frequency to load changes was attributed to the buffering provided by the two amplifier stages that separate the oscillator differential pair and resonator circuit from the output load.

5.3 Summary

This chapter described the frequency discriminator method of phase noise measurement used to characterize the bias current tuned oscillator's phase noise performance. A discussion of the measured phase noise was then presented. Measurements of tuning range, output power, frequency pushing and pulling figure, and second harmonic power were also discussed.

CHAPTER 6: Conclusion

6.1 Summary

The principle goals of this thesis were: to investigate two different spiral inductor fabrication techniques that were expected to increase inductor quality factor without requiring any special non-production process steps; and to investigate a varactorless oscillator design that used bias currents to tune the oscillation frequency.

Chapter 2 discussed spiral inductor design theory, the two fabrication methods to be evaluated, and the final designs of eight sets of inductors used to evaluate the two fabrication techniques. The first fabrication technique was the use of two parallel metal layers instead of one to implement the inductor windings. The other fabrication technique was the placement of insulating substrate trenches between the windings of the spiral. The methods by which the inductor measurements were to be de-embedded from the probe pads were also discussed.

Chapter 3 examined how the inductors were measured and presented the measured results of the eight sets of fabricated spiral inductors. Based on the results, the merits of each fabrication method were discussed along with the impact of other inductor parameters such as size and shape. The two metal inductors consistently demonstrated a lower quality factor and inductance compared to the basic top metal winding inductors, indicating the two metal winding fabrication technique failed to improve the inductors. The trench inductors demonstrated improvements in Q at or beyond the peak Q frequency

when compared to basic top metal inductors, indicating the trenches can improve inductor performance. The measured results of four square inductors were compared to ADS Momentum simulated results. The poor correlation between the simulated and measured results were attributed to assumptions made by the simulator code.

Chapter 4 presented basic oscillator design theory and the basis of Leeson's phase noise equation. The design of a cross coupled differential pair oscillator with emitter-followers in the feedback path was presented along with an explanation of the unique tuning methods used in the oscillator. The design of a pre-driver and output stage were also discussed, followed by an estimation of the oscillator's phase noise using Leeson's equation that indicated the targeted phase noise level was not going to be met.

Chapter 5 discussed the frequency discriminator method of phase noise measurement used to measure the phase noise of the fabricated oscillator. Phase noise measurements were presented followed by measurements of tuning range, output power, pulling and pushing frequency figures, and second harmonic power. An analysis of discrepancies between expected and measured oscillation frequency was also presented.

6.2 Thesis Contribution

This thesis investigated two means of on-silicon spiral inductor fabrication which can be implemented in a production type process. In the first technique the inductor windings were implemented in a two metal layer structure. This technique yielded significantly lower (7-18%) Q and lower (4-7%) L values compared to inductors with top metal only

windings. The self resonant frequency of the two metal layer inductors was measured to be approximately 4% lower than that of the basic inductors. Based on this work the two metal winding configuration is not recommended as a method of increasing spiral inductor Q.

The second inductor fabrication technique placed insulating substrate trenches between the inductor windings. This method was shown to improve inductor Q at or beyond the peak Q frequency with a maximum peak Q increase of 5% as demonstrated by the 0.4nH octagonal inductor. The use of inter-winding trenches was also shown to slightly increase the self resonant frequency of the spirals. Based on this work the inter-winding trench design is recommended when fabricating on-silicon spiral inductors.

One of the fabricated inductors (the 0.4nH octagonal trench inductor) demonstrated a Q of 20 at 15GHz. This result is, to the author's knowledge, the highest Q obtained from a spiral inductor fabricated in a production type silicon process.

This thesis also demonstrated a unique oscillator whose approximately 2.5GHz (or 23%) tuning range was achieved by varying either or both of two bias currents.

6.3 Future Work

The work presented here produced some questions which would require more research to answer.

While inter-winding trenches were shown to improve Q , no hard evidence could be provided that related the point at which the trenches provided improvement in Q and any other inductor parameters. More work needs to be done in order to estimate and optimize the improvements offered by inter-winding trenches.

A question that was beyond the scope of this work but requires some clarification is which of the two 2-port de-embedding methods used to measure the inductors is more accurate. The discrepancies between the two are significant and need to be resolved.

This work demonstrated an integrated on-silicon oscillator with a varactorless tuning method. The measured phase noise of this circuit was approximately 30dB above the targeted phase noise demonstrating the need for further work on this oscillator.

REFERENCES

- [1] R.E. Collin, Foundations for Microwave Engineering: Second Edition, McGraw-Hill, Inc., New York, pp. 912, 1992.
- [2] W.B. Kuhn and N.K. Yanduru, "Spiral Inductor Substrate Loss Modeling in Silicon RFICs," *Microwave Journal*, pp. 66 - 81, March 1999.
- [3] J.R. Long and M.A. Copeland, "The Modeling, Characterization, and Design of Monolithic Inductors for Silicon RF IC's," *IEEE Journal of Solid-State Circuits*, vol. 32, No. 3, pp. 357 - 369, March 1997.
- [4] C.P. Yue and S.S. Wong, "On-Chip Spiral Inductors with Patterned Ground Shields for Si-Based RF IC's," *1997 Symposium on VLSI Circuits Digest of Technical Papers*, pp. 86 - 86, 1997.
- [5] M.C.A.M. Koolen, "On-wafer High-frequency Device Characterization," *Microelectronic Engineering*, pp. 679 - 686, 1992.
- [6] H. Cho and D.E. Burk, "A Three-Step Method for the De-embedding of High-Frequency S-Parameter Measurements," *IEEE Transactions on Electron Devices*, vol. 38, No. 6, pp. 1371 - 1375, June 1991.
- [7] A.S. Sedra and K.C. Smith, Microelectronic Circuits: Third Edition, Saunders College Publishing, Toronto, pp. 228, 1991.
- [8] G.Gonzalez, Microwave Transistor Amplifiers - Analysis and Design: Second Edition, Prentice-Hall, New York, pp. 394, 1997.
- [9] M.A. Margarit et al., "A Low-Noise, Low-Power VCO with Automatic Amplitude Control for Wireless Applications," *IEEE Journal of Solid-State Circuits*, vol. 34, No. 6, pp. 761 - 771, June 1999.
- [10] S. Chaki et al., "Experimental Study on Spiral Inductors," *Proc. IEEE Microwave Symp. Dig. MTT-S*, 1995.
- [11] *Phase Noise Characterization of Microwave Oscillators - Frequency Discriminator Method*, Product Note 11729C-2, Sept. 1985, Hewlett Packard.
- [12] *HP3048A User's Manual*, Hewlett-Packard

- [13] D.B. Leeson, "A Simple Model of Feedback Oscillator Noise Spectrum," *Proc. IEEE*, vol. 54, No. 2, 1966.
- [14] J.W.M Rogers, "Voltage Controlled Oscillators and High Q Copper Inductors," M. Eng. thesis, Carleton University, Aug. 1999.
- [15] T.H. Lee, The Design of CMOS Radio-Frequency Integrated Circuits, Cambridge University Press, New York, pp. 535, 1998.
- [16] B.G. Streetman, Solid State Electronic Devices: Fourth Edition, Prentice-Hall, Englewood Cliffs, pp. 173-175, 1995.
- [17] D. Crooks. et al., NT35 Electrical Specifications and Layout Design Rules: Version 1S01.2. Unpublished proprietary internal document - Nortel Networks, August, 1999.
- [18] H. Knapp. H.-D. Wohlmuth. J. Bock. and A. Scholz. "22GHz monolithically integrated oscillator in silicon bipolar technology," *Electronics Letters*, Vol. 35, No. 6, pp. 438-439. March 1999.
- [19] P.R. Gray. R.G. Meyer. Analysis and Design of Analog Integrated Circuits: Third Edition, John Wiley & Sons, Inc., pp. 41-45. 1993.
- [20] C.P. Yue. et al.. "A Physical Model For Planar Spiral Inductors On Silicon." *IEDM 96*. pp. 155 - 158. 1996.
- [21] K.K. Clarke. and D.T. Hess. Communication Circuits: Analysis and Design. Krieger Publishing Co.. pp. 35. 1994.
- [22] B. Jansen. K. Negus. D. Lee. "Silicon Bipolar VCO Family for 1.1 to 2.2GHz with Fully-Integrated Tank and Tuning Circuits." *IEEE International Solid State Conference*. 1997. pp. 392-393.
- [23] E. Pettenpaul. et al.. "CAD Models of Lumped Elements on GaAs up to 18GHz." *IEEE Transactions on Microwave Theory and Techniques*, Vol. 36, No. 2, Feb. 1988. pp. 294 - 304.
- [24] Mini-Circuits. *RF/IF Designer's Handbook*. Scientific Components. pp. 15 sec. 15. 1997.
- [25] M. Repeta. et al.. NT55 Electrical Specifications and Layout Design Rules: Version 1W01. Unpublished proprietary internal document - Nortel Networks. December 18. 1998.

APPENDIX A: Emitter Follower Analysis

This appendix derives the expressions for input impedance (R_{in}), output impedance (R_{out}), and voltage gain (A_v) for the emitter follower circuit shown in Fig. A.1. To simplify the analysis $r_o \rightarrow \infty$ is assumed.

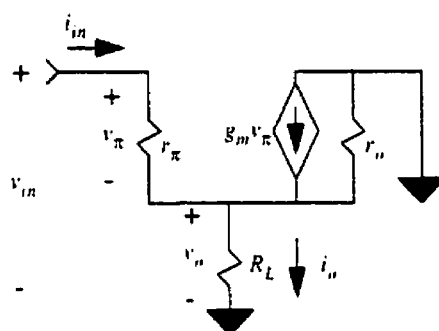


Fig. A.1: Small signal model of emitter follower.

A.1 Input Impedance

Emitter followers offer a high input impedance and a low output impedance and are therefore typically used as buffers between high output impedance sources and low impedance loads. An expression for input impedance can be found from analysis of the small signal circuit in Fig. A.1.

$$v_{in} = v_{\pi} + \left(\frac{1}{r_{\pi}} + g_m \right) v_{\pi} R_L \quad (\text{EQ A.1})$$

$$i_{in} = \frac{v_{in}}{r_{\pi}} \quad (\text{EQ A.2})$$

$$\frac{v_{in}}{i_{in}} = \frac{v_{\pi} + \left(\frac{1}{r_{\pi}} + g_m\right)v_{\pi}R_L}{v_{\pi}/r_{\pi}} \quad (\text{EQ A.3})$$

Using

$$r_{\pi}g_m = \beta \quad (\text{EQ A.4})$$

the input impedance simplifies to

$$z_{in} = \frac{v_{in}}{i_{in}} = r_{\pi} + (1 + \beta)R_L \quad (\text{EQ A.5})$$

A.2 Output Impedance

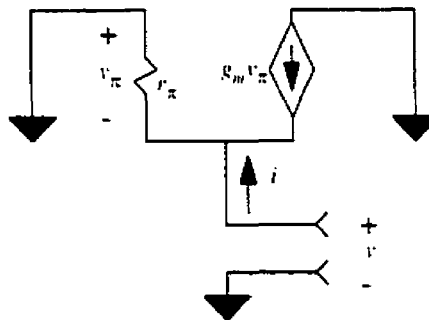


Fig. A.2: Emitter follower small signal circuit connected for output impedance analysis.

The emitter follower output impedance is found through analysis of the circuit in

Fig. A.2.

$$v = -v_{\pi} \quad (\text{EQ A.6})$$

$$i = -g_m v_\pi - \frac{v_\pi}{r_\pi} \quad (\text{EQ A.7})$$

Using (EQ A.4), (EQ A.6), and (EQ A.7) the output impedance is

$$\tilde{z}_{out} = \frac{v}{i} = \frac{r_\pi}{1 + r_\pi g_m} = \frac{r_\pi}{1 + \beta} \quad (\text{EQ A.8})$$

A.3 Voltage Gain

The voltage gain (A_v) of the emitter follower can be found through analysis of the circuit in Fig. A.1.

$$v_o = \left(\frac{v_\pi}{r_\pi} + g_m v_\pi \right) R_L \quad (\text{EQ A.9})$$

$$v_\pi = v_{in} - v_o \quad (\text{EQ A.10})$$

$$r_\pi v_o = (v_{in} - v_o) R_L + g_m r_\pi (v_{in} - v_o) R_L \quad (\text{EQ A.11})$$

$$\text{since } g_m r_\pi = \beta \quad (\text{EQ A.12})$$

$$\frac{v_o}{v_{in}} = \frac{(\beta + 1) R_L}{(\beta + 1) R_L + r_\pi} \quad (\text{EQ A.13})$$

$$A_v = \frac{v_o}{v_{in}} = \frac{R_L}{R_L + \frac{r_\pi}{(\beta + 1)}} = 1 \quad (\text{EQ A.14})$$

APPENDIX B: Proof of (EQ 2.27)

This appendix derives, in a step by step fashion, (EQ 2.27) from Chapter 2 presented here as (EQ B.1) for reference.

$$Y_{ind} = [(Y_{total} - Y_{open})^{-1} - (Y_{short} - Y_{open})^{-1}]^{-1} \tag{EQ B.1}$$

Y_{total} is the Y parameter matrix for the circuit shown in Fig. B.1.

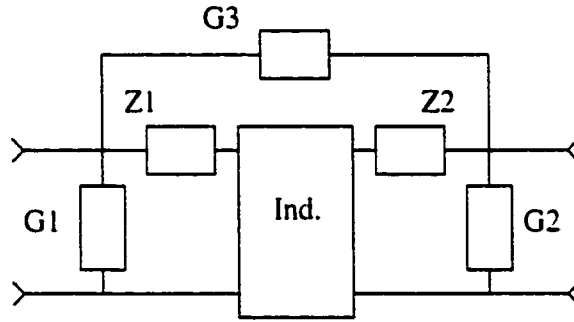


Fig. B.1: Modified Koolen model of an inductor with pad and feed line parasitics.

Y_{open} and Y_{short} are the Y parameters for the open pad structure and shorted pad structure respectively (see Fig. B.2).

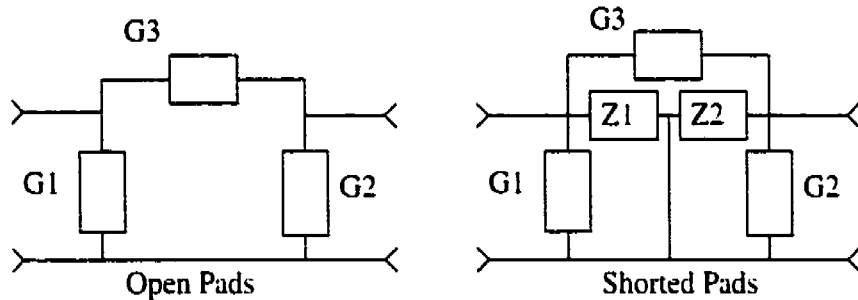


Fig. B.2: Modified versions of Koolen's open and shorted pad parasitics models.

In the following sections the individual Y parameters for each of the matrices in (EQ B.1) are determined.

Y_{total} :

To simplify the following derivation of each Y_{total} parameter, the series feed line impedances are lumped together with the inductor as shown in Fig. B.3, forming another set of Y parameters. Y_s .

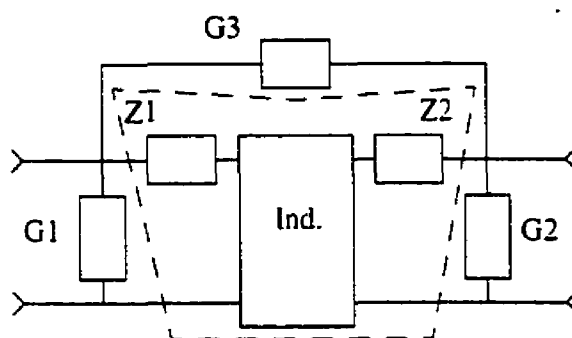


Fig. B.3: Parasitic impedances Z1 and Z2 lumped with the inductor to form the network inside the dashed lines.

By definition

$$Y_s = \begin{bmatrix} Y_{11} & Y_{12} \\ Y_{21} & Y_{22} \end{bmatrix} \quad (\text{EQ B.2})$$

Y_{total} is found by using equations (EQ B.3) to (EQ B.6) from [7].

$$Y_{11} = \frac{I_1}{V_1} \Big|_{V_2=0} \quad (\text{EQ B.3})$$

$$y_{12} = \frac{I_1}{V_2} \Big|_{V_1=0} \quad (\text{EQ B.4})$$

$$y_{21} = \frac{I_2}{V_1} \Big|_{V_2=0} \quad (\text{EQ B.5})$$

$$y_{22} = \frac{I_2}{V_2} \Big|_{V_1=0} \quad (\text{EQ B.6})$$

So,

$$y_{11total} = G1 + G3 + y_{11s} \quad (\text{EQ B.7})$$

$$y_{12total} = -G3 + y_{12s} \quad (\text{EQ B.8})$$

$$y_{21total} = -G3 + y_{21s} \quad (\text{EQ B.9})$$

$$y_{22total} = G2 + G3 + y_{22s} \quad (\text{EQ B.10})$$

which gives a Y parameter matrix of

$$Y_{total} = \begin{bmatrix} G1 + G3 + y_{11s} & -G3 + y_{12s} \\ -G3 + y_{21s} & G2 + G3 + y_{22s} \end{bmatrix} \quad (\text{EQ B.11})$$

Y_{open} :

Y_{open} is found using (EQ B.3) to (EQ B.6) and the open pad circuit shown in Fig. B.2.

$$y_{11open} = G1 + G3 \quad (\text{EQ B.12})$$

$$y_{12open} = -G3 \quad (\text{EQ B.13})$$

$$y_{21open} = -G3 \quad (\text{EQ B.14})$$

$$y_{22open} = G2 + G3 \quad (\text{EQ B.15})$$

Therefore

$$Y_{open} = \begin{bmatrix} G1 + G3 & -G3 \\ -G3 & G2 + G3 \end{bmatrix} \quad (\text{EQ B.16})$$

Y_{short} :

Y_{short} is found using (EQ B.3) to (EQ B.6) and the shorted pad circuit shown in

Fig. B.2.

$$Y_{11short} = G1 + G3 + \frac{1}{Z1} \quad (\text{EQ B.17})$$

$$Y_{12short} = -G3 \quad (\text{EQ B.18})$$

$$Y_{21short} = -G3 \quad (\text{EQ B.19})$$

$$Y_{22short} = G2 + G3 + \frac{1}{Z2} \quad (\text{EQ B.20})$$

The Y parameter matrix is then

$$Y_{short} = \begin{bmatrix} G1 + G3 + \frac{1}{Z1} & -G3 \\ -G3 & G2 + G3 + \frac{1}{Z2} \end{bmatrix} \quad (\text{EQ B.21})$$

$(Y_{short} - Y_{open})$:

$(Y_{short} - Y_{open})$ appears in (EQ B.1) and is evaluated here.

$$\begin{bmatrix} G1 + G3 + \frac{1}{Z1} & -G3 \\ -G3 & G2 + G3 + \frac{1}{Z2} \end{bmatrix} - \begin{bmatrix} G1 + G3 & -G3 \\ -G3 & G2 + G3 \end{bmatrix} = \begin{bmatrix} \frac{1}{Z1} & 0 \\ 0 & \frac{1}{Z2} \end{bmatrix} \quad (\text{EQ B.22})$$

$$(Y_{short} - Y_{open}) = \begin{bmatrix} \frac{1}{Z1} & 0 \\ 0 & \frac{1}{Z2} \end{bmatrix} \quad (\text{EQ B.23})$$

$(Y_{total} - Y_{open})$:

$(Y_{total} - Y_{open})$ also appears in (EQ B.1)

$$Y_{total} - Y_{open} = \begin{bmatrix} G1 + G3 + Y_{11s} & -G3 + Y_{12s} \\ -G3 + Y_{21s} & G2 + G3 + Y_{22s} \end{bmatrix} - \begin{bmatrix} G1 + G3 & -G3 \\ -G3 & G2 + G3 \end{bmatrix} = \begin{bmatrix} Y_{11s} & Y_{12s} \\ Y_{21s} & Y_{22s} \end{bmatrix} \quad (\text{EQ B.24})$$

Inverses of $(Y_{short} - Y_{open})$ and $(Y_{total} - Y_{open})$ are used in (EQ B.1) and are evaluated next.

$(Y_{short} - Y_{open})^{-1}$:

$$(Y_{short} - Y_{open})^{-1} = \begin{bmatrix} \frac{1}{Z1} & 0 \\ 0 & \frac{1}{Z2} \end{bmatrix}^{-1} = \begin{bmatrix} Z1 & 0 \\ 0 & Z2 \end{bmatrix} \quad (\text{EQ B.25})$$

$(Y_{total} - Y_{open})^{-1}$:

To simplify the calculation of $(Y_{total} - Y_{open})^{-1}$, it is helpful to recall that the inverse of a Y parameter matrix for a given network is simply the network's Z parameter matrix.

$$(Y_{total} - Y_{open})^{-1} = Y_s^{-1} = Z_s \quad (\text{EQ B.26})$$

So, rather than trying to find Y_{11s} , Y_{12s} , Y_{21s} , and Y_{22s} in terms of $Z1$, $Z2$ and the inductor Y-parameters (recall from Fig. B.3 that Y_s is the Y parameter matrix of the inductor

with $Z1$ and $Z2$), Z_x is found from the Z parameter equivalent circuit [7] shown in

Fig. B.4.

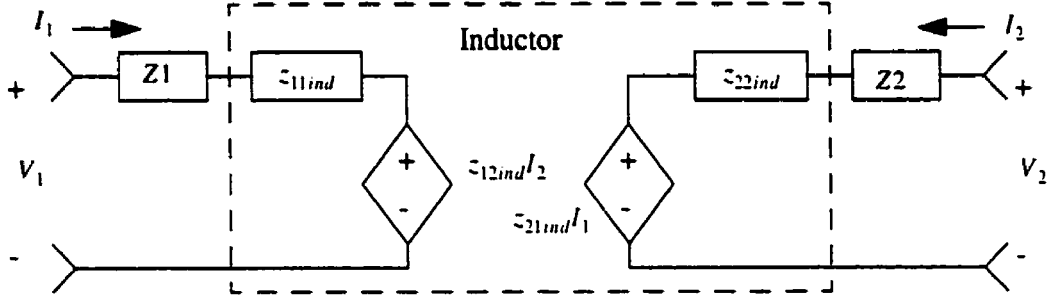


Fig. B.4: Inductor Z parameter equivalent circuit (inside the dashed lines) with feed line series parasitics.

$$z_{11v} = \left. \frac{V_1}{I_1} \right|_{I_2=0} = Z1 + z_{11ind} \quad (\text{EQ B.27})$$

$$z_{12v} = \left. \frac{V_1}{I_2} \right|_{I_1=0} = z_{12ind} \quad (\text{EQ B.28})$$

$$z_{21v} = \left. \frac{V_2}{I_1} \right|_{I_2=0} = z_{21ind} \quad (\text{EQ B.29})$$

$$z_{22v} = \left. \frac{V_2}{I_2} \right|_{I_1=0} = Z2 + z_{22ind} \quad (\text{EQ B.30})$$

$$(Y_{total} - Y_{open})^{-1} = \begin{bmatrix} Z1 + z_{11ind} & z_{12ind} \\ z_{21ind} & Z2 + z_{22ind} \end{bmatrix} \quad (\text{EQ B.31})$$

$$(Y_{total} - Y_{open})^{-1} - (Y_{short} - Y_{open})^{-1} :$$

$$(Y_{total} - Y_{open})^{-1} - (Y_{short} - Y_{open})^{-1} = \begin{bmatrix} Z1 + z_{11ind} & z_{12ind} \\ z_{21ind} & Z2 + z_{22ind} \end{bmatrix} - \begin{bmatrix} Z1 & 0 \\ 0 & Z2 \end{bmatrix} \quad (\text{EQ B.32})$$

$$(Y_{total} - Y_{open})^{-1} - (Y_{short} - Y_{open})^{-1} = \begin{bmatrix} z_{11ind} & z_{12ind} \\ z_{21ind} & z_{22ind} \end{bmatrix} \quad (\text{EQ B.33})$$

$$[(Y_{total} - Y_{open})^{-1} - (Y_{short} - Y_{open})^{-1}]^{-1} :$$

$$[(Y_{total} - Y_{open})^{-1} - (Y_{short} - Y_{open})^{-1}]^{-1} = \begin{bmatrix} \tilde{z}_{11ind} & \tilde{z}_{12ind} \\ \tilde{z}_{21ind} & \tilde{z}_{22ind} \end{bmatrix}^{-1} = \begin{bmatrix} y_{11ind} & y_{12ind} \\ y_{21ind} & y_{22ind} \end{bmatrix} \quad (\text{EQ B.34})$$

where $Y_{ind} = \begin{bmatrix} y_{11ind} & y_{12ind} \\ y_{21ind} & y_{22ind} \end{bmatrix}$ and (EQ B.1) is proven.

APPENDIX C: MATLAB De-embedding Code

C.1 The Modified Cho De-embedding Code

```

%%%%%%c%%o%%a%%n%%a%%l%%y%%s%%.%%m%%   cho_analysis.m  %%%o%%c%%o%%c%%o%%c%%o%%c%%o%%c%%o%%c%%o%%
%%
%%This routine performs the de-embedding of inductors based on Cho's
%%paper.
%%
%%This routine expects to see three variables in memory:
%%
%%ind_to_analyze - a vector of inductor numbers you wish
%%                to examine
%%
%%ind_size - a two character string that states the size
%%          of the inductors to be examined.  ie. for
%%          0.5nH inductor set ind_size = '05'
%%
%%ind_shape - a two character string that states the
%%           shape of the inductors to be examined.
%%           ie. for a square inductor ind_shape = 'sq'
%%
%%This routine provides Q and L values for each spiral.
%%L and Q values are calculated for three types of connections
%%
%%forward - assumes the underpass end of the inductor is grounded.
%%
%%reverse - assumes the non-underpass end of the inductor is grounded.
%%
%%differential - assumes neither end is grounded.  WARNING: THIS
%%FEATURE HAS NOT BEEN VERIFIED FOR ERRORS
%%

%%this variable is used in the following loop to state
%%whether to initialize variable or not
first_time = 1;

%%this loop runs once for each inductor in ind_to_analyze
for gh = 1:length(ind_to_analyze)

```

```

current_ind = num2str(ind_to_analyze(gh))

big_file %this subroutine reads in all the
         %measurement data for the current ind.

S2Y     %converts the S-parameter data to
         %Y-parameter data

chocalc %performs de-embedding routine based
         %Cho's paper.

if first_time == 1 %initializes variables
    L_basic_f_total = zeros(length(L_basic_f),1);
    L_basic_r_total = zeros(length(L_basic_r),1);
    L_basic_d_total = zeros(length(L_basic_d),1);
    L_3metal_f_total = zeros(length(L_3metal_f),1);
    L_3metal_r_total = zeros(length(L_3metal_r),1);
    L_3metal_d_total = zeros(length(L_3metal_d),1);
    L_trench_f_total = zeros(length(L_trench_f),1);
    L_trench_r_total = zeros(length(L_trench_r),1);
    L_trench_d_total = zeros(length(L_trench_d),1);

    Q_basic_f_total = zeros(length(L_basic_f),1);
    Q_basic_r_total = zeros(length(L_basic_r),1);
    Q_basic_d_total = zeros(length(L_basic_d),1);
    Q_3metal_f_total = zeros(length(L_3metal_f),1);
    Q_3metal_r_total = zeros(length(L_3metal_r),1);
    Q_3metal_d_total = zeros(length(L_3metal_d),1);
    Q_trench_f_total = zeros(length(L_trench_f),1);
    Q_trench_r_total = zeros(length(L_trench_r),1);
    Q_trench_d_total = zeros(length(L_trench_d),1);
    first_time = 0;
end
totals %creates unique L and Q vectors for each
       %inductor in ind_to_analyze, also
       %adds data from current inductor to data of
       %past inductors for average calculation.
end

%average Ls and Qs are calculated here
number_of_ind = length(ind_to_analyze);
L_basic_f_avg = L_basic_f_total./number_of_ind;
L_basic_r_avg = L_basic_r_total./number_of_ind;

```

```

L_basic_d_avg = L_basic_d_total./number_of_ind;
L_3metal_f_avg = L_3metal_f_total./number_of_ind;
L_3metal_r_avg = L_3metal_r_total./number_of_ind;
L_3metal_d_avg = L_3metal_d_total./number_of_ind;
L_trench_f_avg = L_trench_f_total./number_of_ind;
L_trench_r_avg = L_trench_r_total./number_of_ind;
L_trench_d_avg = L_trench_d_total./number_of_ind;

```

```

Q_basic_f_avg = Q_basic_f_total./number_of_ind;
Q_basic_r_avg = Q_basic_r_total./number_of_ind;
Q_basic_d_avg = Q_basic_d_total./number_of_ind;
Q_3metal_f_avg = Q_3metal_f_total./number_of_ind;
Q_3metal_r_avg = Q_3metal_r_total./number_of_ind;
Q_3metal_d_avg = Q_3metal_d_total./number_of_ind;
Q_trench_f_avg = Q_trench_f_total./number_of_ind;
Q_trench_r_avg = Q_trench_r_total./number_of_ind;
Q_trench_d_avg = Q_trench_d_total./number_of_ind;

```

```

% big_file.m
%
```

```

% This m-file opens all the S-parameter data files for the inductor given in
% the variable 'current_ind' - note the files must be in Libra format

```

```

pre_fix = strcat(ind_shape, ind_size);

```

```

% load open pads file:

```

```

part_name = strcat(pre_fix, 'ope');

```

```

p_file = strcat(part_name, current_ind);

```

```

open_file = fopen(p_file, 'r');

```

```

raw_data = fscanf(open_file, '%c');

```

```

fclose(open_file);

```

```

start_of_keystring = findstr(raw_data, 'IMG');

```

```

start_of_data = start_of_keystring(length(start_of_keystring)) + 5;

```

```

all_data = raw_data(start_of_data:length(raw_data));

```

```

all_numbers = str2num(all_data);

```

```

freqs = all_numbers(:, 1);

```

```

S11_open = all_numbers(:, 2) + all_numbers(:, 3)*j;

```

```

S21_open = all_numbers(:, 4) + all_numbers(:, 5)*j;

```

```

S12_open = all_numbers(:, 6) + all_numbers(:, 7)*j;

```

```

S22_open = all_numbers(:, 8) + all_numbers(:, 9)*j;

```

```

%load shorted pads data
part_name = strcat(pre_fix, 'sho');
p_file = strcat(part_name,current_ind);
open_file = fopen(p_file,'r');
raw_data = fscanf(open_file, '%c');
fclose(open_file);
start_of_keystring = findstr(raw_data,'IMG');
start_of_data = start_of_keystring(length(start_of_keystring)) + 5;
all_data = raw_data(start_of_data:length(raw_data));
all_numbers = str2num(all_data);
freqs = all_numbers(:,1);
S11_short = all_numbers(:,2) + all_numbers(:,3)*j;
S21_short = all_numbers(:,4) + all_numbers(:,5)*j;
S12_short = all_numbers(:,6) + all_numbers(:,7)*j;
S22_short = all_numbers(:,8) + all_numbers(:,9)*j;

%load interwinding trench inductor data
part_name = strcat(pre_fix, 'tre');
p_file = strcat(part_name,current_ind);
open_file = fopen(p_file,'r');
raw_data = fscanf(open_file, '%c');
fclose(open_file);
start_of_keystring = findstr(raw_data,'IMG');
start_of_data = start_of_keystring(length(start_of_keystring)) + 5;
all_data = raw_data(start_of_data:length(raw_data));
all_numbers = str2num(all_data);
freqs = all_numbers(:,1);
S11_trench = all_numbers(:,2) + all_numbers(:,3)*j;
S21_trench = all_numbers(:,4) + all_numbers(:,5)*j;
S12_trench = all_numbers(:,6) + all_numbers(:,7)*j;
S22_trench = all_numbers(:,8) + all_numbers(:,9)*j;

%load 3met inductor data
part_name = strcat(pre_fix, '3me');
p_file = strcat(part_name,current_ind);
open_file = fopen(p_file,'r');
raw_data = fscanf(open_file, '%c');
fclose(open_file);
start_of_keystring = findstr(raw_data,'IMG');
start_of_data = start_of_keystring(length(start_of_keystring)) + 5;
all_data = raw_data(start_of_data:length(raw_data));
all_numbers = str2num(all_data);
freqs = all_numbers(:,1);

```



```

((1+S11_open(index_)).*(1+S22_open(index_))-
(S12_open(index_).*S21_open(index_)));
Y_open = [(Y11_open.)/50 (Y21_open.)/50 (Y12_open.)/50 (Y22_open.)/50];

```

```
%Shorted pads
```

```

Y11_short(index_) = ((1+S22_short(index_)).*(1-
S11_short(index_))+S12_short(index_).*S21_short(index_))./
((1+S11_short(index_)).*(1+S22_short(index_))-
(S12_short(index_).*S21_short(index_)));
Y12_short(index_) = (-2*S12_short(index_))./
((1+S11_short(index_)).*(1+S22_short(index_))-
(S12_short(index_).*S21_short(index_)));
Y21_short(index_) = (-2*S21_short(index_))./
((1+S11_short(index_)).*(1+S22_short(index_))-
(S12_short(index_).*S21_short(index_)));
Y22_short(index_) = ((1+S11_short(index_)).*(1-
S22_short(index_))+S12_short(index_).*S21_short(index_))./
((1+S11_short(index_)).*(1+S22_short(index_))-
(S12_short(index_).*S21_short(index_)));
Y_short = [(Y11_short.)/50 (Y21_short.)/50 (Y12_short.)/50 (Y22_short.)/50];

```

```
%Inductor with trench
```

```

Y11_trench(index_) = ((1+S22_trench(index_)).*(1-
S11_trench(index_))+S12_trench(index_).*S21_trench(index_))./
((1+S11_trench(index_)).*(1+S22_trench(index_))-
(S12_trench(index_).*S21_trench(index_)));
Y12_trench(index_) = (-2*S12_trench(index_))./
((1+S11_trench(index_)).*(1+S22_trench(index_))-
(S12_trench(index_).*S21_trench(index_)));
Y21_trench(index_) = (-2*S21_trench(index_))./
((1+S11_trench(index_)).*(1+S22_trench(index_))-
(S12_trench(index_).*S21_trench(index_)));
Y22_trench(index_) = ((1+S11_trench(index_)).*(1-
S22_trench(index_))+S12_trench(index_).*S21_trench(index_))./
((1+S11_trench(index_)).*(1+S22_trench(index_))-
(S12_trench(index_).*S21_trench(index_)));
Y_trench = [(Y11_trench.)/50 (Y21_trench.)/50 (Y12_trench.)/50 (Y22_trench.)/
50];

```

```
%Inductor with 3 metal layers
```

```

Y11_3metal(index_) = ((1+S22_3metal(index_)).*(1-
S11_3metal(index_))+S12_3metal(index_).*S21_3metal(index_))./

```



```
G1 = Y_open(x,1) - G3;
G2 = Y_open(x,4) - G3;
```

```
Z1 = 1/(Y_short(x,1)-G1);%G1 added by me
Z2 = 1/(Y_short(x,4)-G2);%G2 added by me
```

```
Y_basic_sf = [Y_basic(x,1) Y_basic(x,3); Y_basic(x,2) Y_basic(x,4)];
Y_trench_sf = [Y_trench(x,1) Y_trench(x,3); Y_trench(x,2) Y_trench(x,4)];
Y_3metal_sf = [Y_3metal(x,1) Y_3metal(x,3); Y_3metal(x,2) Y_3metal(x,4)];
```

```
%subtracting G1 and G2
```

```
Y_basic_sf(1,1) = Y_basic(x,1) - G1;
Y_basic_sf(2,2) = Y_basic(x,4) - G2;
Y_trench_sf(1,1) = Y_trench(x,1) - G1;
Y_trench_sf(2,2) = Y_trench(x,4) - G2;
Y_3metal_sf(1,1) = Y_3metal(x,1) - G1;
Y_3metal_sf(2,2) = Y_3metal(x,4) - G2;
```

```
Z_basic_sf = inv(Y_basic_sf);
Z_trench_sf = inv(Y_trench_sf);
Z_3metal_sf = inv(Y_3metal_sf);
```

```
%subtracting Z1 and Z2
```

```
Z_basic_sf(1,1) = Z_basic_sf(1,1) - Z1;
Z_basic_sf(2,2) = Z_basic_sf(2,2) - Z2;
Z_trench_sf(1,1) = Z_trench_sf(1,1) - Z1;
Z_trench_sf(2,2) = Z_trench_sf(2,2) - Z2;
Z_3metal_sf(1,1) = Z_3metal_sf(1,1) - Z1;
Z_3metal_sf(2,2) = Z_3metal_sf(2,2) - Z2;
```

```
Y_basic_sf = inv(Z_basic_sf);
Y_trench_sf = inv(Z_trench_sf);
Y_3metal_sf = inv(Z_3metal_sf);
```

```
%Removing pad coupling
```

```
Y_basic_sf(1,1) = Y_basic_sf(1,1) - G3;
Y_basic_sf(2,2) = Y_basic_sf(2,2) - G3;
Y_basic_sf(1,2) = Y_basic_sf(1,2) + G3;
Y_basic_sf(2,1) = Y_basic_sf(2,1) + G3;
Y_trench_sf(1,1) = Y_trench_sf(1,1) - G3;
Y_trench_sf(2,2) = Y_trench_sf(2,2) - G3;
Y_trench_sf(1,2) = Y_trench_sf(1,2) + G3;
Y_trench_sf(2,1) = Y_trench_sf(2,1) + G3;
```

```

Y_3metal_sf(1,1) = Y_3metal_sf(1,1) - G3;
Y_3metal_sf(2,2) = Y_3metal_sf(2,2) - G3;
Y_3metal_sf(1,2) = Y_3metal_sf(1,2) + G3;
Y_3metal_sf(2,1) = Y_3metal_sf(2,1) + G3;

Y_basic_de(x,one_four) = [Y_basic_sf(1,one_two), Y_basic_sf(2,one_two)];
Y_trench_de(x,one_four) = [Y_trench_sf(1,one_two), Y_trench_sf(2,one_two)];
Y_3metal_de(x,one_four) = [Y_3metal_sf(1,one_two), Y_3metal_sf(2,one_two)];
end

Z_open_d = -(Y_open(:,1) + Y_open(:,2) + Y_open(:,3) + Y_open(:,4))./
((Y_open(:,3).*(Y_open(:,1)+Y_open(:,3))) -
(Y_open(:,1).*(Y_open(:,4)+Y_open(:,2)))));
Z_basic_d = -(Y_basic_de(:,1) + Y_basic_de(:,2) + Y_basic_de(:,3) + Y_basic_de(:,4))./
((Y_basic_de(:,2).*(Y_basic_de(:,1)+Y_basic_de(:,3))) -
(Y_basic_de(:,1).*(Y_basic_de(:,4)+Y_basic_de(:,2)))));
Z_3metal_d = -(Y_3metal_de(:,1) + Y_3metal_de(:,2) + Y_3metal_de(:,3) +
Y_3metal_de(:,4))./(Y_3metal_de(:,2).*(Y_3metal_de(:,1)+Y_3metal_de(:,3))) -
(Y_3metal_de(:,1).*(Y_3metal_de(:,4)+Y_3metal_de(:,2)))));
Z_trench_d = -(Y_trench_de(:,1) + Y_trench_de(:,2) + Y_trench_de(:,3) +
Y_trench_de(:,4))./(Y_trench_de(:,2).*(Y_trench_de(:,1)+Y_trench_de(:,3))) -
(Y_trench_de(:,1).*(Y_trench_de(:,4)+Y_trench_de(:,2)))));

L_basic_f = imag(1./Y_basic_de(:,1))./(freqs.*2*pi);
L_basic_r = imag(1./Y_basic_de(:,4))./(freqs.*2*pi);
L_basic_d = imag(Z_basic_d)./(freqs.*2*pi);
Q_basic_f = ((2*pi.*freqs).*(L_basic_f))./(real(1./Y_basic_de(:,1)));
Q_basic_r = ((2*pi.*freqs).*(L_basic_r))./(real(1./Y_basic_de(:,4)));
Q_basic_d = ((2*pi.*freqs).*(L_basic_d))./(real(Z_basic_d));

L_3metal_f = imag(1./Y_3metal_de(:,1))./(freqs.*2*pi);
L_3metal_r = imag(1./Y_3metal_de(:,4))./(freqs.*2*pi);
L_3metal_d = imag(Z_3metal_d)./(freqs.*2*pi);
Q_3metal_f = ((2*pi.*freqs).*(L_3metal_f))./(real(1./Y_3metal_de(:,1)));
Q_3metal_r = ((2*pi.*freqs).*(L_3metal_r))./(real(1./Y_3metal_de(:,4)));
Q_3metal_d = ((2*pi.*freqs).*(L_3metal_d))./(real(Z_3metal_d));

L_trench_f = imag(1./Y_trench_de(:,1))./(freqs.*2*pi);
L_trench_r = imag(1./Y_trench_de(:,4))./(freqs.*2*pi);
L_trench_d = imag(Z_trench_d)./(freqs.*2*pi);
Q_trench_f = ((2*pi.*freqs).*(L_trench_f))./(real(1./Y_trench_de(:,1)));
Q_trench_r = ((2*pi.*freqs).*(L_trench_r))./(real(1./Y_trench_de(:,4)));
Q_trench_d = ((2*pi.*freqs).*(L_trench_d))./(real(Z_trench_d));

```

```

%%%%%%%%%%%%%%%%%%%%%% totals.m %%%%%%%%%%%%%%%%%%%%%%
%
%This routine places all the data in appropriate vectors and creates
%a sum of all the data to be used to create an average.
%Variable names are created for each vector of data. For example
%L_trench_f_5 contains the inductance values for inductor #5's
%trench version measured in a forward direction.
%
%The first character in the variable name states whether it is
%L or Q data. The word that follows it describes the fabrication
%method: basic, 3metal, or trench. The last character states
%how the data was calculated: f - forward (underpass end of
%inductor grounded, r - reverse (beginning of spiral grounded),
%or d - differential neither end grounded. WARNING THE
%DIFFERENTIAL CALCULATION HAS NOT BEEN VERIFIED.

Command=strcat('L_basic_f', int2str(gh)):
eval(['L_basic_f' num2str(ind_to_analyze(gh)) '=L_basic_f:']):
eval(['L_basic_r' num2str(ind_to_analyze(gh)) '=L_basic_r:']):
eval(['L_basic_d' num2str(ind_to_analyze(gh)) '=L_basic_d:']):
eval(['L_3metal_f' num2str(ind_to_analyze(gh)) '=L_3metal_f:']):
eval(['L_3metal_r' num2str(ind_to_analyze(gh)) '=L_3metal_r:']):
eval(['L_3metal_d' num2str(ind_to_analyze(gh)) '=L_3metal_d:']):
eval(['L_trench_f' num2str(ind_to_analyze(gh)) '=L_trench_f:']):
eval(['L_trench_r' num2str(ind_to_analyze(gh)) '=L_trench_r:']):
eval(['L_trench_d' num2str(ind_to_analyze(gh)) '=L_trench_d:']):

eval(['Q_basic_f' num2str(ind_to_analyze(gh)) '=Q_basic_f:']):
eval(['Q_basic_r' num2str(ind_to_analyze(gh)) '=Q_basic_r:']):
eval(['Q_basic_d' num2str(ind_to_analyze(gh)) '=Q_basic_d:']):
eval(['Q_3metal_f' num2str(ind_to_analyze(gh)) '=Q_3metal_f:']):
eval(['Q_3metal_r' num2str(ind_to_analyze(gh)) '=Q_3metal_r:']):
eval(['Q_3metal_d' num2str(ind_to_analyze(gh)) '=Q_3metal_d:']):
eval(['Q_trench_f' num2str(ind_to_analyze(gh)) '=Q_trench_f:']):
eval(['Q_trench_r' num2str(ind_to_analyze(gh)) '=Q_trench_r:']):
eval(['Q_trench_d' num2str(ind_to_analyze(gh)) '=Q_trench_d:']):

eval(['Y_short_' num2str(ind_to_analyze(gh)) '(1,:)=Y_short(1,:):']):

L_basic_f_total = L_basic_f_total + L_basic_f;

```

```

L_basic_r_total = L_basic_r_total + L_basic_r;
L_basic_d_total = L_basic_d_total + L_basic_d;
L_3metal_f_total = L_3metal_f_total + L_3metal_f;
L_3metal_r_total = L_3metal_r_total + L_3metal_r;
L_3metal_d_total = L_3metal_d_total + L_3metal_d;
L_trench_f_total = L_trench_f_total + L_trench_f;
L_trench_r_total = L_trench_r_total + L_trench_r;
L_trench_d_total = L_trench_d_total + L_trench_d;

```

```

Q_basic_f_total = Q_basic_f_total + Q_basic_f;
Q_basic_r_total = Q_basic_r_total + Q_basic_r;
Q_basic_d_total = Q_basic_d_total + Q_basic_d;
Q_3metal_f_total = Q_3metal_f_total + Q_3metal_f;
Q_3metal_r_total = Q_3metal_r_total + Q_3metal_r;
Q_3metal_d_total = Q_3metal_d_total + Q_3metal_d;
Q_trench_f_total = Q_trench_f_total + Q_trench_f;
Q_trench_r_total = Q_trench_r_total + Q_trench_r;
Q_trench_d_total = Q_trench_d_total + Q_trench_d;

```

C.2 Modified Koolen De-embedding Code

Note this code calls many of the subroutines in the modified Cho de-embedding code.

```

% ind_analysis.m
%
% This routine performs the de-embedding of inductors based
% on Koolen's paper.
%
% This routine expects to see three variables in memory:
%
% ind_to_analyze - a vector of inductor numbers you wish
%                 to examine
%
% ind_size - a two character string that states the size
%            of the inductors to be examined. ie. for
%            0.5nH inductor set ind_size = '05'
%
% ind_shape - a two character string that states the
%             shape of the inductors to be examined.

```

```

%      ie. for a square inductor ind_shape ='sq'
%
%This routine provides Q and L values for each spiral.
%L and Q values are calculated for three types of connections
%
%forward - assumes the underpass end of the inductor is grounded.
%
%reverse - assumes the non-underpass end of the inductor is grounded.
%
%differential - assumes neither end is grounded. WARNING: THIS
%FEATURE HAS NOT BEEN VERIFIED FOR ERRORS
%

%this variable is used in the following loop to state
%whether to initialize variable or not
first_time = 1;

%this loop runs once for each inductor in ind_to_analyze
for gh = 1:length(ind_to_analyze)
    current_ind = num2str(ind_to_analyze(gh))

    big_file %this subroutine reads in all the
             %measurement data for the current ind.

    S2Y      %converts the S-parameter data to
             %Y-parameter data

    calculate_ind %performs de-embedding routine
                 %based on Koolen's paper.

    if first_time == 1 %initializes variables
        L_basic_f_total = zeros(length(L_basic_f),1);
        L_basic_r_total = zeros(length(L_basic_r),1);
        L_basic_d_total = zeros(length(L_basic_d),1);
        L_3metal_f_total = zeros(length(L_3metal_f),1);
        L_3metal_r_total = zeros(length(L_3metal_r),1);
        L_3metal_d_total = zeros(length(L_3metal_d),1);
        L_trench_f_total = zeros(length(L_trench_f),1);
        L_trench_r_total = zeros(length(L_trench_r),1);
        L_trench_d_total = zeros(length(L_trench_d),1);

        Q_basic_f_total = zeros(length(L_basic_f),1);

```

```

Q_basic_r_total = zeros(length(L_basic_r),1);
Q_basic_d_total = zeros(length(L_basic_d),1);
Q_3metal_f_total = zeros(length(L_3metal_f),1);
Q_3metal_r_total = zeros(length(L_3metal_r),1);
Q_3metal_d_total = zeros(length(L_3metal_d),1);
Q_trench_f_total = zeros(length(L_trench_f),1);
Q_trench_r_total = zeros(length(L_trench_r),1);
Q_trench_d_total = zeros(length(L_trench_d),1);
first_time = 0;
end

totals %creates unique L and Q vectors for each
      %inductor in ind_to_analyze. also
      %adds data from current inductor to data of
      %past inductors for average calculation.
end

number_of_ind = length(ind_to_analyze);
L_basic_f_avg = L_basic_f_total./number_of_ind;
L_basic_r_avg = L_basic_r_total./number_of_ind;
L_basic_d_avg = L_basic_d_total./number_of_ind;
L_3metal_f_avg = L_3metal_f_total./number_of_ind;
L_3metal_r_avg = L_3metal_r_total./number_of_ind;
L_3metal_d_avg = L_3metal_d_total./number_of_ind;
L_trench_f_avg = L_trench_f_total./number_of_ind;
L_trench_r_avg = L_trench_r_total./number_of_ind;
L_trench_d_avg = L_trench_d_total./number_of_ind;

Q_basic_f_avg = Q_basic_f_total./number_of_ind;
Q_basic_r_avg = Q_basic_r_total./number_of_ind;
Q_basic_d_avg = Q_basic_d_total./number_of_ind;
Q_3metal_f_avg = Q_3metal_f_total./number_of_ind;
Q_3metal_r_avg = Q_3metal_r_total./number_of_ind;
Q_3metal_d_avg = Q_3metal_d_total./number_of_ind;
Q_trench_f_avg = Q_trench_f_total./number_of_ind;
Q_trench_r_avg = Q_trench_r_total./number_of_ind;
Q_trench_d_avg = Q_trench_d_total./number_of_ind;

% calculate_ind.m
%
%This m-file de-embeds the pads from the measurements of each
%inductor. Y-parameters for the de-embedded inductors are obtained.

```

%The de-embedding procedure is based on Koolen's paper.

```
one_two = [1 2];
one_four = [1:4];
```

%basic inductor Y-parm extraction

```
for x = 1:length(freqs)
```

```
    Y_basic_sf = [Y_basic(x, 1), Y_basic(x,3); Y_basic(x,2), Y_basic(x,4)];
    Y_3metal_sf = [Y_3metal(x,1), Y_3metal(x,3); Y_3metal(x,2), Y_3metal(x,4)];
    Y_trench_sf = [Y_trench(x,1), Y_trench(x,3); Y_trench(x,2), Y_trench(x,4)];
    Y_open_sf = [Y_open(x,1), Y_open(x,3); Y_open(x,2), Y_open(x,4)];
    Y_short_sf = [Y_short(x,1), Y_short(x,3); Y_short(x,2), Y_short(x,4)];
```

```
    Y_smo = inv(Y_short_sf - Y_open_sf);
```

```
    Y_basic_de_sf = inv(inv(Y_basic_sf - Y_open_sf) - Y_smo);
    Y_3metal_de_sf = inv(inv(Y_3metal_sf - Y_open_sf) - Y_smo);
    Y_trench_de_sf = inv(inv(Y_trench_sf - Y_open_sf) - Y_smo);
```

```
    Y_basic_de(x.one_four) = [Y_basic_de_sf(1.one_two), Y_basic_de_sf(2.one_two)];
    Y_trench_de(x.one_four) = [Y_trench_de_sf(1.one_two), Y_trench_de_sf(2.one_two)];
    Y_3metal_de(x.one_four) = [Y_3metal_de_sf(1.one_two),
    Y_3metal_de_sf(2.one_two)];
end
```

```
Z_open_d = -(Y_open(:,1) + Y_open(:,2) + Y_open(:,3) + Y_open(:,4))./
((Y_open(:,3).*(Y_open(:,1)+Y_open(:,3))) -
(Y_open(:,1).*(Y_open(:,4)+Y_open(:,2)))));
Z_basic_d = -(Y_basic_de(:,1) + Y_basic_de(:,2) + Y_basic_de(:,3) + Y_basic_de(:,4))./
((Y_basic_de(:,2).*(Y_basic_de(:,1)+Y_basic_de(:,3))) -
(Y_basic_de(:,1).*(Y_basic_de(:,4)+Y_basic_de(:,2)))));
Z_3metal_d = -(Y_3metal_de(:,1) + Y_3metal_de(:,2) + Y_3metal_de(:,3) +
Y_3metal_de(:,4))./(Y_3metal_de(:,2).*(Y_3metal_de(:,1)+Y_3metal_de(:,3))) -
(Y_3metal_de(:,1).*(Y_3metal_de(:,4)+Y_3metal_de(:,2)))));
Z_trench_d = -(Y_trench_de(:,1) + Y_trench_de(:,2) + Y_trench_de(:,3) +
Y_trench_de(:,4))./(Y_trench_de(:,2).*(Y_trench_de(:,1)+Y_trench_de(:,3))) -
(Y_trench_de(:,1).*(Y_trench_de(:,4)+Y_trench_de(:,2)))));
```

```
L_basic_f = imag(1./Y_basic_de(:,1))./(freqs.*2*pi);
L_basic_r = imag(1./Y_basic_de(:,4))./(freqs.*2*pi);
L_basic_d = imag(Z_basic_d)./(freqs.*2*pi);
Q_basic_f = ((2*pi.*freqs).*(L_basic_f))./(real(1./Y_basic_de(:,1)));
Q_basic_r = ((2*pi.*freqs).*(L_basic_r))./(real(1./Y_basic_de(:,4)));
```

```

Q_basic_d = ((2*pi.*freqs).*(L_basic_d))./(real(Z_basic_d));

L_3metal_f = imag(1./Y_3metal_de(:,1))./(freqs.*2*pi);
L_3metal_r = imag(1./Y_3metal_de(:,4))./(freqs.*2*pi);
L_3metal_d = imag(Z_3metal_d)./(freqs.*2*pi);
Q_3metal_f = ((2*pi.*freqs).*(L_3metal_f))./(real(1./Y_3metal_de(:,1)));
Q_3metal_r = ((2*pi.*freqs).*(L_3metal_r))./(real(1./Y_3metal_de(:,4)));
Q_3metal_d = ((2*pi.*freqs).*(L_3metal_d))./(real(Z_3metal_d));

L_trench_f = imag(1./Y_trench_de(:,1))./(freqs.*2*pi);
L_trench_r = imag(1./Y_trench_de(:,4))./(freqs.*2*pi);
L_trench_d = imag(Z_trench_d)./(freqs.*2*pi);
Q_trench_f = ((2*pi.*freqs).*(L_trench_f))./(real(1./Y_trench_de(:,1)));
Q_trench_r = ((2*pi.*freqs).*(L_trench_r))./(real(1./Y_trench_de(:,4)));
Q_trench_d = ((2*pi.*freqs).*(L_trench_d))./(real(Z_trench_d));

```

C.3 The 1-Port De-embedding Code

```

% port1_analysis.m %
% This m-file performs the de-embedding procedure for the single
% port spiral inductors.
%
% This routine expects to see three variables in memory:
%
% ind_to_analyze - a vector of inductor numbers you wish
%                 to examine
%
% ind_size - a two character string that states the size
%            of the inductors to be examined. ie. for
%            0.5nH inductor set ind_size = '05'
%
% ind_shape - a two character string that states the
%             shape of the inductors to be examined.
%             ie. for a square inductor ind_shape = 'sq'
%
first_time = 1;

% Reading in the port 1 short data
p_file = 'libra_sim_port1_short';
open_file = fopen(p_file,'r');

```

```

raw_data = fscanf(open_file, '%c');
fclose(open_file);
start_of_keystring = findstr(raw_data,'GHz');
start_of_data = start_of_keystring(length(start_of_keystring) + 5);
all_data = raw_data(start_of_data:length(raw_data));
all_numbers = str2num(all_data);
freqs = all_numbers(:,1);
S11_pad_port1_short = all_numbers(:,2) + all_numbers(:,3)*j;

Y11_pad_port1_short = (1-S11_pad_port1_short)/(1+S11_pad_port1_short).*(1/50);

%Loading and processing measured data
for gh = 1:length(ind_to_analyze)
    current_ind = num2str(ind_to_analyze(gh))
    big_file
    S2Y_1p

    Y11_basic_de = 1./((1./(Y11_basic-Y11_open)) - (1./(Y11_pad_port1_short-
Y11_open)));
    Y11_trench_de = 1./((1./(Y11_trench-Y11_open)) - (1./(Y11_pad_port1_short-
Y11_open)));
    Y11_3metal_de = 1./((1./(Y11_3metal-Y11_open)) - (1./(Y11_pad_port1_short-
Y11_open)));

    L_basic_f = imag(1./Y11_basic_de)/(freqs.*2*pi);
    L_trench_f = imag(1./Y11_trench_de)/(freqs.*2*pi);
    L_3metal_f = imag(1./Y11_3metal_de)/(freqs.*2*pi);

    Q_basic_f = imag(1./Y11_basic_de)/(real(1./Y11_basic_de));
    Q_trench_f = imag(1./Y11_trench_de)/(real(1./Y11_trench_de));
    Q_3metal_f = imag(1./Y11_3metal_de)/(real(1./Y11_3metal_de));
    if first_time == 1
        L_basic_f_total = zeros(length(L_basic_f),1);
        L_3metal_f_total = zeros(length(L_3metal_f),1);
        L_trench_f_total = zeros(length(L_trench_f),1);

        Q_basic_f_total = zeros(length(L_basic_f),1);
        Q_3metal_f_total = zeros(length(L_3metal_f),1);
        Q_trench_f_total = zeros(length(L_trench_f),1);
        first_time = 0;
    end
    totals_1p
end
end

```

```

number_of_ind = length(ind_to_analyze);
L_basic_f_avg = L_basic_f_total./number_of_ind;
L_3metal_f_avg = L_3metal_f_total./number_of_ind;
L_trench_f_avg = L_trench_f_total./number_of_ind;

```

```

Q_basic_f_avg = Q_basic_f_total./number_of_ind;
Q_3metal_f_avg = Q_3metal_f_total./number_of_ind;
Q_trench_f_avg = Q_trench_f_total./number_of_ind;

```

```

%%%%%%%%%%%%%%%%%%%%%%%%%%%%%%%%%%%%%%%% S2Y_1p.m %%%%%%%%%%
%
```

```

%
```

```

%This routine converts one port measurement S-parameters
%to Y-parameters.

```

```

Y11_open = (1-S11_open)/(1+S11_open).*(1/50);
Y11_short = (1-S11_short)/(1+S11_short).*(1/50);
Y11_basic = (1-S11_basic)/(1+S11_basic).*(1/50);
Y11_trench = (1-S11_trench)/(1+S11_trench).*(1/50);
Y11_3metal = (1-S11_3metal)/(1+S11_3metal).*(1/50);

```

```

%%%%%%%%%%%%%%%%%%%%%%%%%%%%%%%%%%%%%%%% totals_1p.m %%%%%%%%%%
%
```

```

%This routine is for one port measurements.
%
```

```

%
```

```

%This routine places all the data in appropriate vectors and creates
%a sum of all the data to be used to create an average.

```

```

Command=strcat('L_basic_f'.int2str(gh));
eval(['L_basic_f' num2str(ind_to_analyze(gh)) '=L_basic_f:']):
eval(['L_3metal_f' num2str(ind_to_analyze(gh)) '=L_3metal_f:']):
eval(['L_trench_f' num2str(ind_to_analyze(gh)) '=L_trench_f:']):

```

```

eval(['Q_basic_f' num2str(ind_to_analyze(gh)) '=Q_basic_f:']):
eval(['Q_3metal_f' num2str(ind_to_analyze(gh)) '=Q_3metal_f:']):
eval(['Q_trench_f' num2str(ind_to_analyze(gh)) '=Q_trench_f:']):

```

```

L_basic_f_total = L_basic_f_total + L_basic_f;
L_3metal_f_total = L_3metal_f_total + L_3metal_f;
L_trench_f_total = L_trench_f_total + L_trench_f;

```

```

Q_basic_f_total = Q_basic_f_total + Q_basic_f;

```

$$\begin{aligned} Q_{3\text{metal}_f\text{total}} &= Q_{3\text{metal}_f\text{total}} + Q_{3\text{metal}_f}; \\ Q_{\text{trench}_f\text{total}} &= Q_{\text{trench}_f\text{total}} + Q_{\text{trench}_f}; \end{aligned}$$

APPENDIX D: Full Circuit Schematic

This appendix provides a complete schematic of the bias current tuned oscillator fabricated as part of this work.

The transistors are labeled with a unitless number followed by a length in micrometers. For example the differential pair transistors of Fig. D.1 are labeled:

111
5 μ m

Each digit of the first number (111) represents, in the following order, the number of emitter, base, and collector stripes of the transistor. In the above example the transistor has one emitter stripe, one base stripe, and one collector stripe.

The second number in the transistor label is the emitter length. The transistor in the above example has an emitter length of 5 μ m.

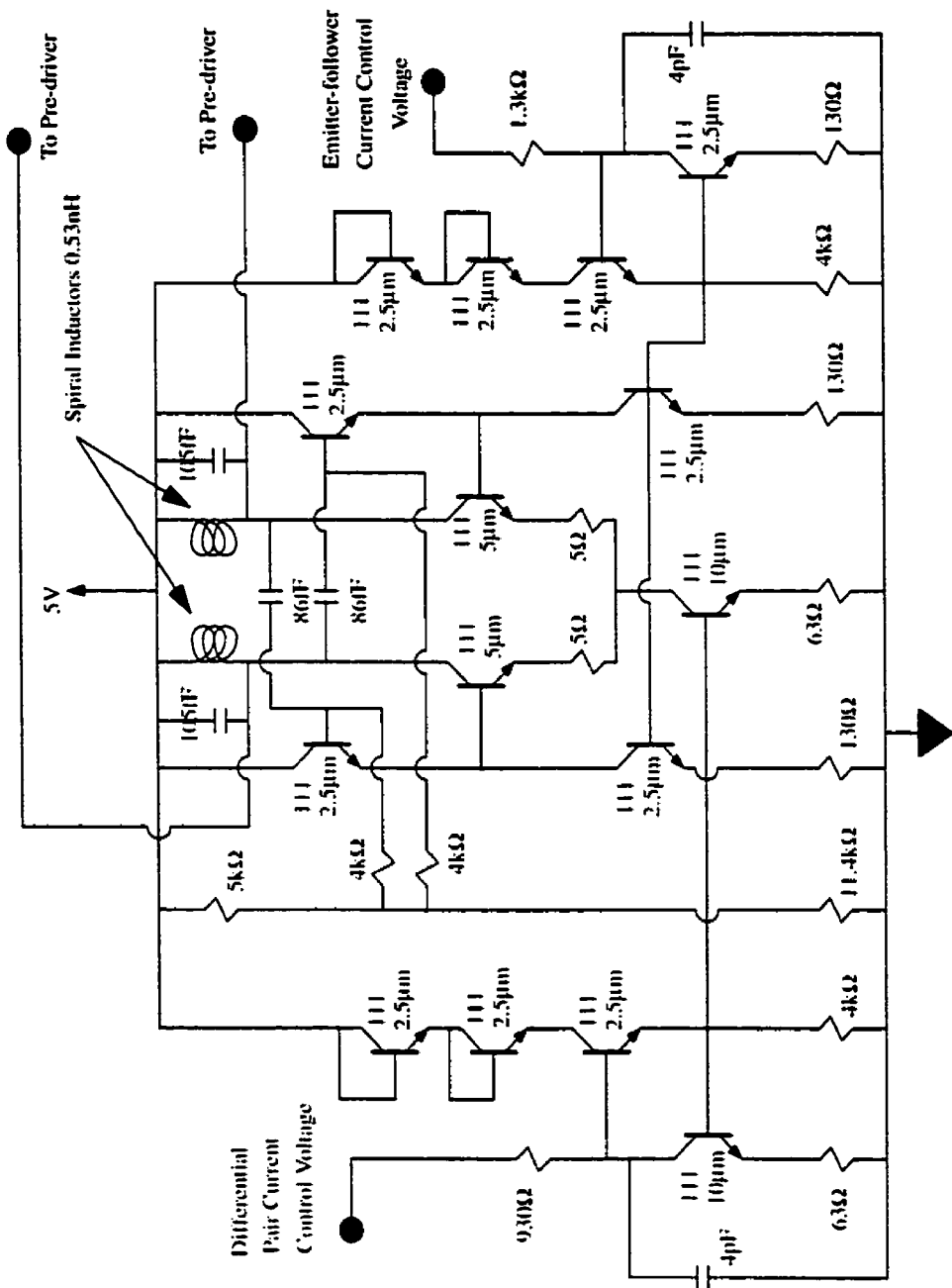


Fig. D.1: Schematic of oscillator circuit.

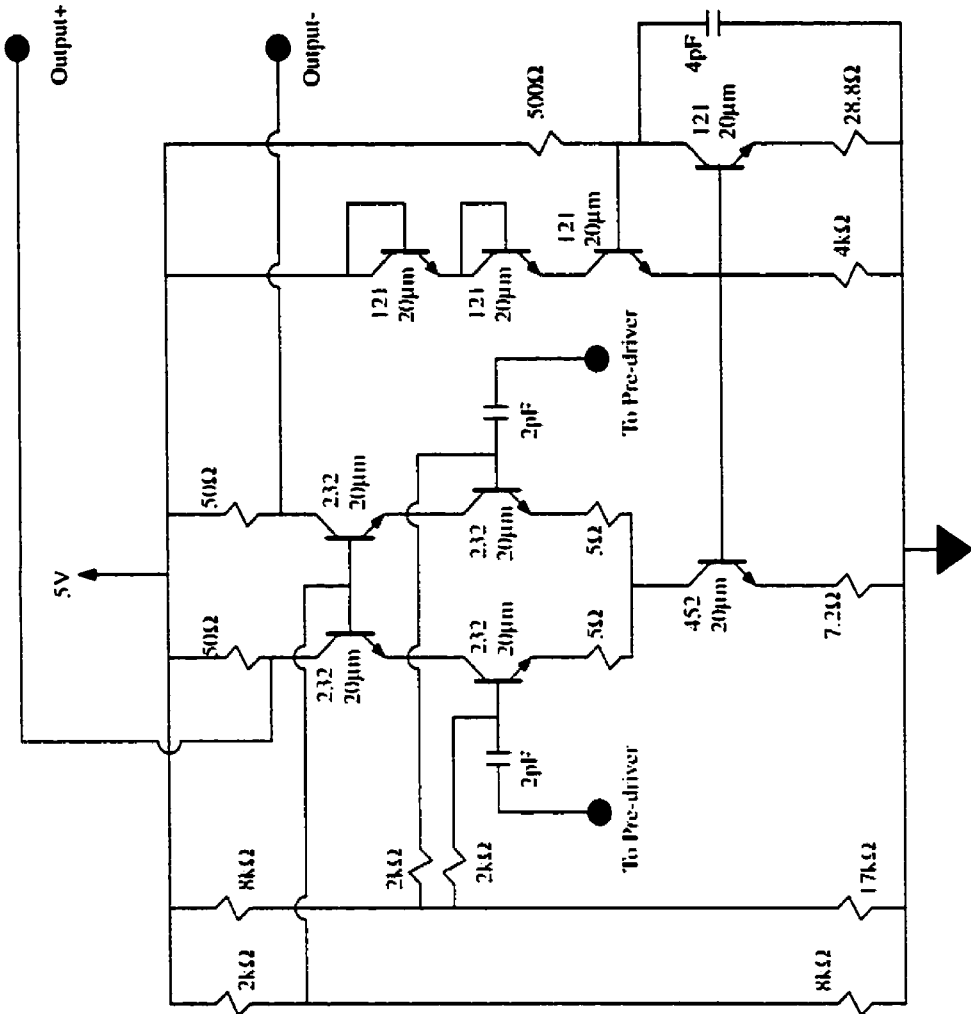


Fig. D.3: Schematic of output buffer circuit.